UNIVERSITA' DEGLI STUDI TOR VERGATA
ROMA

Dipartimento di Informatica, Sistemi e Produzione
GeoInformation Research Doctorate

Microwave Radiometry for Breast Cancer Detection

Candidate: **Santina Iudicello**

Mentor: **prof. Fernando Bardati**

Marzo 2009

Acknowledgements

First of all, I would like to thank my advisor Prof. Fernando Bardati for his thoughtful guidance during this thesis. He provided me with many helpful suggestions, important advice and patience during the course of this work.

I thank Prof. Piero Tognolatti for help with the experimental setup and precious general advice.

I thank Fabrizio Mancini for taking care of the realization of the antennas presented in this thesis.

A sincere thanks goes to Prof. Paolo Coppa and Ing. Gianluigi Bovesecchi for the help in the control temperature system for the phantom setup.

I wish to express my cordial appreciation for the useful collaboration with the research group of Prof. Enrico Verona.

I am also very grateful to the many volunteers I have measured my antennas on. Special gratitude goes to Patrizia Di Iulio for her kindness in having hosted me in her house to carry out my measurements. She trusted me and my research field right now and I was very happy of this.

I would also like to thank my parents, my brothers and my sister for the support they provided me through my studies; they raised me and encouraged all my decisions.

Finally, I thank my husband for instilling in me confidence and drive for pursuing all my interests and in particular my PhD.

Abstract

Interest in breast imaging with electromagnetic fields in the microwave band has been mainly motivated by certain deficiencies in current screening and diagnostic practices based on X-ray mammography.

In this thesis the feasibility of microwave radiometry as a modality for early-stage breast cancer detection has been investigated based on the tumor over-temperature rationale.

The goal of this work is to establish the rationale for the application of microwave radiometry for breast cancer detection and to provide the basis for setting-up measurements on patients.

Basing on electrical and thermal properties of breast tissue available in the literature I developed a numerical model to predict the radiometric output when a contacting antenna is scanned on the breast surface. For this reason, a full 3D model that relates radiometric data to the temperature difference between normal and malignant breast has been developed in order to predict the radiometric visibility of tumors.

Then, I found that the deformation by a cooled antenna pressed against the breast lowers the distance of a subsurface tumor from the contacted surface thus improving the tumor radiometric visibility. I showed this result modeling breast deformation, temperature distribution and corresponding radiometer output both in the presence of a tumor and in its absence.

Two patch antennas have been designed to be matched to a multilayer model of the breast. The antennas have been measured on volunteers in a preliminary small-scale experimental study. By estimating the antenna reflectivity I derived a requirement on the residual temperature when non-ideal radiation balance radiometer and antenna are considered.

Some measurements with the "Tor Vergata" radiometer are presented. The radiometric resolution has been characterized when a matched load immersed in a water bath is connected to the input of the radiometer. A breast phantom and a thermal anomaly imitator for the mammary gland have been developed.

The results of phantom measurements give positive indication on the feasibility of thermal spot detection by our radiometer.

Contents

Introduction

This thesis reports on my research on a passive microwave technique with regard to early-stage breast cancer detection. Results from this study demonstrate the feasibility of tumor detection via differential (malignant-normal) data resulting from the measurement of thermal radiation spontaneously released by the tissue in the microwave frequency band and related to a target volume of the breast.

Chapter 1 introduces the present state of breast imaging technologies for diagnosis that are currently performed or under investigation and discusses how my alternative modality can contribute to the field. I shall distinguish between breast imaging technologies that are currently performed and recognized by health public authorities and those (still under investigation) that are being investigated as they have not yet obtained a general scientific consensus and approval by authorities in the field.

Chapter 2 looks at the general principles of microwave radiometry with particular reference to its application as a diagnostic tool for breast cancer detection. A simple scheme on the modalities for radiometric data collection during a diagnostic session of breast cancer is proposed.

Tumor over-temperature is discussed in this chapter as the rationale for breast cancer detection by microwave radiometry. It has been modeled for different diameters of the tumor at different depths in the breast, according to thermal parameters found in the literature. Some useful indicators of the tumor over-temperature (such as a *thermal apparent volume* and a *thermal equivalent diameter*) have been defined in order to understand to which extent it may affect the signal received by a radiometer depending on tumor size and depth.

Chapter 3 is devoted to the development of a 3D breast electromagnetic model in order to predict the radiometric output when a contacting antenna is scanned on the breast. Both an ideal radiation balance radiometer and an ideal antenna have been considered in this chapter for generality. A parametric study on the radiometric visibility of thermal anomalies is presented for an antenna

consisting of a circular aperture in a perfectly conducting screen.

A breast homogeneous model has been considered both for the radiometric weighting function and the temperature computation inside the breast. At the end of the chapter a *tumor radiometric visibility* has been defined to discuss the detectability of a tumor by a radiometric system. Results on a more realistic non homogeneous model with dielectric parameters based on a recent large-scale experimental characterization, are presented in Chapter 4.

In this chapter I addressed the mechanical problem of breast tissue deformation to evaluate to which extent the tumor radiometric visibility improves when the breast undergoes compression. While breast flattening has been treated as a negligible effect in the modeling by previous authors, in this paper the breast is intentionally squeezed between antenna and thorax. I estimated the thermal behavior and the corresponding radiometric signal for the deformed breast. Large deformations have been taken into account and computational efforts have been done owing to material and geometric non-linearities.

The contact problem has been solved as a constrained minimization problem due to a non-penetration condition at the antenna-breast interface.

Results on the radiometric signal in the presence of a 35% deformation of the breast are presented for comparison with those related to the undeformed condition. Differences in the radiometric signal between the homogeneous and the multilayer model of the breast are also discussed in this chapter.

In Chapter 5 I addressed the problem of estimating the radiometric signal when both the antenna and the radiometer are non-ideal. The residual error in the radiometric temperature estimation due to a non-ideal instrumentation has been defined. This error has been found to depend both on the radiometric antenna and instrumentation.

A requirement on the receiver electronics has been derived from a preliminary small-scale experimental study of two small contacting antennas on volunteers in order to make this error lower than a standard radiometric resolution.

The two patch antennas have been designed to be matched with a multilayer breast tissue at the receiver centre band frequency. These antennas have been measured on volunteers splitted into two groups aged 20-40 and 40-60, respectively. Measured input impedance and return loss are presented. Standard deviation of samples has been computed over the frequency range between 2 and 3GHz showing relatively low dispersion of the data and also good agreement with the numerical computations. Data postprocessing has highlighted differences in the best matching frequency due to position of the antenna on the breast, supposing to divide each breast into 5 quadrants.

The experimental results give also some indications on the antenna to be

optimized for use as a radiometric device.

The sixth and final chapter is devoted to radiometer characterization. Preliminary measurements with an existing 2.65GHz radiometer are included in this chapter to show the sample standard deviation and temperature resolution when a matched load fully immersed in a thermostatated bath, is connected to the input of the radiometer. A breast phantom and a tumor-imitator have been modeled. Encouraging results are shown when a patch antenna is used.

Chapter 1

An overview of the Breast Cancer Screening and Diagnostic Technologies

1.1 Breast Cancer Statistics

Breast cancer is the most common cancer among women worldwide and the second most common type of cancer after lung cancer. Women in the United States have the highest incidence rates of breast cancer in the world. Approximately one in every eight US women is diagnosed with breast cancer by the age of 90, for an absolute lifetime risk of 14.4% [1]. The National Cancer Institute estimates 182.460 new cases and 40.480 deaths in 2008. Breast cancer also occurs in men, but accounts for less than one percent of male malignancies. The incidence of breast cancer varies greatly around the world, being lower in less-developed countries and greatest in the more-developed countries. Age-adjusted annual incidence rates for invasive breast cancer decreased each year from 1999 to 2003, with the greatest decrease in rates occurring from 2002 to 2003. For in situ cancers, rates increased each year from 1999 to 2002 and then decreased from 2002 to 2003, although the percentage decrease (2.7%) was smaller than that for invasive cancers (6.1%). Conversely, a widespread reduction of mortality rates has been observed from the early 1990s (i.e., from 22% in 1990 to 18% in 2000) [1]-[2], which is likely attributable to advancements in medical treatments and to the role of mammography screening in detecting cancers at

an earlier stage. All women are at risk for developing breast cancer. The older a woman is, the greater her chances of developing breast cancer. Approximately 77% of breast cancer cases occur in women over 50 years of age. The risk of developing breast cancer is related to a number of factors including the events of reproductive life and lifestyle factors that modify endogenous levels of sex-hormones [3]. Diet has been also found to play an important role in the etiology of breast cancer [4]. The probability of developing breast cancer within the next 10 years increases with age passing from 0.05% for women by age 20 to 12.5% for women by age 70. While breast cancer is less common at a young age (i.e., in their thirties), younger women tend to have more aggressive breast cancers with faster growth than older women, which may explain why survival rates are lower among younger women. Five year survival rate is 81% for women younger than 45, 85% for women aged 45-64 and 86% for women aged 65 and older. The vast majority of breast tumors originate within the fibroglandular breast tissue. Breast cancer stages range from Stage 0 (very early form of cancer) to Stage IV (advanced, metastatic breast cancer). The five-year survival rate for breast cancer is calculated based on averages. Each patient's individual tumor characteristics, state of health, genetic background, etc. will impact her survival. The five-year relative survival rate passes from 100% for Stage 0 and Stage I breast cancer to 20% for Stage IV breast cancer with an overall survival rate after 5 years of about 88%, after 10 years of about 80%, after 15 years of about 71% and after 20 years of about 63%.

1.2 Current Breast Cancer Screening and Diagnosis

1.2.1 Mammography

The key to surviving breast cancer is early detection that reduces the need for therapeutic treatment and minimizes pain and suffering. According to the American Cancer Society when breast cancer is confined to the breast, the five-year survival rate is close to 100%.

There are several methods of screening. Women 20 years of age and older should be told about the benefits and limitations of breast self-exams (BSE). Women should be aware of how their breasts normally feel and report any new breast change to a health professional as soon as they are found. [Note: while the American Cancer Society recently amended its guidelines and no longer recommends monthly BSE, many healthcare professionals believe strongly in this

easy, no cost method of screening for breast cancer and continue to recommend BSE on a monthly basis].

Women 20-39 should have a physical examination of the breast (CBE or clinical breast exam) at least every three years, performed by health care professional such as a physician. Women 40 and older should have a CBE every year, performed by a physician and they should receive a screening mammogram every year. The National Cancer Institute recommends mammography every one to two years for women between 40-50 years of age. Beginning at age 50, screening mammography should be performed every year.

However, the standard screening technology X-ray mammogram has many unsatisfactory features, as explained in the following section. Yet the efficacy of the standard (and notoriously uncomfortable) early detection-test, the X-ray mammogram, has been disputed of late, especially for younger women. Most experts agree that mammography screening benefits women 50-69 years old [5]-[6]. Meta-analysis of randomized-control trials of mammography screening show a 25-30% reduction in breast cancer mortality for women over 50, and a smaller, more equivocal effect in women aged 40-49 [7].

1.2.2 Mammography and the Rationale for Alternatives

Screening might produce greater benefits if it were more sensitive and specific. Most tumors become visible at screening when they reached a diameter of 5mm to 10mm.

Mammography is currently the most effective method of detecting asymptomatic breast cancer. Its use for screening has been widely promoted by the National Cancer Institute and other organizations. The goal of screening mammography is to detect breast cancer when it is still too small to be felt by a physician or the patient. Mammography can detected approximately 85% of breast cancers. If a screening mammography indicates an abnormality, women will most likely be recommended for further breast imaging (i.e., with spot view mammography, ultrasound or other imaging tests). If further imaging confirms or reveals an abnormality, the woman may be referred for biopsy to determine whether she has breast cancer. While screening mammography can detect most breast cancers, it can miss up to 15% of cancers but it can also detect cancer several years before a lump can be felt. Average-size lump detected with routine mammogram is about 1.1cm. Average-size lump detected with self breast exam is 2.1cm.

Mammography can also be performed as a diagnostic test in order to evaluate a breast complaint or abnormality detected by physical exam or routine

screening mammography.

Diagnostic mammography is different from screening mammography in that additional views of the breast are usually taken, as opposed to two views typically taken with screening mammography. Thus, diagnostic mammography is usually more time-consuming and costly than screening mammography. Typical views for diagnostic mammograms include the cranio-caudal view (CC), the medio-lateral-oblique view (MLO), and supplemental views tailored to the specific problem. The goal of diagnostic mammography is to pinpoint the exact size and location of breast abnormality and to image the surrounding tissue and lymph nodes. In many cases, diagnostic mammography will help show that the abnormality is highly likely to be benign (non-cancerous). Abnormalities that can be detected by mammography are two main ones being calcifications (micro and macrocalcifications) and masses. Calcifications are tiny mineral deposits within the breast tissue that appear as small white regions on the mammogram films. Microcalcifications are tiny (less than 1/50 of an inch or 1/2 of a millimeter) and they may indicate a small cancer and they are the most common mammographic sign of ductal carcinoma in situ (an early cancer confined to the breast ducts). Almost 90% of cases of ductal carcinoma in situ are associated with microcalcifications. In other cases, the microcalcifications are more suspicious and a biopsy is recommended. Only approximately 17% of calcifications requiring biopsy are cancerous. Macrocalcifications are coarse (large) calcium deposits that are often associated with benign fibrocystic change or with degenerative changes in the breasts, such as aging of the breast arteries, old injuries, or inflammation.

Another important change seen on a mammogram is the presence of a mass, which may occur with or without associated calcifications. A mass is any group of cells clustered together more densely than the surrounding tissue. A cyst (a non-cancerous collection of fluid in the breast) may appear as a mass on a mammogram film. A cyst cannot be diagnosed by physical exam alone nor can it be diagnosed by mammography alone, although certain signs can suggest the presence of a cyst or cysts. To confirm that a mass is a cyst, either breast ultrasound or aspiration with a needle is required. As with calcifications, a mass can be caused by benign breast conditions or by breast cancer. The size, shape, and margins (edges) of the mass help the radiologist in evaluating the likelihood of cancer. Enhancements of screen-film mammography have included full-field digital mammography and computer-aided detection of abnormalities. The primary motivation behind the development of digital X-ray mammography is the belief that it has the potential to improve image quality and therefore lesion detection (especially for dense breasts) with a lower dose of radiation

compared to that required for conventional film-based mammography.

Despite its recognized value in detecting and characterizing breast disease, mammography has important limitations. First, its false-negative rate ranges from 4% to 34%, depending on the length of follow-up after a "normal" mammogram [8]. Second, screening mammography is less sensitive in women with radiographically dense breast tissue [4]. This is of particular concern because the amount of fibroglandular tissue may represent an independent risk factor for developing breast cancer [9]. Third, screening mammography also suffers from a high false-positive rate: on average, 75% of breast biopsies prompted by a "suspicious" mammographic abnormality prove benign [2]. Mammography's other drawbacks include discomfort due to breast compression, variability in radiological interpretation, and a slight risk of inducing cancer due to the ionizing radiation exposure.

1.2.3 Ultrasound

Breast ultrasound is frequently used to evaluate breast abnormalities that are found with screening or diagnostic mammography or during a physician performed clinical breast exam and to localize tumors before biopsy. Ultrasound waves are high frequency sound waves that reflect at boundaries between tissues with different acoustic properties. The depth of these boundaries is proportional to the time intervals of reflection arrivals thus mapping an image of tissue boundaries.

Conventional ultrasound is excellent at imaging cysts: round, fluid-filled, pockets inside the breast. Additionally, ultrasound can often quickly determine if a suspicious area is in fact a cyst (always non-cancerous) or an increased density of solid tissue (dense mass) which may require a biopsy to determine if it is malignant (cancerous). Ultrasound has excellent contrast resolution. This means, for example, that an area of fluid (cyst) and an area of normal breast tissue are easy to differentiate on an ultrasound image.

However, ultrasound does not have good spatial resolution like mammography, and therefore cannot provide as much detail as a mammogram image. Conventional ultrasound has been limited in its ability to detect microcalcifications that cannot be distinguish from artifacts. A new technique called "compound imaging" reduces speckle in the breast images thus improving the contrast and definition of small lesion (i.e. microcalcifications).

A breast biopsy is performed to determine whether the suspicious lump is benign or cancerous. Less than 30% of all breast biopsies are cancerous.

1.2.4 Magnetic Resonance

Magnetic resonance breast imaging (MRI or MR) in addition to mammography, help diagnose breast cancer thus eliminating unnecessary biopsies. Magnetic resonance images are created by recording the signals generated after radiofrequency excitation of hydrogen nuclei (or other element) in tissue exposed to a strong static magnetic field. The signals have characteristics that vary according to tissue type.

It is often used to investigate breast concerns first detected with mammography, physical exam, or other imaging exams.

MRI is also excellent at imaging the augmented breast, including both the breast implant itself and the breast tissue surrounding the implant (abnormalities or signs of breast cancer can sometimes be obscured by the implant on a mammogram). MRI is also useful for staging breast cancer, determining the most appropriate treatment. It is recommended for women under 40 with high risk of breast cancer. Because MRI is more sensitive than mammography, it can help detect cancer that may be missed by mammography. However, because this increased sensitivity can also lead to false positive results.

The most useful MRI technique (dynamic contrast imaging) for breast imaging uses a contrast material called Gadolinium DTPA, which is injected into a vein in the arm before or during the exam to improve the quality of the images. This contrast agent helps produce stronger and clearer images and "highlight" any abnormalities. An MRI exam allows breast images to be taken in any plane and from any orientation. Dynamic contrast imaging typically images only a cross section of the breast. Three-dimensional high-resolution imaging generates whole-breast images, which allow radiologists to detect additional breast lesions that may be missed by dynamic contrast imaging.

One particular advantage of MRI is that it is highly sensitive to small abnormalities that can sometimes be missed with other exams. Determining the extent of breast cancer with MRI can help indicate treatment: breast conserving surgery (lumpectomy) or breast removal (mastectomy). The sensitivity of MRI ranges between 88 and 100%. The reported specificity ranges from 28 and 100% depending on the patient population and on the interpretation technique used [1].

MRI may also be useful in helping to determine whether breast cancer has spread into the chest wall. If there is evidence of breast cancer in the chest wall, a patient often needs to undergo chemotherapy before breast cancer surgery. Not knowing whether the chest wall is involved can delay chemotherapy and cause the patient to have both chemotherapy and radiation therapy after surgery.

Physicians sometimes use MRI to detect cancer recurrences in women who have already been treated for breast cancer with lumpectomy.

There are limitations associated with MRI. First, MRI cannot always distinguish between cancerous and non-cancerous abnormalities, which can lead to unnecessary breast biopsies. The disparity between the very high degree of sensitivity and the relatively low degree of specificity of the technology can be problematic in that unexpected lesions - found incidentally in the breast during the MRI workup of a lump detected by mammography - are often observed. This means that MRI has been shown to produce a moderate amount of false-positive results. This raises the question as to whether such lesions should also be monitored or biopsied.

Another drawback of breast MRI is that has historically been unable to effectively image calcifications, tiny calcium deposits that can indicate breast cancer. Still, mammography can reliably image calcifications, which are often associated with early-stage breast cancers such as ductal carcinoma in situ (DCIS).

Furthermore, MRI is an expensive exam; an average MRI of the breast costs approximately $1000 versus $100 per screening mammogram. MRI can also take longer than mammography: more than 30 minutes in addition to the administration of the contrast versus 10 to 15 minutes for a screening mammogram. Patients need to lie still in a prone (face down) position during the exam to eliminate motion in the images. Though an MRI exam is not painful, patients must tolerate any claustrophobia (fear of small spaces) they may have. A contrast agent is also given prior to the exam to improve image quality.

1.2.5 Scintimammography

Breast scintimammography can be helpful in selected cases (e.g. dense breasts, palpable anomalies not revealed by mammography or ultrasound) after a diagnostic mammography and ultrasound have been performed. It involves injecting a radioactive tracer (Miraluma Tc-99m, dye) into the patient. Since the dye accumulates differently in cancerous and non-cancerous tissues, scintimammography can help physicians determine whether cancer is present. The tracer concentrates more in the breast cancer than in normal tissue by a mechanism not well understood but that may be related to the degree of cellular proliferation and vascular permeability. Scintimammography image the spatial concentration of the radiotracers. A special gammacamera is used to capture images of the breast from several angles. Images are planar or three-dimensional if generated by tomographic reconstruction (Single-photon-emission computed tomography [SPECT]).

It also used to help determine if the lymph nodes contain cancer cells. No breast compression is necessary.

Breast scintimammography can be also useful to detect a lump at the surgical site after mastectomy since scar tissue may be difficult to distinguish from other tumors with other breast imaging exams. Studies show that nuclear medicine breast imaging is only 40% to 60% accurate in imaging small breast abnormalities but more than 90% accurate in detecting abnormalities over one centimeter. It is more expensive than ultrasound and mammography, it costs $200 to $600 per exam. The small dose of radioactivity are generally considered safe except for pregnant women and young children. Studies indicate that the overall sensitivity of the technique ranges from 75 to 94 percent and that the specificity ranges from 80 to 89 percent [1].

1.2.6 PET

Breast PET (Positron Emission Tomography) is used to discriminate between benign and malign lesion.

It uses very short-lived radioactive compounds that localize in cancer cells. Cancer cells have alterations in the normal metabolism of the glucose, and have increased glucose uptake and decreased glucose clearance. Glucose can be bound to the positron 18-F to make a compound 18 F-fluorodeoxyglucose, FDG. When injected into a patient's blood stream, FDG is taken up by the cancer cells at a more rapid rate than normal cells and allows cancers to be seen as "hot spots" on the PET scan. A typical PET scan usually images the body from the head to the upper thighs. Scanners are now available that can perform both PET and CT scans in the same imaging session. The images that are obtained can be overlaid or fused so the functional information of the PET scan can be accurately localized on the high-resolution anatomic images of the CT scan. Fusion imaging performed on these hybrid scanners has been shown to improve whole body scan diagnostic accuracy. Although accuracy in detecting tumors larger than 2cm is high, PET may miss approximately one third of invasive cancers smaller than 1 centimeter.

Care must be taken in interpreting PET scans of patients after biopsy of surgery, as sites of inflammation of infection will also display increased uptake of FDG. With these limitations, PET is not useful as a screening tool. It may, however, provide some benefit when used for problem solving. For example, the value of mammography is often limited after breast augmentation, and in this situation, PET might offer some advantage in screening for cancer. Pet scans have sensitivity between 80 and 100 percent and a specificity between 75 and

85 [1].

Combining PET and dynamic MRI information in assessment of breast lesions found on mammography may decrease the number of biopsies of benign lesions, as the high specificity of PET complements the high sensitivity of dynamic breast MRI.

Currently, a few research centers are evaluating dedicated positron emission mammography devices that may potentially improve identification of small breast cancers.

Pet scanners are quite expensive and not widely available, and the agents used are expensive to make and last only a short time.

1.2.7 Thermography

Thermography has been approved by the United States FDA since 1983 for the adjunctive screening of breast cancer. Infrared thermal imaging has been used for several decades to monitor the temperature distribution over human skin. Abnormalities such as malignancies, inflammation and infection cause localized increase in temperature that appear as hot spots in an infrared camera. This technique was largely abandoned in 1970s because of inconsistent results and no scientific general consensus. High rate of false positive and low sensitivity (from 39 to 89 percent) caused thermography to drop early in the study. However, technological developments in recent years have sparked new interest in the technique.

1.3 Emerging Breast Imaging Technologies

A wide variety of new technologies, including alternative imaging modalities, geneticmarker techniques, improvements in X-ray mammography, and novel biological assays that would enhance, complement or replace mammography, are being investigated in hopes of improving early-detection rates. Screening is also the primary role foreseen for most of the alternative imaging modalities now being developed. The potential usefulness of alternative imaging is not, however, restricted to screening; it may also contribute to the characterization of breast abnormalities detected by mammography and other means, including BSE and CBE.

Some alternative imaging methods do not yet achieve the high-resolution structural imaging offered by conventional mammography. While this would be desirable, there are good reasons for trading some spatial resolution for other

information. In particular, providing the radiologist with alternative tools for evaluating patient populations not well-served by mammography and expanding the diagnostic information available to the radiologist in clinically suspicious cases are important goals not dependent on high spatial resolution as such.

For example, imaging methods that are sensitive to functional malignant features such as angiogenesis or thermogenesis could be exploited in an adjunctive role to improve the specificity of mammographic diagnosis. In addition, X-ray mammography has been repeatably found not to detect 10-30% of cancers greater than 5 mm in diameter, largely due to its relatively poor soft-tissue contrast [10]. This is particularly true for radiologically dense breasts, which are more common in younger women.

Spatial resolution may thus not be the limiting factor for detecting certain mammographic abnormalities, and so should not be the most important concern in the development of alternatives to current breast-imaging technologies. Most of the new imaging technologies are in the field of microwaves.

Below, we briefly indicate the physical basis of each emerging imaging modality in the field of microwaves after a short summary on the motivation of microwaves in medicine and in particular for breast cancer detection.

1.3.1 Microwaves for Breast Cancer Detection

Exciting prospects for innovative microwave sensing technologies to address diagnostic needs in medicine have been brought by the dawn of the 21st century.

A wide numbers of medical applications of microwaves has been reported in the literature but the one that has obtained great interest over the past 10 years is breast cancer detection.

A renewed interest in clinical microwave diagnostics [11] can be explained on the basis of the improved performance of both instrumentation and computer modeling of complex systems.

When microwave methods are applied to the breast they have more chances of success because of a larger penetration depth and accessible location of external sounding sensor. A comparison between the left and the right breast is possible.

The breast is both anatomically accessible outside any major muscle wall, making it relatively low-loss environment for microwave sensing. It is small enough that the computing power required to model it more affordable than other organs.

Interest in imaging the breast with electromagnetic field in the microwaves has been also motivated by certain deficiencies in current screening and diag-

nostic practices based on X-ray mammography and by the nonhazardous nature of the EM energy at low levels.

Behind ongoing research, the knowledge of the large dielectric contrast of cancer relative to normal breast tissue found in historical studies of breast properties generated from ex-vivo experiments, has also given motivation in the research field of microwaves for breast cancer detection [12]. However, a large-scale study of the breast tissue dielectric properties revealed that the dielectric contrast is as large as 10:1 between malignant and normal adipose-dominated breast tissues while the dielectric contrast between malignant and normal fibroglandular tissues is non more than 10% [13].

The microwave frequency range makes researchers able to find a trade off between the demands of penetration depth and imaging resolution.

All these are the reasons why microwave imaging has obtained such strong interest as an alternative non-ionizing breast imaging modality and why microwave imaging research has been addressed to the specific problem of the early breast cancer detection.

Works on active microwave techniques for breast cancer detection include narrowband and wideband inverse scattering techniques (*microwave tomography*), *ultrawideband beamforming* and other impulse-based techniques such as time reversal (*microwave radar*), hybrid techniques such as *microwave-induced thermoacoustic tomography*, *microwave imaging with mechanical or acoustic excitation*, and *microwave holography*. Realistic three-dimensional models MRI derived for FDTD simulations of the breast and different clinical prototypes and phantoms for active microwave imaging of the breast have been presented in different works during the last years [14],[15],[16].

Currently microwave radiometry is the only one passive technique in the field of microwaves.

All these emerging techniques are painless, don't compress the breast, don't use ionizing radiation. They also work equally well for women of all ages, including young women with dense breasts and should provide quantitative data that can reduce the interpretive variability associated with mammography. All these modalities have been rendered feasible by the recent explosion in low-cost computational power.

1.3.2 Active Microwave Technologies

Microwave tomography is a technique that uses the differential water content of cancerous tissue versus that of noncancerous tissue to detect tumors. Several microwaves transmitters illuminate the breast. The back-scattered signals are

collected via antennas positioned around the breast and they are compound to produce a three-dimensional image of the dielectric profile of the breast by solving an inverse scattering problem based on nonlinear image reconstruction algorithms. It has several attractive features.

On the other hand, a unique solution of the inversion algorithm, sufficient resolution of the inverted solution, a low computational burden and a low time-consuming in the reconstruction algorithms are desirable and can be considered challenges for the improvement of such a technique.

For years, active microwave imaging technologies have been motivated by the large dielectric contrast malignant-to-normal tissues. Recently breast tissue dielectric properties have been characterized in the frequency range between 0.5 and 20GHz in a large-scale study with well documentated protocols. The dielectric contrast has been found to be as high as 10:1 in fatty breast tissue but no more than 10% in fibroglandular tissue [13]. Despite this finding, researchers have shown in recent works the there are some evidences demonstrating that promises of active microwave techniques haven't fallen down.

Initial clinical experience[15] on microwave breast imaging has been shown that average values from in-vivo images agree with those observed in [13]. This would mean that the contrast between malignant-to-normal breast tissues was apparent.

Despite the evidence of higher values of dielectric properties in denser breast tissues than historically appreciated there are some encouraging evidence for image contrast in cancer based on spatial discrimination of tissue dielectric properties in the microwave range ($\sim$ 1GHz) on the 10mm scale. In cases of breast abnormalities that where subsequently biopsied, cancer contrast was 2:1 on average relative to the normal breast in electrical conductivity and 1.2:1 on average in relative permittivity when lesions greater than 1cm were evaluated.

It appears that the relative permittivity is proportional to the total water content and scales proportionally with fat vs. fibroglandular tissue vs. cancer where the latter demonstrate a modest increase in total water. The electrical conductivity, on the other hand, may represent the proportioning of total water into its free and bound compartments where the latter is elevated in both cancers and fibroglandular tissue (relative to fat) but the former is much more prevalent in cancer and creates the threshold change in conductivity observed (i.e. large proportional increase in free or extracellular water content) even when the total water content (and, therefore permittivity) may only be modestly elevated [16].

Nonlinear methods are required to estimate the distribution of electrical properties that exist within tissue based on measured responses to applied EM exposures. The imaging problem cannot be linearized because of the nonlinear

relationship between the dielectric profile and the scattering response due to etherogeneity of the breast interior. The inverse electromagnetic problem in the image reconstruction process is nonlinear and also ill-posed. An iterative electromagnetic time-domain inversion algorithm is usually used. Efforts are currently made in order to overcome the illposedness and to improve the resolving ability of the algorithm using regularization procedures based on introducing constraint on the reconstructed image and including a priori data of the shape and dielectric properties of the object being imaged [17],[18],[19].

Global optimization algorithm such as Genetic Algorithm (GA)[20] and Particle Swarm Optimization (PSO)[21] have been used to eliminate the risk of getting trapped in a local minimum. But global methods usually suffer from an expensive computational burden. For this reason efforts are being made to reduce computational runtime [22].

Different regularization technique have been employed in the context of two-dimensional [23] and three-dimensional [24] breast imaging problems. Benefits of a bound-constrained inverse solution are shown in [25]. The imaging array, therefore is a critical part in the EM imaging system design because of the need of elements coupled to the breast through a comfortable exam interface that produces reliable and high fidelity measurements of the EM signals.

Since the majority of breast tumors originate within fibroglandular tissue, new efforts are being addressed to enhance the dielectric contrast. The feasibility of air-filled microbubbles as contrast agents (such as the ones used as ultrasound contrast agents) for enhancing the malignant-to-normal dielectric contrast are being investigated. Initial numerical studies suggest that the presence of microbubbles reduces the effective dielectric properties of the tumor by as much as 30% thus improving detection via differential (pre- and post- contrast) imaging [26]. Impact to these dielectric properties (modified by contrast agents) on microwave images for 3D anatomically realistic numerical breast phantom using an inverse scattering algorithms is being explored.

Ultra wideband microwave radar technique (UWB) is another microwave technique that has grown in recent years as a promising technique for breast cancer detection. In 1998, Hagness and colleagues introduced a pulsed radar system for breast tumor detection. This was the first medical application of technology that previously has been used predominantly for detection of land mines and detection of concealed weapons at airports.

This method avoids nonlinear inverse scattering techniques that may be complex and computer intensive. However, it does not provide profiles of the permittivity, but only identifies regions of increased scattering due to a small region of different permittivity. To acquire the data, the breast is illuminated

with an ultra-wideband pulse, and the same antenna collects the backscattered waves. This process is repeated for multiple antenna positions. A time-shift-and-add algorithm is applied to the set of pulses recorded at the antenna output in all positions. The time delay for the round trip to a given point in the test domain is computed for each antenna position. Next, the signals with the appropriate time delays are summed up. The focal point is scanned to a new location and the focusing process is repeated. The basis for tumor detection and location is the difference in the electrical properties of normal and malignant breast tissues when exposed to an incident electromagnetic field at microwave frequencies (300MHz-30GHz) [27], [28],[29],[30].

This procedure ensures that signals from a given pixel or voxel in the test domain add coherently. Signals from scatterers in other locations add incoherently, which tends to reduce clutter. Thus, a small scatterer can be picked up, if it has sufficiently large contrast compared to a random heterogeneity within the test domain. The same principle is used in several synthetic aperture ground penetrating radar systems. One of the significant advantages of this approach is that high resolution can be obtained provided that a sufficiently wideband pulse can be used.

Thermoacoustic tomography exposes the breast to short pulses of externally applied electromagnetic energy. Differential absorption induces differential heating of the tissue followed by rapid thermal expansion. This generates sound waves that are detected by an array of ultrasonic transducers positioned around the breast. Tissues that absorb more energy expand more and produce more sound. The timing and intensity of the acoustic waves are used to construct a three-dimensional image of the irradiated tissue. The electromagnetic wave pulse, the acoustic properties of the tissue, the geometry of the ultrasonic detector array, and the image reconstruction algorithm determine the spatial resolutions of the images.

Indirect microwave holography consists of illumination of the object with a source of microwave radiation. Then, an intensity pattern formed by combining the scattered signal from the object with a reference signal is recorded. At optical frequencies, image reconstruction is performed by re-illuminating the hologram with the original reference signal. Problems associated with providing an offset reference wave prove this technique difficult to be adopted. The potential of this approach is demonstrated in [31].

1.4 Microwave Radiometry - State of Art

Microwave Radiometry exploits the natural electromagnetic emission by any object (e.g. living tissue) with a temperature above to absolute zero [32],[33],[34],[35], [36],[37],[38],[39]. The type of instrument that is used to receive the radiation from the object is normally referred to as a radiometer.

Microwave Radiometry is well assessed as a monitoring tool in remote-sensing geophysical applications with a nondense medium often sensed by a remote antenna [40]. For studies of properties of the troposphere, e.g. temperature and water vapor profiles, and for properties of the stratosphere, e.g. ozone profiles, the radiometer is highly suitable since atmospheric gases are having absorption resonances and consequently emission of radiation. Over the last 25 years, it has also been proposed as a noninvasive, completely passive technique for temperature measurements within nonaccessible dense bodies in view of medical application.

Interests to microwave radiometry in medicine comes from the possibility to derive informations related to the thermal status of subcutaneous tissue to a depth of some centimeters from the detection of the passive emission of microwaves by the tissue.

In this case the radiation can be received by antennas placed on the tissue surface, so that the antenna near-field is generally involved in sensing [41]-[42]. By listening to the broadband thermal radiation at one or more frequency band, the radiometer converts the received energy to an equivalent temperature averaged over a volume of tissue that depends on the radiative/receive pattern of the antenna. Listening at microwaves frequencies in the range of 1-5GHz, the EM signal from the body is extremely weak (on the order of picowatts). This makes it extremely important to design antennas that can collect the signal as efficiently as possible.

The greatest intensity of radiation is in the infrared according to the Planck law, but high attenuation of tissue in this range limits application of the infrared thermography to measurements of skin temperature only. In the microwave frequency range the intensity of radiation is about ten million times lower but attenuation of tissue is low, too.

In clinics, microwave radiometry has been considered in the attempt to cope with two major challenges, i.e. noninvasive temperature monitoring and early detection of tumor malignancies. First-type applications range from non-invasive monitoring of subsurface temperatures during hyperthermia treatments [43], [44] e [45] ,[46], or long-term monitoring of thermal abnormalities like mild hypothermia of newborn infant brain [47],[48] to non-invasive temperature mon-

itoring for feedback control of hyperthermia treatments [49]. The application of microwave radiometry to the detection of a tumor has been investigated since 1977 [50],[51],[52],[53],[54] also in connection with the problem of retrieving a temperature profile from a set of radiometric data for detection of cancer in breast [55],[56],[57], brain [58] and thyroid [59]. In spite of some positive evidence, however, microwave radiometry has not yet reached a general consensus as a screening modality for early cancer detection although recent results seem encouraging [60].

A full 3D model that relates radiometric data to the temperature changes between a normal and malignant breast is not yet available. We have developed this model and discussed it in Chapter 3 in order to derive requirements for a tumor to be visible by an ideal radiometer and antenna, i.e. maximum detectable depth and minimum detectable temperature gradient.

Most of the research groups used radiometers operating at lowgigahertz frequencies, with antennas consisting of openended rectangular waveguides [61], [62], [33] or small-loop antennas placed against the skin [63]; one group used millimeter frequencies with a horn antenna and dielectric lens [64]. Increased information about the spatial extent and location of thermal hot-spots has been obtained using multiple antennas [33], multiple frequencies [65] or sophisticated correlation techniques [66]. Multispectral radiometry is considered with the purpose of reconstructing profiles of subcutaneous temperature from sets of radiometric measurements taken at different frequencies [67],[55]. The inverse problem is ill conditioned, and proper inversion techniques must be used to prevent numerical instabilities in the temperature retrievals. The singular function method has been considered as an inversion technique particularly useful when a low number of measurements is available [68]. The stability of the solution against the measurement noise can be additionally improved by use of Kalman filtering which allows temporal variations to be inserted in the retrieval scheme.

The current work is an in depth analysis of the capabilities of a radiometric system operating with one antenna at one frequency. This thesis aims at finding a correlation of the radiometric data with the presence of a disease-related temperature differential and not to retrieve temperature.

A dual-mode microwave transceiving antenna for simultaneous heating and noninvasive thermometry of superficial tumors like the chestwall recurrence of breast cancer has been investigated [69].

The high gain in the boresight direction makes the Archimedean spiral a candidate for sensing weak thermal noise levels at depth in tissue. The Archimedean spiral antenna element, on the other hand, produces a narrow, centrally peaked, "pencil beam" shaped radiation pattern. Spiral antenna has shown to be good

candidate for this application, being well matched to both the human body and feedlines over a broad band of frequencies in addition to being reasonably efficient. Characteristics of microstrip muscle-loaded single-arm archimedean spiral antenna are presented in [70] but no experimental results of prototypes application on tissues can be found in the literature.

Some microstrip antennas have been designed to operate with the breast in a radiometric application. These antennas are described in details in Chapter 5.

1.4.1 Rationale for breast cancer detection

Since (fast-growing) tumors can exhibit local temperature elevation over surrounding normal tissues [71], microwave radiometry has shown promise as a possible diagnostic tool for early breast cancer detection [54]. It is therefore a promising instrument for the diagnosis of diseases involving a temperature variation within the tissues for example due to inflammatory processes and changes in blood flow.

The goal of this work is to investigate the feasibility of microwave radiometry as a modality for early-stage breast cancer detection.

Cancerous tumors have an abnormal cellular metabolism (thermogenesis). In simple terms their energy systems work differently in comparison with a healthy cell. They have a metabolism that is dependent on glucose and thus require a network of vascular tissue to enable them to survive. Tumor thermogenesis and the development of this vascular network called angiogenesis are a very early indicators that a tumor is present in the tissues. It appears even before signs of breast cancer are detectable by either self-exams or mammograms. Since these changes cause an increase in the temperature of the tumor area with respect to the surroundings, microwave radiometry can be exploited to detect this (tumor) over-temperature.

As a screening modality it can improve the sensitivity of the mammographic results. The potential usefulness of this alternative modality could not, however, be restricted to screening. Being sensitive to functional malignant features such as angiogenesis and thermogenesis, passive microwave radiometry could be exploited in an adjunctive role to improve the specificity of mammographic diagnosis by the characterization of breast abnormalities detected by mammography. In other words it can complement the mammography information on the morphological nature of the tumor with an information concerning the physiological nature of malignancies.

Being a passive detection modality, it does not require exposure to radiation

and so it is both safe and entirely nonhazardous. Unlike active modalities described in the previous section it may also be used for young women with denses breast.

The potential use of microwave radiometry as a screening tool and the fact that it can be used with absolute safety on women from a young age are important as well to increase the reliability of mammography in terms of sensitivity and specificity thus limiting the number of false-positives and false-negatives.

Chapter 2

Microwave Radiometry: Basic Principle

2.1 Microwave Radiometry

The passive microwave thermography or, concisely, radiometry, is based on the measurement of thermal radiation emitted by any body at higher temperature than absolute zero. The intensity of this emission is dependent on temperature and is highly variable within different spectral bands. The largest intensity of radiation is in the infrared range, but high attenuation of tissue in this range limits application of infrared thermography only to measurements of skin temperature.

The radiation intensity in the microwave band is about ten million times lower but attenuation in tissue is lower. Moreover in this range the intensity of radiation is directly proportional to absolute temperature so microwave radiometry can be considered to allow detection and diagnosis of pathological conditions in which there are disease-related temperature differentials.

Thermal radiation leaving from a biological body is attenuated by each crossed layer of tissue. Moreover it is reflected and refracted at the interfaces between different layers. A crucial limitation of microwave radiometry is the extremely weak signal level of the thermal noise emitted by the lossy material (10^{-15} Watts).

For anatomical depths of heat sources, computer simulations show that the maximum intensity of the received radiation is in the range between 1 and 5GHz.

Therefore radiometers working in this range are mainly used in research.

Microwave radiometers are highly sensitive receivers designed to measure thermal noise power. The function of a radiometer is to measure the temperature of a medium sensed by an antenna connected to its input. This temperature represents the average value of a fluctuation noiselike signal. The smallest change in the load temperature that can be detected by a radiometer is referred to as radiometric resolution (sensitivity) and characterizes the performance of a microwave radiometer.

Considering the methods of thermal noise measurement, microwave radiometers can be divided into two groups: total power (compensatory) radiometers and modulation radiometers (Dicke radiometers).

2.1.1 Total Power Radiometer

Consider the total power radiometer system shown in Fig.2.1a. The antenna is connected to a superetherodyne receiver of bandwidth B and total power gain G followed by a detector and a low-pass band filter. The power delivered by the antenna usually is broadband noise extending over a wider bandwidth than the receiver bandwidth B. The function of the RF amplifier is to filter the input signal by amplifying the frequency components contained in the bandwidth B centered at the RF frequency of interest. The mixer and the IF amplifier translate the RF band of signals of bandwidth B to the same bandwidth at the IF and provide further amplification. Such a system consisting of RF-to-IF translation of a single band of width B is called *single-sideband* receiver.

A diode detector gives a relatively accurate method of determining RF power delivered to a load, for powers above about 100mW. Measured DC voltage is simply equal to the peak voltage of the RF waveform: power in watts may be determined by calculating $V_{peak}^2/100$ (for 50-ohm systems). Square-law simply means that the DC component of diode output is proportional to the square of the AC input voltage i.e., the diode detector operation region is square-law for signals below $-20dBm$.

The low-pass filter (integrator of integration time τ) filters out the high-frequency fluctuations of the detected voltage which is equivalent to averaging the square-law detector output over some interval of time τ. In terms of smoothing (filtering) out the ac fluctuations an ideal integrator is equivalent to an ideal low-pass filter if the integration time is equal to the reciprocal of twice the bandwidth of the ideal filter.

A representation equivalent to Fig.2.1a is shown in Fig.2.1b in which the antenna is replaced by a noise source with output power $P_A = kT_AB$ and the

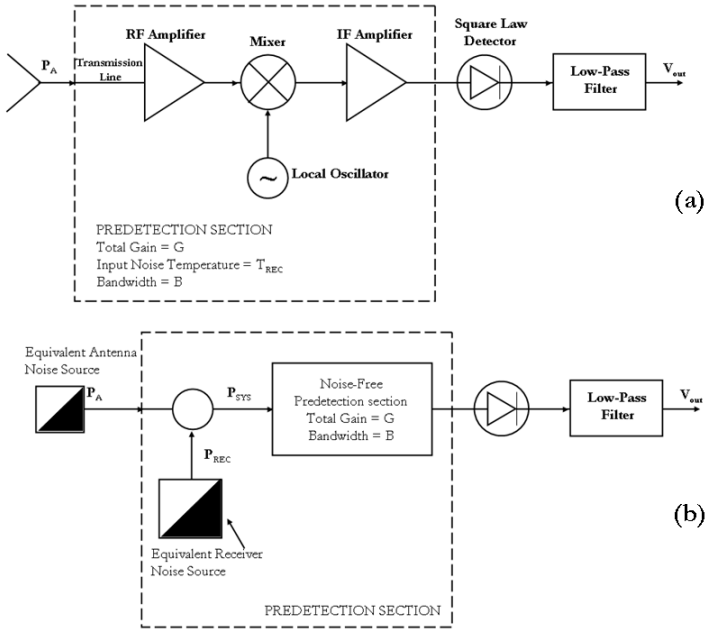

Figure 2.1: Total-Power Radiometer block diagram a) and its equivalent b).

receiver (including transmission line) is replaced by a combination of a noise-free receiver and an input noise source with output given by $P_{REC} = kT_{REC}B$, where T_{REC} is the equivalent input noise temperature of the transmission-line-receiver combination. The total system input noise power is:

$$P_{SYS} = P_A + P_{REC} = kT_{SYS}B \tag{2.1}$$

where:

$$T_{SYS} = T_A + T_{REC} \tag{2.2}$$

The IF amplifier (average) output power P_{IF} is given by:

$$P_{IF} = GkT_{SYS}B \tag{2.3}$$

We denote with ΔT_{SYS} the standard deviation associated with the measured (estimated) value of T_{SYS}.

From an observation standpoint, ΔT_{SYS} may be viewed as the minimum change in T_{SYS} that is necessary to produce a detectable change at the radiometer output, where detectable change is defined as a change in the dc level of the output voltage equal to the standard deviation of the ac component. Recalling that $T_{SYS} = T_A + T_{REC}$:

$$\Delta T = \Delta T_{SYS} = \frac{T_{SYS}}{\sqrt{B\tau}} = \frac{T_A + T_{REC}}{\sqrt{B\tau}} \tag{2.4}$$

where ΔT is regarded as the minimum detectable change in the radiometric antenna temperature T_A of the observed scene. The above equation defines the radiometric sensitivity of an *ideal* total-power radiometer with no gain fluctuations. This assumption is not always valid. To emphasize the importance of this assumption, ΔT will be denoted ΔT_{IDEAL}.

2.1.2 Effects of Receiver Gain Variations

The expression of ΔT accounts only for the measurement uncertainty due to noise fluctuations and does not incorporate receiver gain fluctuations. Gain variations in the predetection section arise primarily from the RF amplifier and secondarily from the mixer and IF amplifier. Since the output signal is linearly related to the product $G(T_A + T_{REC})$, where G is the average system power gain, an increase in G will be misinterpreted by the output as an increase in $T_A + T_{REC}$. Long term (slow) variations of G, with periods of the order of minutes, may be factored out approximately by calibrating the radiometer as frequently as is practicable. However, calibration doesn't eliminate short-term (fast) gain variations that occur over intervals smaller than the period between successive calibrations.

Since the noise uncertainty ΔT_N and the gain uncertainty ΔG are caused by unrelated mechanism, they may be considered statistically independent. In this case the total rms uncertainty is given by:

$$\Delta T = \left[(\Delta T_N)^2 + (\Delta G)^2\right]^{\frac{1}{2}} = (T_A - T_{REC}) \cdot \left[\frac{1}{B\tau} + \left(\frac{\Delta G}{G}\right)^2\right]^{\frac{1}{2}} \tag{2.5}$$

The above expression defines the radiometer sensitivity of the total-power ra-

diometer incorporating the effects of both noise and gain variations. Gain variations are often the limiting factor to achieving high radiometric resolution.

Even with a noise-free receiver ($T_{REC} \simeq 0$) a resolution of 1K cannot be achieved without improving the gain variation factor $\frac{\Delta G}{G}$. Typically the gain variation factor for low-noise microwave amplifiers is between 10^{-2} and 10^{-3}. Gain variations may be reduced by an order of magnitude by controlling the sources that cause these variations, namely, power-supply voltages and environmental temperature variations. One possible solution to the gain variations problem is to use a receiver with no RF amplifier. In this case values of $\frac{\Delta G}{G}$ low as 10^{-4} to 10^{-5} are achievable.

2.1.3 Dicke Radiometer

In 1946, the gain-variation problem was alleviated by Dicke through the use of modulation techniques. A block diagram of the Dicke radiometer is shown in Fig.2.2. It is basically a total-power radiometer with two additional features: (1) a switch, which has become known as a "Dicke" switch, connected at the receiver input at a point as close to the antenna as possible, and used to modulate the receiver input signal and (2) a synchronous demodulator (or synchronous detector) placed in between the square-law detector and the low pass filter (integrator). The modulation consists of periodically switching the receiver input between the antenna and a constant (reference) noise source at a switching rate higher than the highest significant spectral component in the gain variation spectrum. That is, the switching rate is chosen so that over a period of one switching cycle (typically between 1 and 20ms) the system gain is essentially constant and therefore identical for the half-cycle during which the receiver is connected to the antenna and the half-cycle during which the receiver is connected to the reference source.

The synchronous demodulator consists of a switch that operates in synchronism with the input Dicke switch, followed by two unit-gain amplifiers (in parallel) with opposite polarity to receive the voltage output corresponding to the antenna and comparison-source power respectively. The unit-gain amplifier outputs are then summed and fed into the low-pass filter (integrator).

We shall derive an expression for the radiometric resolution ΔT of the Dicke radiometer:

$$\Delta T = \left[(\Delta T_{NANT})^2 + (\Delta T_G)^2 + (\Delta T_{NREF})^2\right]^{\frac{1}{2}} \tag{2.6}$$

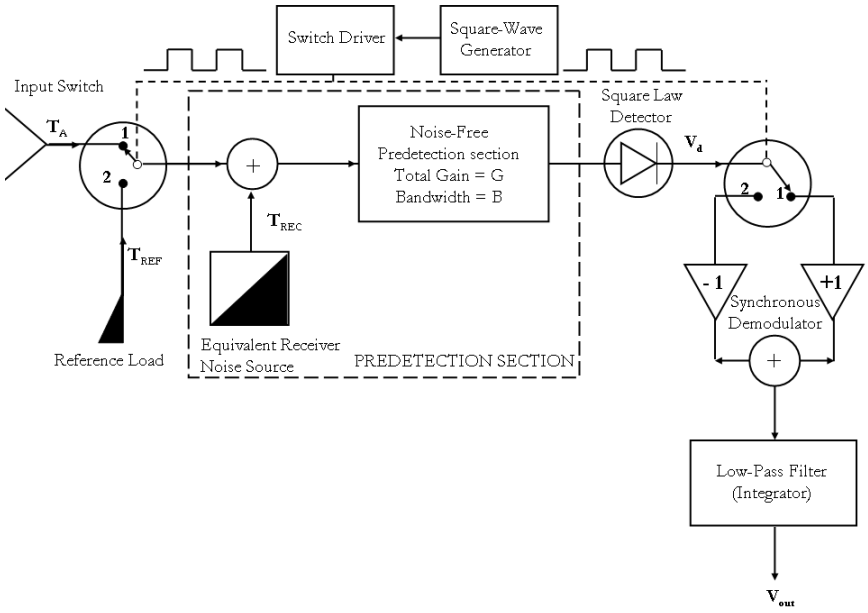

Figure 2.2: Block diagram of a Dicke Radiometer.

which reduces to:

$$\Delta T = \left[\frac{2(T_A + T_{REC})^2 + 2(T_{REF} + T_{REC})^2}{B\tau} + \left(\frac{\Delta G}{G} \right)^2 (T_A - T_{REF})^2 \right]^{\frac{1}{2}} \tag{2.7}$$

where T_{REF} is the reference-source noise temperature. The above expression will be referred to as the radiometric resolution of the *unbalanced* Dicke radiometer. Overall, the radiometric resolution of the unbalanced Dicke radiometer is superior to that of the total-power radiometer. When the condition $T_A = T_{REF}$ is met the second term inside the square brackets goes to zero, thereby eliminating the effects of gain variations all together and the radiometer is said to be *balanced*. In this case ΔT reduces to:

$$\Delta T = \frac{2(T_A + T_{REC})}{\sqrt{B\tau}} = 2\Delta T_{IDEAL} \tag{2.8}$$

or twice the theoretical sensitivity of an ideal total power radiometer (free of gain variations). The factor 2 comes from the fact that T_A is observed for only half the time.

2.1.4 Balancing Techniques

The balanced condition of the Dicke radiometer may be realized by either: (1) adjusting T_{REF} to equal T_A (or vice versa) prior to the input switch, or (2) controlling the predetection gain of the outputs due to the antenna and reference source separately, in such manner that the two voltage outputs are made equal. In the first case a feedback loop is used to control the magnitude of T_{REF} so that it continuously balances the antenna temperature T_A. This is realized by feeding the integrator output into a control circuit that applies the necessary voltage (or current) to an electronically controlled variable attenuator to maintain a null at the integrator output. The reference noise temperature T_{REF} is in part due to the noise generated by the noise source and in part due to self-emission by the attenuator:

$$T_{REF} = \frac{T_N}{L} + \left(1 - \frac{1}{L}\right) T_0 \tag{2.9}$$

where T_N is the noise temperature of the source, L is the loss factor of the attenuator and T_0 is its physical temperature. As a function of L, the limiting values of T_{REF} are $T_{REF} = T_N$ for $L = 1$ (no attenuation) and $T_{REF} = T_0$ for L very large. Conceptually, T_N and T_0 can be specified so that the range between them covers the range of values over which T_A is expected to vary. In practice, however this specification cannot be realized with passive noise sources unless cryogenic cooling is used. For real, variable attenuators the loss factor L cannot be reduced all the way to unit.

A null balancing condition can also be achieved through the use of noise injection into the line connecting the antenna to the input switch. To balance the reference load, a sufficient amount of noise power is injected into the antenna port through a directional coupler so that the input noise temperature T'_A appearing at the input switch is equal to T_{REF}.

Diode attenuators are most stable in their extreme ON and OFF states. When operated in only one or the other of these two states (by controlling the

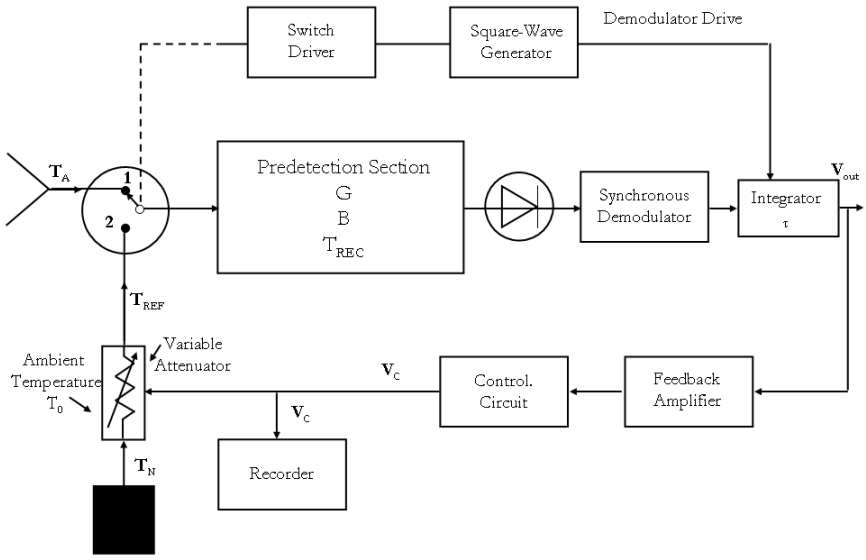

Figure 2.3: Dicke Radiometer using feedback to control the reference noise temperature.

magnitude and polarity of the bias voltage), a PIN diode attenuator becomes ON/OFF switch; in the ON position it causes minimum attenuation ($\simeq 2.0dB$), and in the OFF position it causes maximum attenuation (typically 60 dB). The injected noise is generated in the form of narrow rectangular pulses rather than continuously.

The balanced condition was realized in the methods considered thus far by adjusting the noise temperature of the reference channel to equal the noise temperature of the antenna channel, or vice versa, at the input switch. Another way to effect balance is by modulating the gain of the IF output voltage prior to the square-law detector. The modulation consists of switching the IF output between a constant attenuator and a variable attenuator for the alternate half cycles of the input switch. The function of the feedback loop is to control the variable attenuator so that its output voltage (corresponding to the reference channel) is equal to the output voltage of the fixed attenuator (corresponding

to the antenna channel).

This kind of balanced condition described above has some drawbacks. Slow variations in the receiver noise temperature T_{REC} (between calibrations) result in a measurement error of the absolute value of T_A due to the dependence of the control circuit voltage on T_{REC}. In contrast the techniques employing temperature control to balance the radiometer are insensitive to drifts in T_{REC}. Another limitation of the gain-modulation technique is that it can produce excessive output fluctuations if the amplitude gain modulation is large.

Thus, for low-noise receivers (relatively small T_{REC}) the gain modulation method is useful over a narrow range of the difference $T_{REC} - T_A$.

2.2 "Tor Vergata" Radiometer

Our radiometer is similar to a balanced Dicke radiometer with a feedback to control the reference noise temperature (see Fig.2.4 and Fig.2.5). In addition there are two internal reference temperatures so that the reflectivity can be estimated in addition to temperature. The presence of two internal temperature references makes the "Tor Vergata" radiometer a four-state radiometer. The reference noise temperatures T_{REF_1} and T_{REF_2} are set by the noise source depending on whether the noise generator is turned on or off through a control signal.

Fig.2.4 shows a block diagram of the "Tor Vergata" radiometer.

A feedback loop is used to switch the the reference temperature between two states so that it balances the antenna temperature T_A. This is realized by feeding the integrator output into a control circuit that applies the necessary voltage (or current) to an electronically controlled variable attenuator to maintain a null at the integrator output. Another loop is used to swithc the receiver input signal between the antenna and the reference noise source as in an unbalanced Dicke radiometer.

As a consequence there are two control signal. ck1 switches the receiver input between the antenna and a constant (reference) noise source at a switching rate higher than that of ck2 that switches the noise generator between the ON/OFF states. Also the synchronous demodulator switch is controlled by ck1.

When ck1 is in the 0 position (see Fig.2.5) it causes the receiver input to be the signal from the reference noise source which can be in the ON/OFF state depending on whether ck2 is in the 0/1 position. When ck1 is in the 1 position it causes the receiver input to be the signal from the antenna.

If we consider ideal microwave components and neglect the insertion losses, the voltage output signal due to the four states are:

STATE 1: **ck2 = 0** (noise generator OFF), **ck1 = 1** (antenna)

$$V_1 = kG\Delta f T_x(1-\rho) + \rho kG\Delta f T_{REF_1} \tag{2.10}$$

STATE 2: **ck2 = 0** (noise generator OFF), **ck1 = 0** (internal reference)

$$V_2 = kG\Delta f T_x(1-\rho) + \rho kG\Delta f T_{REF_2} \tag{2.11}$$

STATE 3: **ck2 = 1** (noise generator ON), **ck1 = 1** (antenna)

$$V_3 = kG\Delta f T_{REF_1} \tag{2.12}$$

STATE 4: **ck2 = 1** (noise generator ON), **ck1 = 0** (internal reference)

$$V_4 = kG\Delta f T_{REF_2} \tag{2.13}$$

where G is the averaged channel gain over the receiver bandwidth Δf, T_x is the load temperature and k is the Boltzmann constant. From the above expressions we can derive both temperature (T_x) and reflectivity (ρ):

$$\rho = \frac{V_1 - V_2}{V_3 - V_4} \tag{2.14}$$

$$T_x = \frac{V_1 T_{REF_1}(V_3 - V_4) - V_4 T_{REF_2}(V_1 - V_2)}{V_4\left[(V_3 - V_4) - (V_1 - V_2)\right]} \tag{2.15}$$

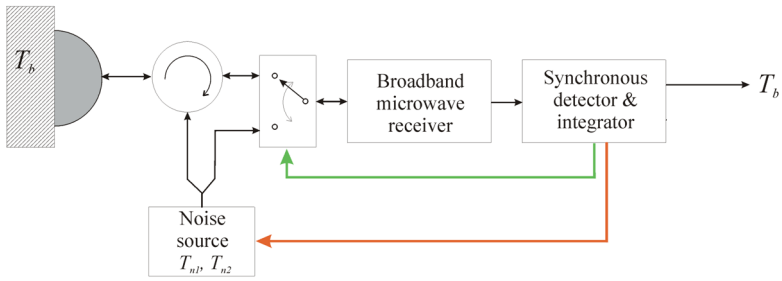

Figure 2.4: Block diagram of "Tor Vergata" radiometer with compensation of reflection coefficient.

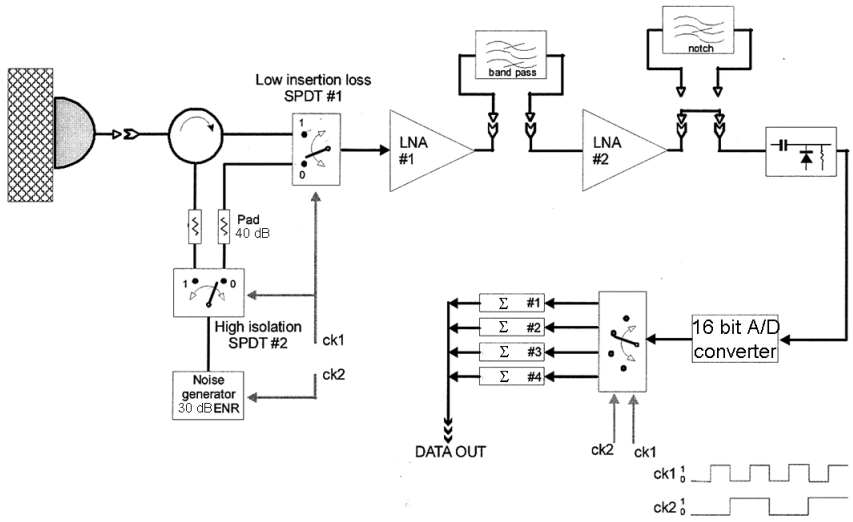

Figure 2.5: Radiometer electrical scheme.

2.3 The Radiometric Equation

Charged particles in motion in a body are sources of primary incoherent electromagnetic fields which propagate with absorption within the body. Some field however reaches the surface and radiates outside. In near-field radiometry a contacting antenna collects and transduces the impinging radiation into an electrical current which fluctuates in the input circuit of a receiver. Time-averaging fluctuating fields and currents gives zero. Second-order moments instead are different from zero [72]. In a radiation-balance microwave radiometer [73] the power from the antenna is compared with the power from an internal noise generator, providing samples P_n. The radiometer output, proportional to $\kappa B T_B$ (in Watt), is the average of samples P_n over the integration time τ_R. κ is Boltzmann's constant, B is microwave receiver bandwidth, and T_B is input temperature as seen from the receiver (brightness temperature in K). The standard deviation of samples P_n over τ_R is evaluated as $\kappa B \, \sigma_R$, where σ_R is referred to as radiometric resolution. When the power balance between body and receiver is modeled, the receiver is represented by a load resistance at temperature T_{REC}. At microwave frequencies under the assumption of thermal equilibrium, the power balance is:

$$T_B = eT_A + (1 - e)\, T_{REC} \tag{2.16}$$

where e , emissivity, is related to the reflection coefficient Γ at the interface between antenna and body by $e = 1 - |\Gamma|^2$. T_A, available temperature, is obtained from the physical temperature T (in K) by integration over the body:

$$T_A = \int_{\Omega} W(\underline{r}) T(\underline{r}) dV \tag{2.17}$$

where W is a non-negative function that weighs the elemental contributions and can be evaluated from the microwave power deposition pattern P_d (or specific absorption rate, SAR) when the antenna is radiating onto the body in active modality (the reciprocity theorem states that any subvolume of a material produces a radiometric signal equal to the absorbed radiation at the same frequency [74]):

$$W(\underline{r}) = \frac{P_d(\underline{r})}{\int_{\Omega} P_d(\underline{r}) dV} \tag{2.18}$$

Ω is the overall tissue volume that is sensed by the antenna. The input temperature as seen from the receiver therefore is:

$$T_B = e\frac{\int\limits_{\Omega} P_d(\underline{r})T(\underline{r})dV}{\int\limits_{\Omega} P_d(\underline{r})dV} + (1-e)T_{REC} \tag{2.19}$$

It is straightforward verifying that the previous equation holds independently of the zero of temperature.

In spite of the simplicity of the underlying rationale, measurements on patients may fail because inadequacies of the instruments and presence of artifacts due to spurious radiation. When the antenna explores the breast, in fact, the data may vary because any change in the antenna match causes a variation in the back reflection of thermal noise from the receiver. An ideal radiation-balance radiometer [73] prevents this drawback.

In an ideal radiation-balance radiometer the receiver resistance is adjusted to have $T_A = T_{REC}$, therefore we shall use:

$$T_B = \frac{\int\limits_{\Omega} P_d(\underline{r})T(\underline{r})dV}{\int\limits_{\Omega} P_d(\underline{r})dV} \tag{2.20}$$

for the input temperature. After a calibration, receiver gain and offset are set to have:

$$S_B = \frac{\int\limits_{\Omega} P_d(\underline{r})T(\underline{r})dV}{\int\limits_{\Omega} P_d(\underline{r})dV} \tag{2.21}$$

for the signal in output. S_B coincides with T when T is uniform throughout Ω.

2.4 Tumor Over-Temperature Rationale

The use of microwave radiometry in cancer detection is based upon the assumption that a temperature differential exists between a malignant tumor and the surrounding tissue.

A tumor may change the normal distribution of temperature inside breast $T(\underline{r})$ into a new temperature $T'(\underline{r})$ differing by ΔT $(\underline{r})$ from the normal temperature mainly in the tumor volume and in the surrounding tissue [71]. An elevated thermogenesis is considered responsible for this change. The anomalous metabolic generation rate is explained as due to higher energy efficiency of fermentation in cancerous cells. Moreover vascular changes are elicited in the tumor area resulting in increased microvessel density (angiogenesis). Experiments have been reported showing that the tumor temperature is larger than the venous temperature that, in turn, is larger than the arterial temperature. In addition peritumoral hyperthermia is observed, that is explained as heat transfer from tumor mainly by blood convection through veins. To estimate tumor over-temperature we modeled a mammalian tumor as a sphere of diameter D having thermal parameters (metabolic heat generation rate, blood perfusion rate, effective thermal conductivity) differing from those of normal tissue. The sphere is located at various depths in the range $1 \leq d \leq 4$ cm inside a homogeneous hemisphere of normal tissue. The chest wall backs this model of breast (see Fig.2.6a). The tumor size is varied in the range $6 \leq D \leq 12$ mm.

Tumor thermogenesis is modeled by a value q_m that is obtained from:

$$q_m \cdot \tau = C \tag{2.22}$$

where $C = 3.27\ W \cdot d/m^3$ and τ is the time (d, day) required for the tumor to double its volume [75]. The exponential law relating tumor diameter (in m) and doubling time is:

$$D = e^{2.134 \times 10^{-5}(\tau - 50)} \tag{2.23}$$

The remaining thermal parameters for the tumor are taken from [76] and [77] and listed in Tab.2.1. For the sake of simplicity the lesion is placed at some depth from the breast surface with its center in the radial line perpendicular to

tissue	$k(W/m \cdot C)$	$\rho_b c_b w_b (W/m^3 \cdot C)$	$q_m(W/m^3)$
normal breast	0.48	2400	700
tumor	0.511	$48 \cdot 10^3$	see Eqs.2.22,2.23

Table 2.1: Thermal parameters.

a) **b)**

Figure 2.6: Hemispherical model of the breast on a muscle box (thorax) a). Sagittal view b). D and d are tumor diameter and tumor depth respectively.

the chest (ζ-axis, with $\zeta = 0$ on the skin, see Fig.2.6b). This site is not the most common placement of a mammalian tumor, which instead is an upper lateral quadrant.

We assume that the temperature distribution within the breast satisfies the steady-state bio-heat equation [78]:

$$\nabla \cdot k\nabla T + q_m - \rho_b c_b w_b (T - T_b) = 0 \tag{2.24}$$

where k is effective thermal conductivity which includes the enhancement in conductivity due to perfusion, q_m is metabolic heat generation rate, ρ_b is blood mass density, c_b is blood specific heat, w_b is blood perfusion rate per unit volume of tissue, T_b is arterial blood temperature. The boundary condition at the hemispherical interface between breast and air is:

$$k\nabla T \cdot \hat{n}_a + h_a(T - T_a) = 0 \tag{2.25}$$

with $\hat{n}_a$ the unit vector in the direction of the external normal to the boundary, h_a an effective conductive heat transfer coefficient, and T_a room temperature.

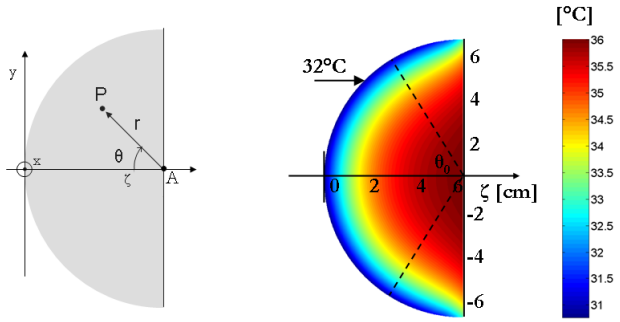

(a) (b)

Figure 2.7: Normal breast modeled as a hemisphere: (a) Principal plane with coordinates in use; (b) Temperature distribution map, sagittal view.

Eq.(2.25) is a linear heat balance at the skin. It models different heat exchanges to the environment such as conductive and convective heat transfer, linearized radiation, evaporation [79]. The temperature is continuous at the plane boundary between breast and chest at temperature T_c. In the most general case, h_a is a function of position on the surface and may account for patient's specificities like sweat and emotion.

The numerical values of the thermal parameters are listed in Tab.2.1 for normal breast [76]. We adopted $R = 6.5$cm for the breast radius, $T_a = 21°C$, $T_b = 37°C$, $T_c = 37°C$, $h_a = 13.5W/(m^2 \cdot^\circ C)$.

Numerical computations have been performed by Comsol Multiphysics, a finite element method simulation tool. The solution $T(\underline{r})$ to Eqs.2.24, 2.25 is shown in Fig.2.7 on a principal plane, i.e. a diametral plane normal to the chest. The skin temperature varies in the range $32 - 37°C$, the largest value being attained at the junction between breast and chest. As expected, the contribution of q_m to the normal breast temperature is negligible. The breast is heated by the entering blood and heat from the chest, while heat is lost by radiation towards the ambient. For later use we observe that the temperature does not depend on angle for radial lines within a cone of quite large angle with apex at the center of the hemisphere (Fig.2.7). Moreover the presence of a lesion will cause only local changes of temperature as we shall see.

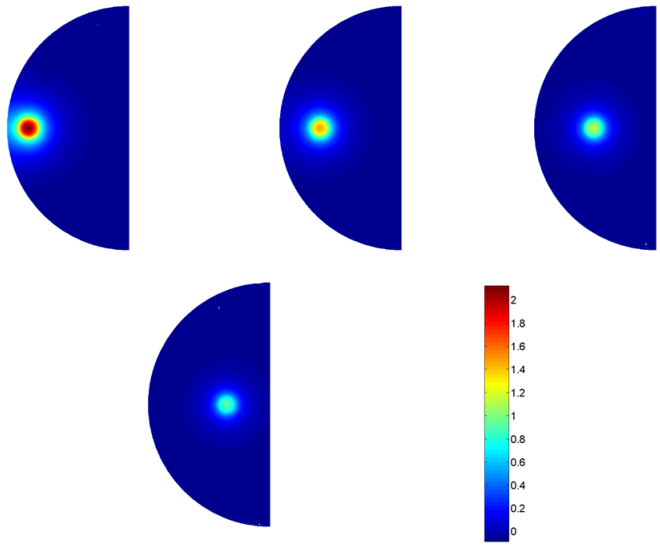

Figure 2.8: Temperature differential ΔT with respect to normal breast when a 10mm lesion is modeled at 1cm, 2cm, 3cm and 4cm depths from the skin.

To achieve some generality in the discussion of the results, therefore, the temperature will be related to the tumor depth, i.e. the distance of a tumor from the surface (skin). The results however properly apply to lesions with center in the ζ-axis for which the numerical analysis will be developed.

The over-temperature due to a lesion for standard room conditions does not exceed $1 - 2°$C depending on size and decreases with the distance from the breast surface where a radiation-type boundary condition [80] is imposed.

Diagrams of ΔT on a sagittal view of the breast are shown in Fig.2.8.

Diagrams of T and ΔT vs. depth are shown in Fig.2.9 for a 10mm lesion and a 12mm lesion respectively. The maximum $\Delta T_{\max}$ of $\Delta T(\underline{r})$, that is attained inside the tumor, is the highest difference in temperature between unhealthy and normal breast. For a 10mm tumor centered at 1, 2, 3 and 4 cm from the surface, we obtain $\Delta T_{\max} = 2.3, 1.58, 1.2, 0.97°C$, respectively. We find that the increase of temperature is lower for deeper locations of a tumor. This can be explained observing that when the perfusion term $-\rho_b c_b w_b(T - T_b)$ in the tumor core is < 0, it counteracts q_m and further increase of temperature. The perfusion

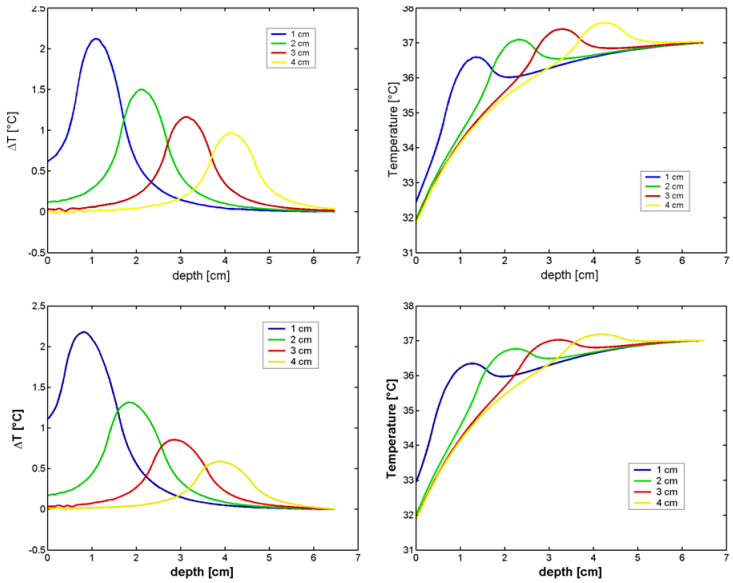

Figure 2.9: Temperature T and Temperature difference ΔT (unhealthy – normal) vs. depth on the median radial line through a tumor center, for various depths of a 10 mm lesion (top) and 12 mm lesion (bottom) respectively.

term instead is positive outside the core thus heating the tissue. The tumor angiogenesis, modeled as increased blood perfusion, clamps the temperature of the cancerous breast to the vicinity of T_b .

If we use the normal-breast perfusion rate also inside the tumor (in other words if we ignore angiogenesis) we get $\Delta T_{\max} = 1.36$, 1.30, 1.30, and 1.29 °C for the above distance from the surface. Neglecting angiogenesis causes the over-temperature be quite independent of depth.

If we instead neglect tumor thermogenesis taking only increased perfusion into account, the over-temperature respectively is $\Delta T_{\max} = 1.52$, 0.80, 0.44, and 0.36 $°C$ at the four locations, i.e., it is lower than that predicted by the full tumor model especially in depth, e.g., at 3cm $\Delta T_{\max}$ is 1/3 the temperature difference in the presence of thermogenesis. Similar results can be shown for a 12mm lesion (Fig.2.9).

Note that the largest difference of temperature is now 2.18, 1.31, 0.85, and 0.59 $°C$, respectively, at the four tumor placements. The tumor is larger but

the thermogenesis is lower.

The above results agree with the experimental result that a tumor affects the temperature in its proximity. Moreover an increased tumor perfusion affects the peripheral breast temperature to a larger extent, while an increased metabolic generation rate is more responsible of a temperature differential in relatively deep breast.

2.4.1 Apparent Thermal Volume

We introduce the apparent thermal volume of a breast tumor as the volume where the difference between unhealthy and normal breast temperature is $\geq 1°C$. Diagrams of the thermal apparent volume vs. depth are shown in Fig.2.10a for four diameters of a lesion. For lesions having diameter less than 10mm, q_m takes the value obtained from Eqs.2.22, 2.23 for D=10mm, which is the smallest diameter in [75] in the thermal model of a breast carcinoma. Higher values of q_m are generally associated to younger and smaller lesions, so the thermal visibility of these tumors is probably larger than that predicted by the results of our computations. It is interesting noticing from the diagrams that due to less effective thermogenesis, a peripheral larger tumor is thermally less visible than a smaller one before some depth.

Besides, we define the equivalent tumor diameter as the tumor diameter corresponding to its thermal apparent volume. Tab.3.2 shows the equivalent tumor volume for tumor of 12, 10, 8 and 6 mm diameter and for depths in the range $0.5 - 4.5$cm. It is interesting noticing from the table that due to apparent thermal volume, there is a significant difference between tumor real diameter and tumor equivalent diameter when tumor depth is lower than about 2cm.

The above numerical results have been obtained in the framework of a thermal model and a set of values for the breast thermal parameters found in the literature. Some assumptions, however, are questionable, i.e., the bio-heat equation neglects discrete vessels and the vascular bed may be non-uniform. As an example, an increased vascular density has been documented in the peripheral breast in some patients [81].

This occurrence makes lower the thermal visibility of a lesion. To model this in a simple way, we augmented the perfusion rate coefficient by a factor 3 in an external layer of the normal breast model. The results in Fig.2.11 refer to a layer of thickness t for t=1cm and 2cm. The apparent thermal visibility of a 10mm tumor is reduced in comparison with its visibility in the uniform perfusion case.

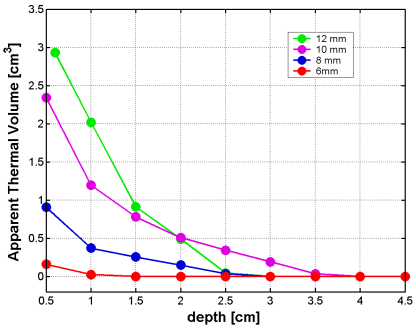

a)

Tumor Diameter (D)	Tumor Volume [cm^3]
12mm	0.91
10mm	0.52
8mm	0.27
6mm	0.11

b)

Figure 2.10: Apparent thermal volume of a lesion vs. depth a). Tumor volumes b).

	tumor depth (cm)								
D (mm)	**0.5**	**1**	**1.5**	**2**	**2.5**	**3**	**3.5**	**4**	**4.5**
12	26	23	17.6	14.4	6.7	0	0	0	0
10	24	19.3	16.6	12.8	10.8	5.6	0	0	0
8	17.6	13	11.6	8.4	6.2	0	0	0	0
6	9.6	5	0	0	0	0	0	0	0

Table 2.2: Equivalent tumor diameter. Orange (green) color highlights equivalent tumor diameter larger (smaller) than real tumor diameter.

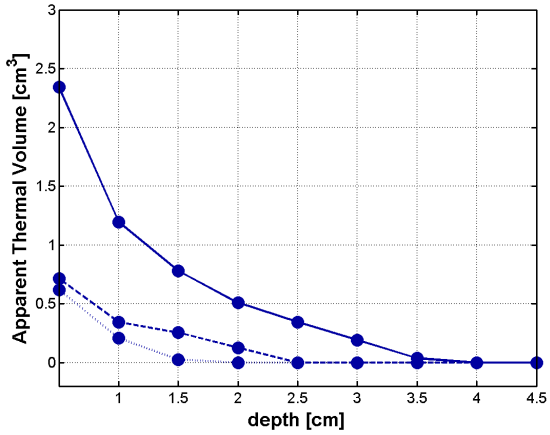

Figure 2.11: Apparent thermal volume of a lesion vs. depth for a 10mm lesion. Uniform perfusion (continuous line), increased perfusion in a 1cm superficial layer (dashed line), increased perfusion in a 2cm layer (dotted line).

2.5 How to collect radiometric data during a diagnostic application

During a typical diagnostic session a contacting antenna scans the surface of a non-isothermal lossy medium (breast) over different positions and receives the thermal radiation released by the tissue in the frequency range of the receiver which it is connected to.

If we suppose that the tissue is normal (Fig.2.12) the radiometric signal in output to the radiometer will be:

$$S_B = \frac{\int\limits_{\Omega} P_d(\underline{r}) T(\underline{r}) dV}{\int\limits_{\Omega} P_d(\underline{r}) dV} \tag{2.26}$$

according to Eq.(2.21).

If we suppose that a tumor is present in the breast (Fig.2.12) the signal in output to the radiometer will be:

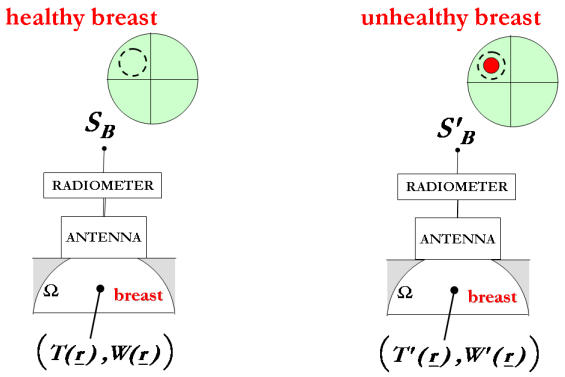

Figure 2.12: Simplified diagram of a radiometric measurement in a diagnostic application. Radiometric signal for normal (malignant) breast on the left (right). Red circle is the tumor, dashed line circle is the antenna contacted area.

$$S'_B = \frac{\int\limits_{\Omega} P'_d(\underline{r}) T'(\underline{r}) dV}{\int\limits_{\Omega} P'_d(\underline{r}) dV} \tag{2.27}$$

where the prime is used when there is a malignancy in the tissue.

As a consequence, the difference in the radiometric signals between malignant and normal breast denoted with ΔS will be:

$$\Delta S = \frac{\int\limits_{\Omega} P'_d(\underline{r}) T'(\underline{r}) dV}{\int\limits_{\Omega} P'_d(\underline{r}) dV} - \frac{\int\limits_{\Omega} P_d(\underline{r}) T(\underline{r}) dV}{\int\limits_{\Omega} P_d(\underline{r}) dV} \tag{2.28}$$

When a thermal anomaly is located within the radiation solid of the antenna, i.e. the volume of breast that contributes almost all the net real power entering the antenna from the breast, the receiver output increases to some amount ΔS. The anomaly is radiometrically visible if such amount is larger than the instrumental resolution.

This means that the signal corresponding to normal breast can be considered as the reference signal and any other signal related to the presence of a tumor

has to be compared with it. Moreover, the increment in received power due to a visible thermal anomaly must overcome the floor power due to thermal emission from normal tissue. In practice ΔS is the radiometer output after a calibration setting the instrumental offset equal to the signal of the normal breast.

In the next chapters we will show that ΔS is proportional to tumor over-temperature ΔT with respect to normal breast tissue according to the following equation:

$$\Delta S = \alpha \Delta T \tag{2.29}$$

where α is a proportionality factor that represents the radiometric system sensitivity.

It is easy to understand that α has to be the largest possible in order microwave radiometry to be successful as a diagnostic method. For a given tumor diameter, the larger α the smaller the tumor over-temperature detected and the deeper the tumor as well. If the temperature of the scanned object is constant Eq.(2.29) yields to the expected result $\frac{\Delta S}{\Delta T} = 1$ i.e., $\alpha = 1$.

In the following chapters we will show that α depends not only on the instrumental sensitivity but also on the antenna characteristics.

Now, it is simpler to understand the main feature of microwave radiometry in the ability to detect subcutaneous and localized over-temperature related to functional features of the tissue such as metabolism and angiogenesis, from a contacting non invasive measurement.

In order to estimate the difference radiometric signal ΔS, temperature and weighting function distributions inside normal and malignant breast have been computed according to the scheme of Fig.2.12 and results are presented in chapter 3.

During a real diagnostic test, since we don't know which is the breast quadrant of the malignancy i.e. we don't know which is the reference signal, we can suppose to take the radiometric data for each of the positions set for the scan and then compare one another.

Chapter 3

Detectability of Tumor by a Radiometric System

3.1 Radiometric Visibility

In this chapter we discuss the detectability of a tumor by a radiometric system which receives thermal emission from a body, i.e., a breast, using definitions and equations in the previous chapters.

For the signal S_B in output to a radiation-balance microwave radiometer we shall use:

$$S_B = \frac{\int\limits_{\Omega} P_d(\underline{r})T(\underline{r})dV}{\int\limits_{\Omega} P_d(\underline{r})dV} \tag{3.1}$$

that has already discussed in chapter 2. S_B is affected by a noise σ_R that depends on integration time τ_R. σ_R decreases as τ_R increases. It depends also on the receiver bandwidth i.e., the larger the bandwidth the smaller σ_R.

Since in most cases the volume sensed by the antenna is mathematically unlimited extending to regions of unpredictable temperature, an approximation of Ω will be introduced, consisting in a volume including a large fraction, e.g. 95%, of the net real power radiated by the antenna. According to this definition, the antenna radiation solid, Ω, generally is a convex set beneath the antenna. The particular shape of Ω depends on tissue, antenna and frequency. Other sources

may contribute a current to the receiver input, such as external independent radiation entering the antenna via the body or through the currents it induces on connecting cables. For the sake of simplicity we shall neglect such spurious contributions.

The presence of a malignancy may result in an over-temperature ΔT as well as in a change ΔP_d of power deposition within Ω, due to a change in permittivity of tumor tissue with reference to normal tissue. In order a thermal anomaly to be detected, the difference ΔS in the radiometric signals between unhealthy and normal breast must be larger than σ_R. We introduce a radiometric visibility as the maximum depth of a tumor that can be detected. The radiometric visibility is a function of lesion size for a given depth. In this chapter we investigate this dependence.

ΔS evaluation needs a preliminary estimate of the breast tumor over - temperature. This has already performed in the previous chapter assuming homogeneous thermal properties of mammalian tissue and that the heat balance is adequately described by the classical bio-heat equation. It has been found that the over-temperature due to a lesion for standard room conditions does not exceed $1-2^{\circ}C$ depending on size and decreases with the distance from the breast surface where a radiation-type boundary condition [80] is imposed.

The weighting function depends on the electrical parameters and shape of a sensed body, as well as on antenna and frequency of operation. In this paper an attempt has been made to obtain results relatively independent of the breast shape which varies with patient and position. To achieve this, a theoretical antenna has been considered, i.e. an aperture in a perfectly conducting plane that radiates onto a half-space with the parameters of a breast. To an acceptable approximation, the radiation solid of this antenna lies in the interior of a sensed breast. ΔS has been evaluated for two sizes of the antenna and compared with σ_R to estimate the radiometric visibility.

3.2 Radiometric Signal Evaluation

In normal operation the thermal emission from the breast is collected by a contacting antenna which is optimized for radiometric application, i.e., it is mechanically and electrically matched to the breast and protected against impinging spurious radiation. However, for the sake of generality, we shall not specify here any particular radiometric antenna letting the size be its only characteristic feature. The electromagnetic model of such an abstract device will be a circular aperture S_a with diameter $2a$ in a perfect conducting plane extending

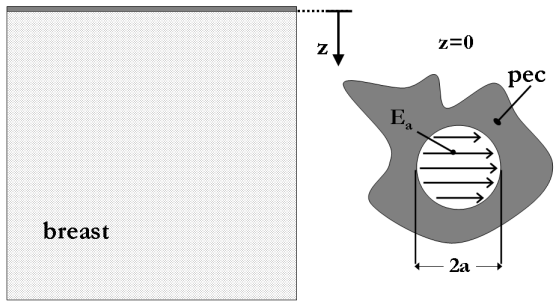

Figure 3.1: Electromagnetic model of a homogeneous breast(left), orthogonal cut perpendicular to the aperture antenna plane. z=0 plane including the circular aperture on a pec plane (right).

to ∞. The field is radiated by a uniform linearly-polarized electric field $\underline{E}_a$ on the aperture. In a Cartesian reference system, the plane has equation $z = 0$, while the halfspace $z > 0$ is filled by gland tissue (Fig.3.1) having parameters $\epsilon = \epsilon_0\epsilon_r$, σ, μ_0, with ϵ_0, μ_0 dielectric constant and permeability of free space, and $\epsilon_r = 10$, $\sigma = 0.2\ S/m$.

Electromagnetic field computations have been performed at frequency $f =$ 2.65GHz. To compute the radiometric signal by Eq.(3.1), power absorption by breast tissue is evaluated when the antenna radiates onto the breast. The electric field $\underline{E}(\underline{r})$, $\underline{r} \in V$, has been obtained within a box V of 7x13x13cm^3 enclosing the hemispherical breast, by a FDTD code using Mur absorbing boundary conditions at the walls.

Contour-level plots of $P_d = \frac{1}{2}\sigma\underline{E}^2$ are shown on two orthogonal principal planes that are respectively perpendicular and parallel (Fig.3.2) to the aperture field $\underline{E}_a$ for a 3cm aperture and $\underline{E}_a = 1$V/m. The 5% contour line circumscribes a convex set beneath an extended aperture S'_a, which is slightly larger than S_a. The quotient between the two areas is $S'_a/S_a = 1.8$ for a 3cm aperture, 1.36 for a 4cm one.

The FDTD computation has been repeated in the presence of a spherical lesion with its center at various depths. The dielectric parameters of malignant

tissue has been taken from [12] as $\epsilon_{rt} = 50$, $\sigma_t = 1.5 S/m$. $\underline{E}$ has a minimum in the lesion, which is due to a larger dielectric constant of a tumor in comparison with that of surrounding tissue. This partially prevents electromagnetic radiation from entering the tumor. Due to higher electrical conductivity, instead, the absorbed power density has a peak inside the lesion.

Results on the radiometric signal evaluation are presented in this chapter considering dielectric properties for breast tissue found in [12].

Recently, the dielectric properties of normal and malignant breast tissues have been experimentally characterized in the microwave frequency range by Lazebnik et al. [13]. Basing on the percentage of adipose tissue content, they classified samples of normal breast into three groups. The dielectric properties we adopted for normal breast are similar to those in the third group in [13] (85-100% adipose tissue content).

Results on a more realistic breast tissue dielectric properties are presented in chapter 4 with a more realistic electromagnetic model of the breast as well. The radiometric signals S_B for normal tissue and S'_B in the presence of a lesion can be obtained from Eq.(3.1) by numerical integration of $P_d T$. However a contacting antenna will locally deform a breast which is flattened to an extension comparable with the antenna size. To take this effect into account, the domain of resolution of the bioheat equation has been changed to a hemisphere H_{cap} deprived of the spherical cap whose basis is the extended antenna aperture S'_a. The height h of the spherical cap is 4.6 mm for a 3cm aperture. We assume that the distance of a lesion from the breast surface is not changed by this flattening. The domain of integration is V taking care, however, to set $T = 0$ when forming the product $P_d T$ at a point $\underline{r} \notin H_{cap}$. We have evaluated the total power P_V deposited in V by the aperture antenna for comparison with the total power, P_H, deposited in H_{cap}. The ratio P_H/P_V can be unitary at the most. The equality $P_H = P_V$ corresponds to the case where no contribution to the radiometric signal has been lost as a consequence of radiation to outside the breast. We found $P_H/P_V = 0.92$ for the normal breast and a 3cm aperture.

3.2.1 Discussion

ΔS as defined in chapter 2, Eq.(2.28), is diagrammed in Fig.3.3 vs. lesion depth for a 3cm and a 4cm aperture, respectively, and a 10mm tumor. The three curves refer to: the complete model (red line); W is used in Eq.(2.28) instead of W', i.e. the lesion does not perturb the electromagnetic field of the healthy breast so that $\Delta S = \int_V W\,(T' - T)\,dV$ (green line); T is used instead of T' (blue line). In the last case the lesion is assumed to not perturb the temperature of

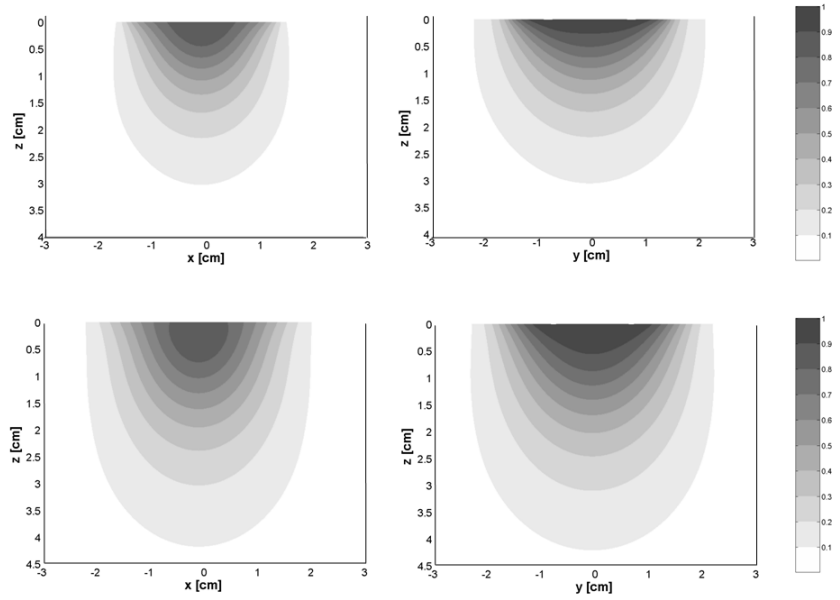

Figure 3.2: Contour-level diagrams of P_d as cross section of Ω_p by the principal plane perpendicular (left) and parallel (right) to the aperture field. Ω_p include the volume where $p\%$ of net real power is deposited. 3cm circular aperture antenna(top), 4cm circular aperture antenna(bottom). P_d is normalized with respect the maximum.

the normal breast so that $\Delta S = \int_V (W' - W)\, T\, dV$. The last diagram shows that the difference signal ΔS is very low if the presence of a tumor does not locally affect the normal breast temperature. In other words and for an ideal radiation-balance radiometer, the difference signal is mainly due to an eventual over-temperature. On the contrary, even if a tumor does not exhibit different dielectric properties from those of the healthy tissue, a difference signal can be appreciated due to over-temperature.

An approximate equation is obtained letting $\int_V (W' - W) T dV = 0$. After substitution into Eq.(2.28) we obtain $\Delta S \simeq \int_V W'(T' - T) dV$, and:

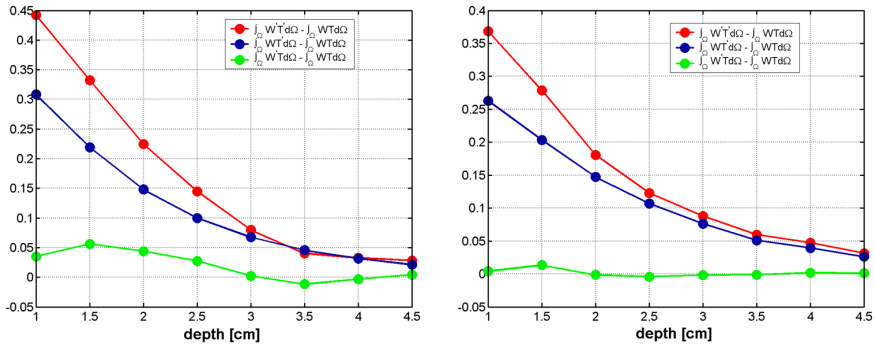

Figure 3.3: Difference radiometric signal (unhealthy-normal) for a 10mm lesion at various depths. 3cm aperture antenna (left), 4cm aperture antenna (right).

$$\Delta S \cong \frac{\int\limits_V P_d^{\prime}(T^{\prime} - T)dV}{\int\limits_V P_d^{\prime} dV} \tag{3.2}$$

A further approximation allows a very simple interpretation to the useful signal. Studying the thermal model we have seen that the over-temperature ΔT is localized in a spot including the tumor core. Denote this spot by ω. If $\overline{\Delta T}$ is an average value within ω, we have for the difference signal:

$$\Delta S \cong \overline{\Delta T}\eta_\omega \tag{3.3}$$

with

$$\eta_\omega = \frac{\int\limits_\omega P_d^{\prime} dV}{\int\limits_V P_d^{\prime} dV}$$

We conclude that the difference signal is approximately proportional to the mean temperature difference between malignant and normal breast where the factor η_ω has the meaning of an efficiency. Indeed η_ω is the power delivered to ω as a fraction of the net power delivered to the breast when the antenna radiates

onto it in active modality. This coefficient is a heating efficiency in microwave hyperthermia where electromagnetic power is focused to heat preferentially a target in respect to surrounding tissue.

The difference signal is finally shown as a function of tumor depth and size for two apertures in Fig.3.4. A tumor is radiometrically visible if the difference signal overcomes the resolution, i.e. $\Delta S \geq \sigma_R$ is the condition for a tumor to be visible. σ_r is some hundredths of degree depending on radiometer and integration time. A reference value can be $\sigma_R = 0.1°\text{C}$, with 1s integration time. We observe from the diagrams that (i) the visibility decreases with tumor depth. In fact both the over-temperature and the weighting function decrease with the distance from the surface; (ii) a small tumor of 6mm is visible in a superficial layer of the breast of thickness 1cm about, while a 10mm tumor is visible in a layer of 2.8cm; (iii) a 3cm aperture is more effective than a 4cm one up to $\cong$ 3cm, because a larger value of η_ω; (iv) a 4cm aperture is more effective for deeper tumors because a larger penetration depth; (v) a lower σ_R improves visibility, e.g., a 6mm lesion is visible up to 2cm, a 10 mm lesion up to 3.5cm for 0.05°C of radiometric resolution.

Fig.3.5 is a concise diagram of tumor radiometric visibility for $\sigma_R = 0.1°\text{C}$ and for 3 and 4cm circular aperture antenna.

It is worthy mentioning, however, that the metabolic generation coefficient in the bio-heat equation is probably underestimated for small tumors, whereas an over estimation of the difference signal may be due to the presence of increased peripheral perfusion. To appreciate the reduction of radiometric visibility as a consequence of reduced thermal visibility, diagrams of ΔS are presented in Fig.3.6. Now a 10mm lesion is radiometrically visible if it is not deeper than 2cm.

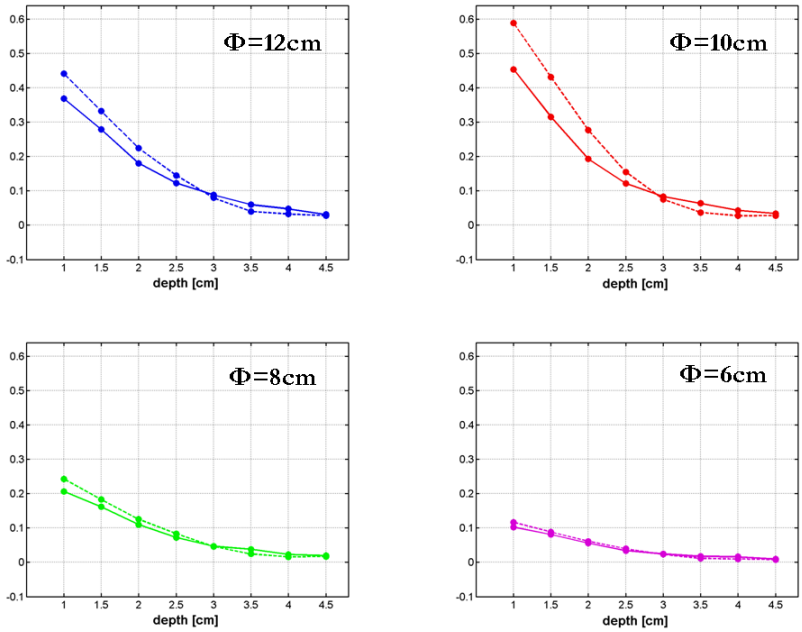

Figure 3.4: Difference radiometric signal vs. tumor depth for an aperture antenna of 3cm (dashed line) and 4cm (continuous line).

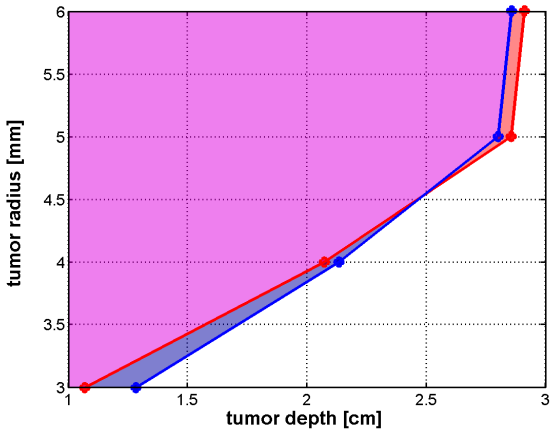

Figure 3.5: Radiometric visibility map. The magenta area includes tumors visible by both a 3cm and 4cm aperture antenna. The blue area includes tumor visible only by a 3cm antenna while the red area includes tumors visible by a 4cm antenna.

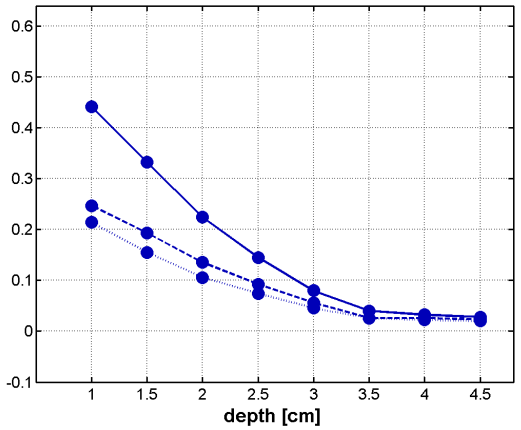

Figure 3.6: Difference signal vs. tumor depth for a 3cm aperture antenna and: uniform perfusion (continuous line), increased perfusion in a 1cm superficial layer (dashed line), increased perfusion in a 2cm layer (dotted line).

Chapter 4

Breast Tissue Compression to Improve Radiometric Visibility

4.1 Imaging of Compressed Breast by Micrwowave Radiometry

In this chapter the breast is intentionally squeezed between the radiometric antenna and the chest wall and the temperature is evaluated for the deformed breast together with the generated radiometric signal.

To be compared with the radiometric resolution, the difference signal between the outputs in the presence of a lesion and in its absence has to be evaluated. To achieve this, a mechanical, thermal and electromagnetic model of the breast has been developed. A finite-element code has been used to solve for the mechanical and thermal problems, while FDTD has been exploited for electromagnetic computations. We show that compressing the breast improves the radiometric visibility depending on tumor depth and deformation [82].

When a contacting sensor is scanned on the breast a pressure is normally exercised. The breast is deformed so that the distance of a lesion from the contacted surface is lowered while its visibility is changed. While breast flattening has been treated as a negligible effect in the modeling by previous authors, in this paper the breast is intentionally squeezed between antenna and thorax and

we estimate the thermal behavior and the corresponding radiometric signal for the deformed breast. Breast compression is routinely performed during compression mammography to an extent that is indicated by regulatory agencies [83].

To evaluate the radiometric signal the mechanical, thermal and electromagnetic properties of the breast must be specified for each tissue component.

In the next section the breast deformation due to a compression exercised normally to the chest wall will be studied, while the thermal and electromagnetic models that are necessary to estimate S will be presented in section 4.1.2 and 4.1.3. The mechanical and thermal problems have been solved in a finite-element frame using the commercial tool COMSOL Multiphysics [84]. The electromagnetic problems have been solved by FDTD using a proprietary code. Preliminary results will be presented showing the increase in visibility that are consequent to breast compression.

4.1.1 Biomechanical Model

The normal breast consists of a tree-like structure of glandular tissue supported by connective tissue, immersed in fat and surrounded by skin. However, to simplify the problem, we model the breast as a homogeneous hemisphere supported by a square box of muscle (as already presented in chapter 2, Fig.2.6). Assuming that the breast is made of an equal amount of fat and glandular tissue, the homogeneous model results from averaged mechanical properties.

To model the breast deformation under compression, a simulation model, which can handle large deformations and nonlinear, nearly incompressible materials, must be implemented.

In literature breast-deformation modeling is receiving attention due to the need of data fusion from X-ray mammography in different views and Magnetic Resonance Imaging in early cancer diagnostics as well as to achieve suitable information for surgery or needle insertion during a biopsy [85], [86], [87], [88], [89]. Biological tissues have been shown to exhibit non-linear stress-strain laws [90], [91] and this is the case for the range of strains involved during mammographic screens. Different material models for breast tissues are proposed in the literature. A review of stress-strain relationships can be found in [86]. The resulting stress for a given strain is largely dependent on the model, while a criterion for model validation can be the plausibility of the achieved deformation in the comparison with experimental outcomes e.g. in [92] the displacement of a set of landmarks positioned on a patient has been measured for increasing net deformation. The exponential models are more accurate than linear and neo-

hookean ones in retrieving large breast deformation. However, as a drawback, they originate non-realistic compression forces [92], [93].

The kinematic problem is to find the coordinates x of the deformed body, given the coordinates X of the undeformed body. The displacement vector and the Green-Lagrange strain tensor are respectively defined as:

$$\underline{U} = \underline{x} - \underline{X} \tag{4.1}$$

$$E_{ij} = \frac{1}{2}(\frac{\partial U_i}{\partial X_j} + \frac{\partial U_j}{\partial X_i} + \frac{\partial U_k}{\partial X_i}\frac{\partial U_k}{\partial X_j}) \tag{4.2}$$

where summation over repeated indices is intended. The deformation gradient tensor $F_{ij} = \frac{\partial x_i}{\partial X_j}$ is introduced. The Second Piola- Kirchoff tensor, T_{mn} , is generally used as stress definition in large deformation problems. T_{mn} is defined as the force acting on the undeformed body measured per unit undeformed area. In an equilibrium deformed state, all forces must balance, and it can be shown that this leads to:

$$\frac{\partial}{\partial X_m}(T_{mn}\frac{\partial x_i}{\partial X_n}) + f_i = 0, (i = 1, 2, 3) \tag{4.3}$$

where f_i is volume external force component per unit volume. To relate stress to strain, a strain energy function $W(E_{ij})$ is assumed to exist. The principle of virtual works allows the equilibrium problem (Eq.4.3) to be reformulated as an energy minimization problem. We have made the assumption that the tissue is isotropic. If a material is isotropic, the strain-energy density function W can be in general expressed as a function of the strain invariants I_1, I_2, I_3 where $I_1 = tr(F_{ij}^T F_{ij})$ and ^{T} is for transposed. $I_3 = J^2$, with J volume ratio. $J = 1$ for a perfectly incompressible material. Practically, tissues have a Poisson ratio that ranges from 0.49 to 0.5. The Poisson ratio for the tissue used in this study is 0.498. We assumed an exponential constitutive law [87]:

$$W = a(e^{b(I_1-3)} - 1) - \frac{p}{2}(I_3 - 1) \tag{4.4}$$

where a and b are average fit parameters between fat and glandular tissue calculated from uniaxial stress-strain experiments using a tissue sample [94], p is the internal pressure that represents a Lagrangian multiplier introduced to impose the constraint $I_3 - 1 = 0$.

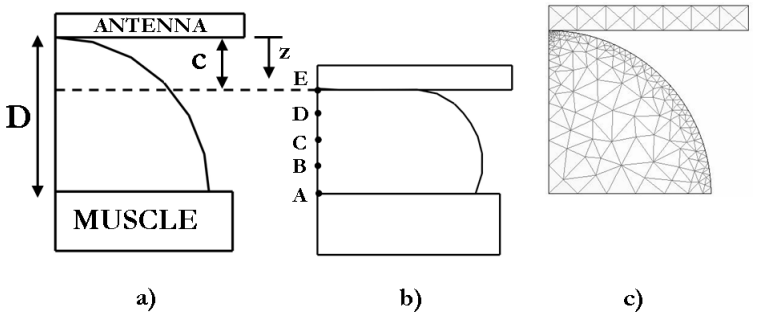

Figure 4.1: Geometry of the undeformed breast a), Geometry of the deformed breast b), Undeformed breast, partition into triangular elements c).

Finally, the mechanical boundary conditions must be specified to obtain the solution. We admit that the radiometric antenna is frontally pressed against the breast, which is squeezed between the planar antenna and the thorax plane, coincident with the pectoral muscle wall. The two planes are parallel. The muscle wall is fixed. Zero displacement on the muscle wall in contact with the breast and zero pressure on the free skin surface are suitable boundary conditions. The antenna itself has been modeled as a compression plate with the mechanical coefficients of aluminum. At the interface between antenna and breast a non-penetration condition holds [87].

Owing to this condition the breast modeling under compression is not a standard elasticity problem. Let D be the distance of the antenna plate from the chest wall. The compression plate is supposed to move in the direction of the z-axis, towards the chest. D equals the hemisphere radius R in the undeformed configuration, when the plane is contacting the breast at a single point (Fig.4.1a).

During compression D is reduced while the plate/breast contact area increases (Fig.4.1b). If the total displacement of the plate is C, then the relative net deformation is $C/R = (R - D)/R$. The following numerical analysis will be performed for a net deformation of 35%, which is between the limit values of mammography (20-50%). In order to model such a large deformation we divided C into N small displacements. Then we solved N linear deformation problems as a sequence of steps. At the end of each step, we know the flattened breast surface in contact with the antenna. However, we don$'$t know "a priori" which

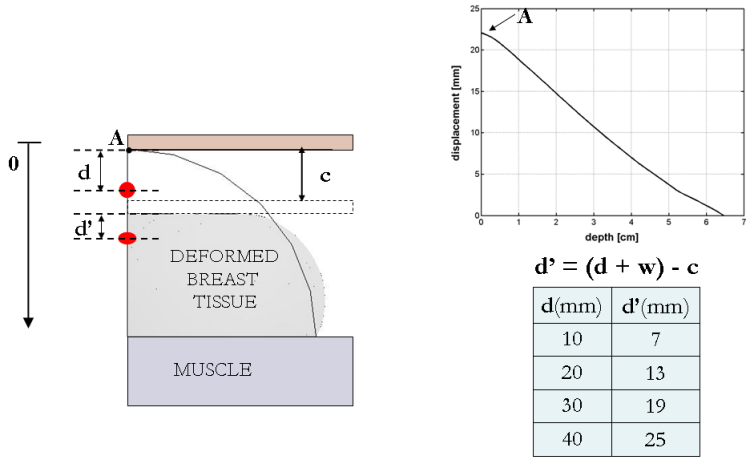

d' = (d + w) - c

d(mm)	d'(mm)
10	7
20	13
30	19
40	25

Figure 4.2: Particle displacement for vs. depth on z-axis.

additional surface the antenna will contact as a consequence of the deformation at the next step. The problem of determining the additional contact surface of a deformable body under compression is known as a contact analysis problem. It has been formulated and solved as an Augmented Lagrangian optimization [95]. Due to axial symmetry a quarter of the structure has been modeled, therefore the further condition of zero displacement normally to the symmetry walls has been introduced. The finite element mesh consists of 15150 tetrahedral elements, 14620 for the breast and 530 for the compression plate. A view of the partition into elements is shown in Fig.4.1c. Mesh density is higher near the initial point of contact between the breast and the antenna while an element size of 2.5mm is specified on the breast external surface. To solve for the non-linear mechanical behavior, after a small displacement increment of the compression plate, the internal pressure is computed together with the displacement at each point.

In mammography breast deformation studies, the relative reduction of a breast diameter is imposed, while the net force between the plates is computed from the resulting stress. The diagram in Fig.4.1b refers to a breast deformation of about 35% for frontal compression.

In Fig.4.2 the displacement is shown versus particle depth in the undeformed

state on a sagittal plane. The displacement is practically linear with depth, with 35% slope. We modeled a tumor as a sphere. The sphere is located on the symmetry axis (z-axis) perpendicular to the chest wall. Tumor-center distance from the antenna contact point in the undeformed state is referred to as tumor depth. For simplicity the mechanical properties of the tumor have been taken coincident with those of the host tissue. After frontal compression the sphere is deformed into an ellipsoid whose axes can be estimated using the diagram in Fig.4.2 for the displacements of the tumor-diameter end-points along the z-axis, while the two other axes are found by tumor volume conservation. If we denote with w the displacement for points along z-axis the tumor depth in the deformed breast d' will be:

$$d' = (d + w) - C \tag{4.5}$$

Tumor depths after compression, evaluated according to Eq.(4.5) are presented in the table of Fig.4.2 for tumor initially at 1cm, 2cm, 3cm and 4cm depth in the reference configuration.

4.1.2 Thermal Model

In previous chapter the contact between antenna and breast was ideally confined to a small area and to a very short time interval, in such a way to neglect temperature variations in the breast due to the soft contact with the antenna. Two limiting cases can be envisaged in the presence of large deformations.

In a first case the antenna is instantaneously compressed against the breast, while the radiometer takes the data in that instant. No heat exchanges are allowed, so that the temperature of a particle at a point x in the compressed state coincides with its temperature at the initial location X in the undeformed state (Fig.4.3c). We shall refer to this temperature as adiabatic temperature.

In a second case, the radiometric data acquisition takes enough time (about 12 minutes as shown in Fig.4.3b) to let the temperature reach the steady state within the deformed breast in the presence of a larger contact surface between antenna and breast (Fig.4.3d). We shall refer to this temperature as steady-state temperature.

We expect that the temperature that is sensed by the antenna during a realistic measurement be between these limiting cases. At the boundary between antenna and breast, Eq.(2.25), (chapter 2) still holds, with a heat transfer coefficient $h_a = 135W/(m^2 \cdot K)$, i.e., ten times the coefficient for the air/breast

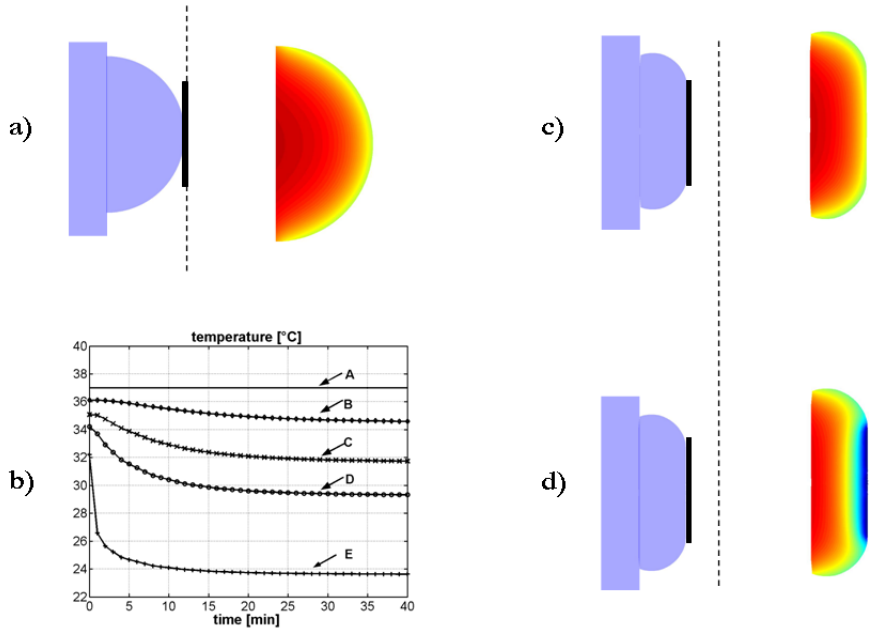

Figure 4.3: Temperature maps on a sagittal plane for undeformed normal breast a), deformed normal breast in the adiabatic case c), deformed normal breast in the steady-state case d). Temperature T vs. time at the points labeled as in Fig.4.1b. The curves start for t=0 from the adiabatic values b).

interface. The antenna is supposed to be kept at a reference temperature T_a, by circulating de-ionized water.

For normal breast: $k = 0.48W/m{\cdot}°C$, q_m=700 W/m^3, ρ_b=1060 Kg/m^3, $c_b = 2600J/Kg{\cdot}°C$, $w_b = 0.00054s^{-1}$. For muscle: $k = 0.48W/m{\cdot}°C$, $q_m = 700W/m^3$, $w_b = 0.0008s^{-1}$. $Ta = 20°C$, $T_A = 20°C$, $T_b = 37°C$.

For tumor: $k_t = 0.511W/m{\cdot}°C$, $q_{mt} = 65400W/m^3$, $w_{tb} = 0.01s^{-1}$ [76].

Diagrams of ΔT vs. lesion depth are shown in Fig.4.4 along a line through the lesion center, for a 10mm tumor centered at 1cm, 2cm, 3cm and 4cm from the surface, in the adiabatic and steady-state cases. The tumor depth is the tumor-center distance from the surface before compression.

From the diagrams in Fig.4.3 we observe that the breast peripheral temper-

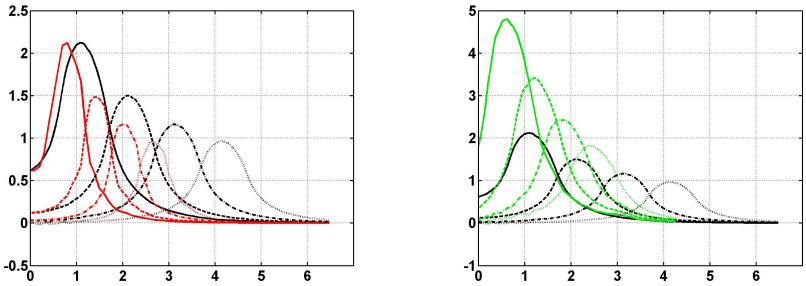

Figure 4.4: Temperature difference (unhealthy-healthy) ΔT for a 10mm lesion and compressed breast vs. lesion depth in cm. Steady-state (green line) and adiabatic (red line) temperature. Black line in both figure a) and b) is temperature difference for undeformed breast.

ature is lower for steady-state because of the more effective superficial cooling forced by the contacting antenna. Therefore the tumor steady-state over temperature ΔT is higher than the adiabatic one as shown in Fig.4.4.

4.1.3 Electromagnetic Model

As in section 3.2 the electromagnetic model consists of a circular aperture of diameter 2a, center at $z = 0$, in an infinite conducting plane. Motivations of this particular electromagnetic model have been discussed in the previous chapter.

We assume the halfspace in front of the aperture is filled by breast tissue. Accounting for the heterogeneity of breast tissue is a difficult task since the adipose tissue is inseparably intermixed with fibroglandular parenchyma (except in the subcutaneous region) [96], [97].

For simplicity we assume a homogeneous medium with dielectric properties as in [98].

The field is radiated by a uniform linearly polarized electric field E_a on the aperture. The center-band frequency is 2.65 GHz, which is close to widely used frequencies in medical application of microwave radiometry [46], [99], [100], [53], [101].

Electromagnetic field computations have been performed by a proprietary

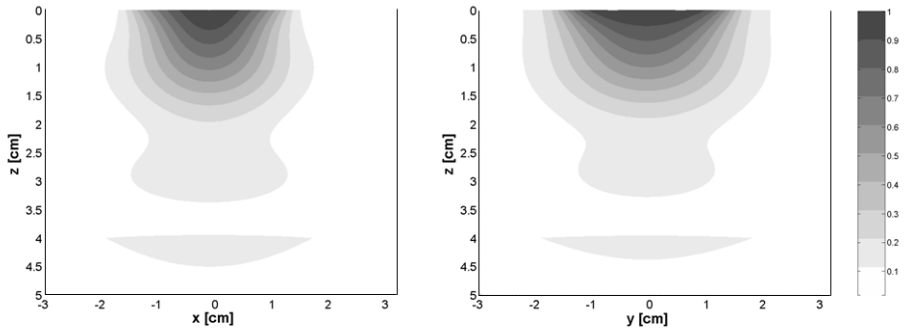

Figure 4.5: Contour-level diagrams of P_d on the principal plane perpendicular(left) and parallel(right) to the aperture field respectively.

FDTD code using Mur absorbing boundary conditions at the walls. The FDTD computation has been repeated in the presence of the spherical lesion with its center at various depths. Contour-level plots of P_d are shown on two orthogonal principal planes in Fig.4.5.

For normal breast: $\epsilon_{rb} = 10$, $\sigma_b = 0.2S/m$; for muscle: $\epsilon_{rm} = 50$, $\sigma_m = 1.5S/m$.

4.1.4 Radiometric Model

The radiometric signal has been computed by equation after temperature and power P_d delivered to tissue have been determined within both normal and unhealthy breast.

Diagrams of ΔS are shown in Fig.4.6a as a function of tumor depth and refer to non-compressed breast.

The diagrams in Fig.4.6b refer to the compressed breast and to the adiabatic (bold line) and steady-state (gray line) temperatures. A realistic curve for ΔS lies between these diagrams.

As we have already shown before this chapter a tumor is radiometrically visible if the difference signal overcomes the resolution, i.e. $\Delta S \geq \delta S$ is the condition for a tumor to be visible.

The visibility of a 10mm tumor increases passing from about 2.5cm (Fig.4.6a) in the undeformed breast to a value between 30mm and 38mm (Fig.4.6b) in the

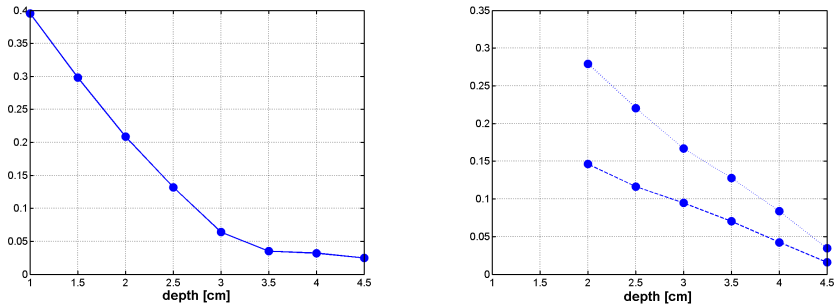

a) b)

Figure 4.6: Difference radiometric signal (unhealthy-normal) of a 10mm lesion vs. depth and a 3cm aperture antenna for non compressed breast a), for compressed breast: adiabatic temperature (dashed line), steady-state temperature (dotted line) b) .

deformed breast and 35% net deformation if the dielectric properties are chosen as in [98].

Breast compression has a number of advantages for a diagnostic application such as microwave radiometry. Compressing the breast with the patient in a supine position, maximizes the amount of breast tissue within the compression device and moves the breast lesion away from the chest wall as we have shown in this chapter. Compressing the breast to a flat surface with an acrylic plastic material improves the transfer of microwave energy from the applicators to the breast tissue i.e., in reciprocity, the receiving of microwave energy improves. Besides, cooling the breast compression plates and skin with air during radiometric treatments helps emphasize the tumor over-temperature. Compression immobilizes the breast tissue such that any potential patient motion complications are eliminated.

On the other hand use of breast compression reduces blood flow, which improves the ability to rapidly heat tissue when a thermotherapy treatment is considered but for the compression level considered in this chapter and supposing an acquisition time of 5 minutes at most, breast blood supply alterations can be neglected.

4.2 Results for a Realistic Model of the Breast

An improved model of the breast, which includes a portion of chest, a skin layer and both fat and fibroglandular tissues has been considered in order to evaluate the radiometric signal with a more realistic set of dielectric parameters.

Fig.4.7 shows the electromagnetic model on a cross-section orthogonal to the aperture plane.

Electromagnetic computations have been repeated for the electromagnetic model of Fig.4.7. The difference signal is shown on Fig.4.8a for a 10mm tumor and a 3cm circular aperture antenna vs. lesion depth in comparison with the difference signal evaluated with the homogeneous electromagnetic model for the undeformed breast.

We notice from the diagrams that the difference signal is understimated when a homogeneous electromagnetic model is considered. This is due to the shift of the weighting function as shown in Fig.4.8b.

The weighting function related to a homogeneous fibroglandular tissue has been included in Fig.4.8b for comparison.

The visibility of a 10mm tumor estimated with a more realistic model increases with respect to the homogeneous one. It grows up to about 3cm.

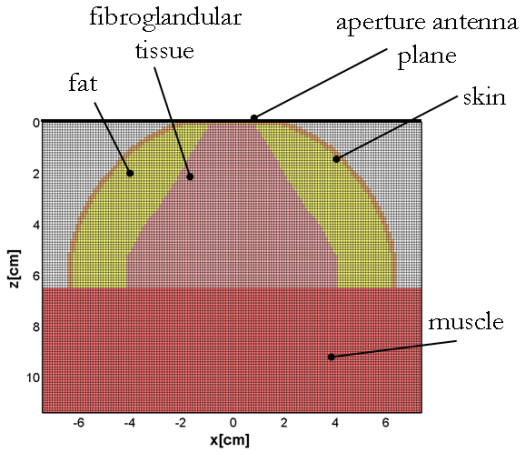

tissue	ε_r	σ[S/m]
skin	37	1.4
fibroglandular tissue	39	1.18
fat	10	0.2
muscle	52	2

Figure 4.7: Realistic multilayer model of the breast on a cross section (left); dielectric parameters of tissues (right) .

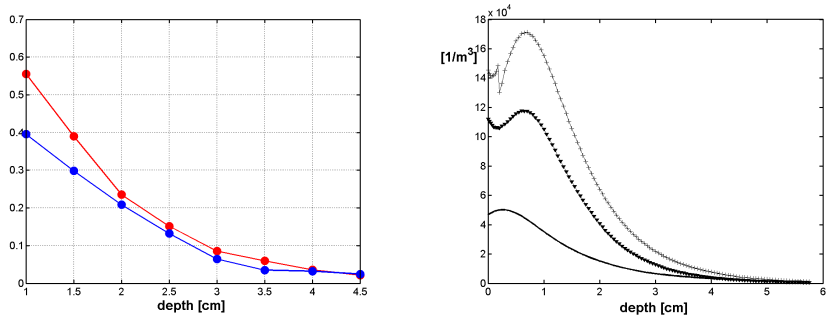

a) b)

Figure 4.8: Difference radiometric signal for a 10mm tumor and a 3cm circular aperture antenna. Homogeneous electromagnetic model (blue line), realistic multilayer model (red line) a) . Weighting function along an axis orthogonal to the aperture plane passing from the circular aperture center. Homogeneous fatty breast (continuous line); homogeneous fibroglandular tissue (line with triangles); multilayer model (line with plus sign) b).

Similar results are shown for the deformed breast in Fig.4.9.

The visibility of a 10mm tumor increases passing from about 3cm (Fig.4.8a, red line) in the undeformed breast to a value between 32mm and 45mm in the deformed breast and 35% net deformation.

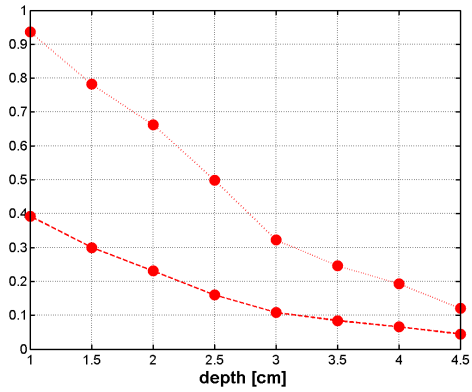

Figure 4.9: Difference radiometric signal (unhealthy-normal) of a 10mm lesion vs. depth and a 3cm aperture antenna for compressed breast: adiabatic temperature (dashed line), steady-state temperature (dotted line).

Chapter 5

Theorical and Experimental Characterization of the Radiometric Antenna

5.1 System error in microwave radiometry

An ideal antenna and an ideal radiation balance radiometer have been considered so far. The radiometric equation for an ideal radiation balance radiometer has been presented in chapter 2.

The residual error in the radiometric temperature estimation due to a non-ideal radiation-balance radiometer will be estimated in this chapter. A schematic diagram of the output of a radiometric measurement both for an ideal and a real radiation balance radiometer is presented in Fig.5.1.

When a non-ideal radiometer is considered the measurement is affected by a system error depending on both the instrumentation and antenna. The radiometric temperature can be defined as:

$$T_B = T_{av} \pm \rho T_\epsilon \tag{5.1}$$

for a non-ideal radiation balance radiometer. T_ϵ is residual temperature defined as:

$$T_\epsilon = T_{REC} - T_{av} \tag{5.2}$$

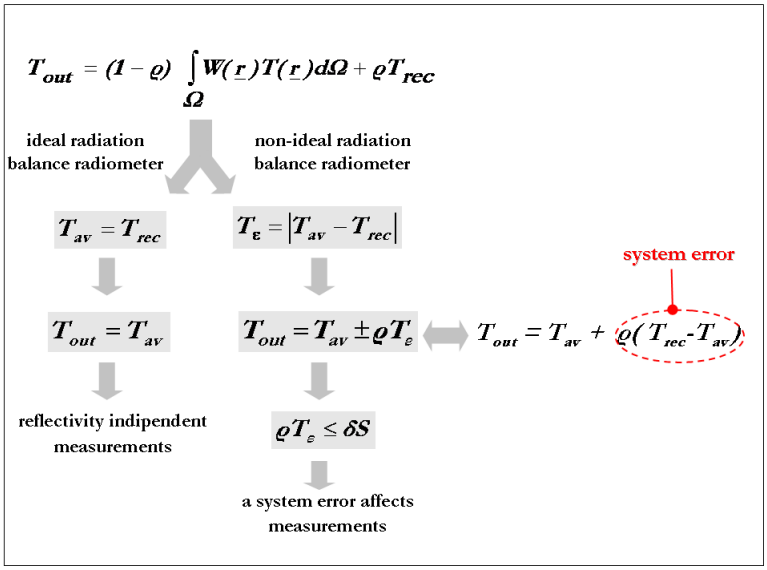

Figure 5.1: Schematic diagram of the radiometric output .

where T_{REC} and T_{av} are receiver temperature and available temperature respectively, as introduced in section 2.1.

The residual temperature depends on the radiometer electronics and it is not so simple to estimate it because a realistic model of the receiver unit of the radiometer that takes into account internal dissipations and the non-ideal behaviour of the electronic components is difficult to derive with good accuracy.

By estimating the antenna reflectivity through a preliminary small-scale experimental study of two antennas on volunteers, we derive a requirement on the residual temperature i.e., we require it to be smaller than the $\delta S/\rho$ ratio as shown in Fig.5.1.

5.2 Thermometric Antenna Requirements

To date, the microstrip antenna has been the most commonly used transceiving element for non invasive monitoring applications such as microwave radiometry

due to its lightweight and conformable structure which allows improved coupling to contoured surfaces, small size, matching capabilities, ease of construction and handling and very low cost [102], [103].

First of all the ability to receive EM-energy from a lossy dielectric load is strongly related to antenna input impedance. Good matching capabilities is the first requirement for an antenna to be used in radiometric application. Ideally a radiation balance radiometer is able to compensate any antenna-tissue mismatch. Since the error in the radiometric temperature estimation depends on the antenna reflectivity for a given T_ϵ as shown in the previous section, it is reasonable to think that an antenna that shows excellent coupling to the medium, insensitivity to differences in tissue properties and positions is desirable.

Antenna size should be chosen as a tradeoff between thermometric spatial resolution and penetration depth. Antennas with a large effective aperture area have a larger depth of measurement sensitivity compared to more omnidirectionally (small) radiating antennas. In practice the effective depth of sensing depends on aperture size, geometric construction, frequency and dielectric properties of the medium. An efficient receiving antenna over a wide frequency band has also more chances to have a good return loss in the frequency band of the microwave receiver.

On the other hand, an antenna can only sense regions or detect objects of size comparable to its dimension (also a function of depth). Detectability is inversely proportional to the antenna's own size although improved recognition to some extent can be obtained by overlapping antenna apertures or correlation techniques. We will not discuss these techniques in this work.

Another important requirement for an antenna to be used in radiometry is to yield the best heating efficiency (see section 3.2) in the boresight direction to receive thermal radiation only from tissue directly below the sensing antenna and not from tissue which may be heated by adiacent transmitting antennas. Moreover the greater the heating efficiency for a given tumor depth, the greater the radiometric signal due to the tumor itself i.e., a good heating efficiency makes the antenna more sensitive to weak thermal noise levels and hence increases the sensing depth of thermal noise signals.

A radiometric antenna should have also the lower radiation efficiency possible in order to prevent spurious radiation coming from outside to enter the receiver.

5.3 Resonant Mode Microstrip Patch Antennas Models

Two patch antennas with simple geometries i.e., with few geometric degrees of freedom have been designed. The two antennas have been designed to be matched with a multilayer model of the breast. We have considered resonant mode antennas working at the central frequency of the radiometer band.

A full three-dimensional model (3-D) finite difference time domain (FDTD) method is applied to analyze finite ground-plane backed circular and rectangular patch antennas radiating into a lossy medium with the dielectric properties of breast tissue.

A multilayer model of the breast made up of 2mm of skin, 2cm of fat and 5cm of fibroglandular tissue has been considered (see Fig.5.2). The dielectric parameters of the layers have been already presented in chapter 5.

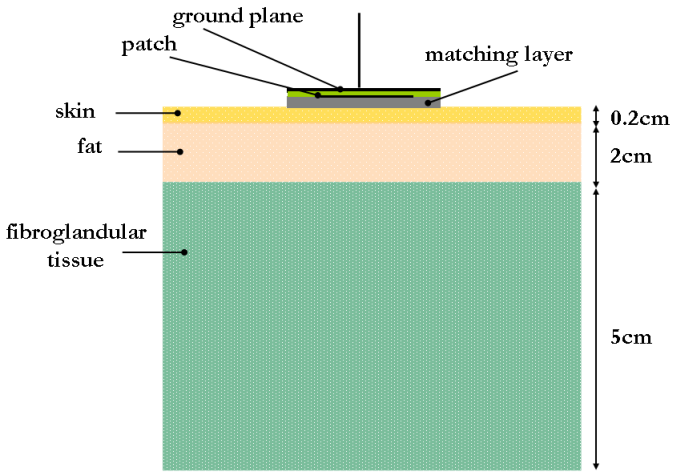

Figure 5.2: Multilayer model of the breast on a cross section .

In the next two sections the performance of these antennas are presented over a 2-3GHz frequency span.

5.3.1 Circular Patch Antenna

The geometry of the circular patch is shown in Fig 5.3 together with a picture of a prototype[1]. A patch size between 3 and 4cm has been chosen as a tradeoff size between penetration depth and spatial resolution. The geometric parameters of the patch and the dielectric constant for the substrate and the matching layer are listed in table 5.1.

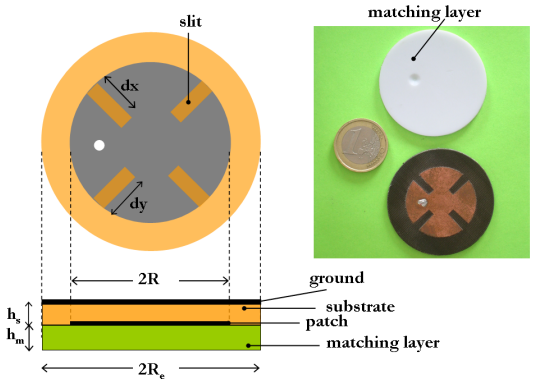

Figure 5.3: Geometry of the circular patch antenna (left) and prototype (right).

dx	dy	R	R_e	h_s	h_m	ϵ_s	ϵ_m
$9.8mm$	$9.8mm$	$1.5cm$	$2.3cm$	$1.5mm$	$2mm$	2.33	2.1

Table 5.1: Geometric parameters for the circular patch antenna and dielectric constants.

Four perturbation slits (of the inset type) on the contour of a circular patch have been introduced in order to make the antenna resonant at 2.65GHz with a patch diameter of 3cm.

[1]Prototypes have been realized by Fabrizio Mancini at DIEI, University of L'Aquila, Monteluco di Roio, 67100-L'Aquila.

Figure 5.4: Tuning patch.

A pair of diametrically opposed slits segments splits the dominant mode into two near-degenerate modes. One of these has a resonant frequency that is lower while the other orthogonal mode resonates at a higher frequency as compared to that of the unperturbed patch. The lower resonant frequency can be conveniently controlled by varying the slit length.

Miniaturized resonant patch antennas possess a very narrow impedance bandwidth. Consequently, in light of material and fabrication tolerances, their design for operation at a precise frequency is a very difficult task, and some form of tuning become necessary. Several methods of tuning resonant patch antennas exist. They consist of use trim tabs, short circuiting posts, reactive load and methods to vary the effective permittivity of the substrate, for example by varying the spacing between the patch and the ground plane.

Generally, a four-slit geometry aims at obtaining circularly polarized radiation by making dx different from dy. When dx=dy the patch is linearly polarized along the line passing through the center and the excitation point (see Fig.5.3).

The resonant frequency decreases as d increases. This means that this geometry can be made about half the size of a circular patch. The geometry corresponding to d/R =leading to a 30% size reduction was realized. The bandwidth decreases as d increases. While the change in directivity is not very significant, it can be seen that the decrease in gain can be dramatic when the slit d is large. These results suggest that a large degree of miniaturization leads to poor performances. The reason is that shape modification introduces "out-of-phase" radiating edges leading to higher dissipation in the presence of losses.

The variation in the resonance frequency with d suggests a simple mean for tuning. The slit region introduces a capacitive loading whose value can be decreased using a variable short circuit. This can be simply realized by stack-

ing another patch of a special shape on the top of the geometry of Fig.5.6. If the capacitance can be short circuited by a planar structure, at a distance slightly above the patch level, electrical contact can be avoided and the resonant frequency become less sensitive to variations in d. By stacking the tuning structure of Fig.5.4, a controllable offset between dx and dy is given and will lead to circularly polarized operation [104].

Although theoretically a tuning range of 2 : 1 is feasible, variation in other antenna parameters limits the useful range to about 15-20%.

The excitation is by a coaxial connector passing through the substrate. The input resistance value decreases as the feed point approaches the center.

The matching layer has the minimum thickness for antenna-tissue coupling. The patch was printed at the center of a circular ground plane with a radius of 2.3cm.

Simulated input impedance and return loss over the frequency range from 2 to 3GHz are shown in Fig.5.5. Computations have been performed using a FDTD code.

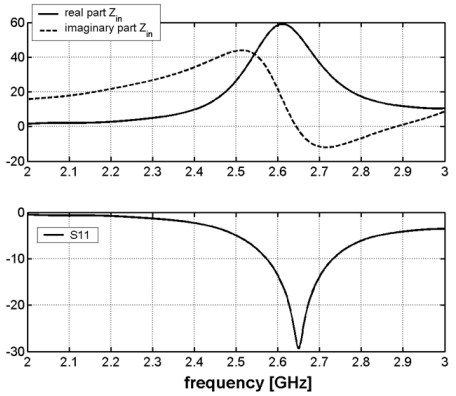

f_o	$\lvert S_{11}\rvert$	$Re[Z_{in}]$	$Im[Z_{in}]$	B%
2.65GHz	-28dB	52Ω	-1.0 Ω	5%

Figure 5.5: Real part, imaginary part and return loss of the input impedance of the circular patch antenna.

5.3.2 Rectangular Patch Antenna

A $\lambda/4$ rectangular patch with a short circuit along one edge has been designed (Fig.5.6). Since the short circuit edge represents a null electric field edge, the short circuit doesn't have effect of the antenna characteristics and it is useful to miniaturized the patch [105].

The patch geometric parameters and the relative permittivity for the substrate and the matching layer are listed in table 5.2.

A parasitic patch element adjacent to the driven patch antenna improves the coupling with the tissues. The available antenna bandwidth also improves by adding a stub element by capacitive coupling with the driven patch.

The bandwidth for this antenna is approximately triple with respect to the circular patch.

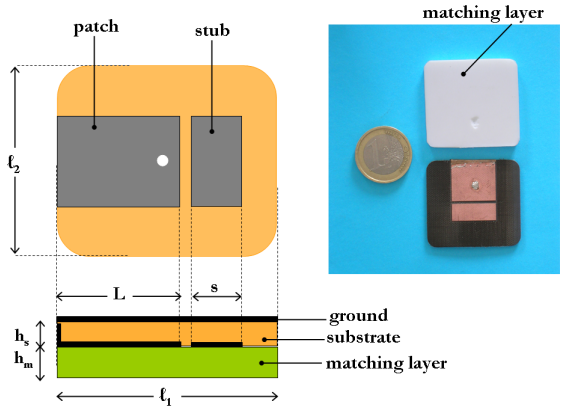

Figure 5.6: Geometry of the rectangular patch antenna (left) and prototype (right).

L	s	ℓ_1	ℓ_2	h_s	h_m	ϵ_s	ϵ_m
$16.5mm$	$7.5cm$	$3.4cm$	$3.8cm$	$1.5mm$	$2mm$	2.33	2.1

Table 5.2: Geometric parameters for the circular patch antenna and dielectric constants.

The corners of the antenna have been smoothed off in order to be more

conformable to the patient.

The antenna excitation is by a coaxial center conductor passing through the substrate. The input resistance value decreases as the feed point approaches the center. The patch is linearly polarized along the axis passing through the and the excitation point.

The matching layer thickness is the minimum thickness that ensures the antenna-tissue coupling as well as for the circular patch.

The patch was printed on a rectangular $\ell_1 \times \ell_2$ ground plane.

Simulated input impedance and return loss over the frequency range from 2 to 3GHz are shown in Fig.5.5.

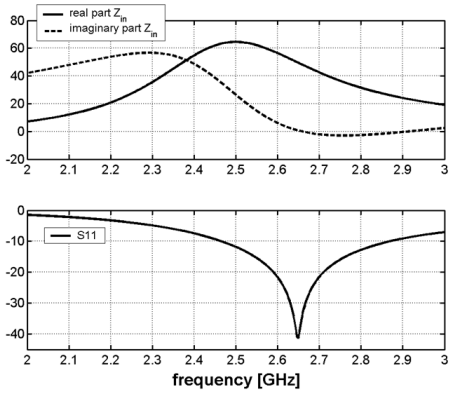

f_o	$\lvert S_{11} \rvert$	$Re[Z_{in}]$	$Im[Z_{in}]$	B%
2.65GHz	-40dB	49Ω	-0.6 Ω	16%

Figure 5.7: Real part, imaginary part and return loss of the input impedance of the rectangular patch antenna.

5.3.3 Measurements

The two antennas have been measured on 40 volunteers splitted into two groups aged 20-40 and 40-60 respectively. 10 measurements for each volunteer, 5 measurements for each side of the breast according to the scheme in Fig.5.8.

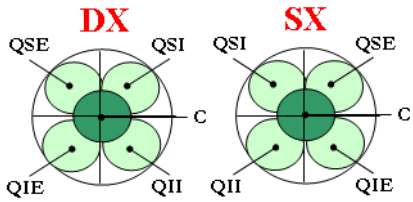

Figure 5.8: Breast quadrants. QSE and QSI are superior quadrants, external and internal respectively. QIE and QII are inferior quadrants, external and internal respectively.

Both the antennas have been equipped with a simple system to control the contacting pressure (Fig.5.9) [2]. A PVC cylinder squeezes a spring sliding onto three brass axes.

On the right side of Fig.5.9 the measured return loss is diagrammed for four different pressure level increasing from p_1 to p_4. It is interesting to notice from the diagram that the antenna reflectivity depends on the contacting pressure. An increase of 2Newton in the contacting force produces a reflectivity decrease of about 50% at frequencies close to the resonance.

5.3.4 Results

Input impedance and return loss have been measured over the frequency range from 2 to 3GHz. Fig.5.10a and Fig.5.10b show the measurements for the groups of volunteers aged 20-40 and 40-60, respectively. Table 5.3 summarizes mean and standard deviation of the measured return loss for the two groups of volunteers and for each side of the breast at 2.6GHz, showing a relatively low dispersion of the measured data. Similar results are presented for the rectangular patch antenna in Fig.5.11a, Fig.5.11b and Table 5.4. In Fig.5.10 and Fig5.11

[2]The pressure control system has been assembled in a collaboration with prof. E. Verona, CNR, Acoustic Institute "O.M. Corbino", Rome, Italy.

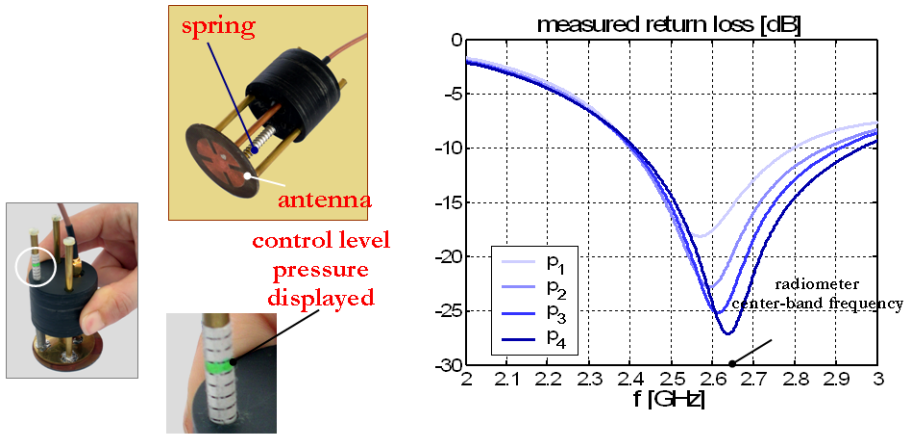

Figure 5.9: Control pressure system with a reference pressure level displayed (left). Measured return loss for 4 different pressure level (right), $p_1 < p_2 < p_3 < p_4$.

the results of the measurements are presented as average (bold line) and $\pm 2\sigma$ dispersion (gray area), with σ standard deviation. They show a relatively low dispersion of the antenna matching properties over the examined population. There aren't significant differences between right and left size of the breast and the standard deviation doesn't depend on the group nor on the antenna.

Diagrams of the best matching frequency found for each of the five quadrants of the breast are shown in Fig.5.13a and Fig.5.13b for the circular patch and in Fig.5.16a and Fig.5.16b for the rectangular patch antenna. Dark-green dots are samples (volunteers) while light-green dots represent the mean frequency evaluated at each quadrant. The best matching frequency for a quadrant is very similar to that of the corresponding quadrant on the controlateral breast for both the two antennas and groups of volunteers, due to anatomical simmetry of the mammary glands.

The best matching frequency ranges between 2.6 and 2.7 GHz (except for the central quadrant) depending on the position, for both the two antennas, groups of volunteers and side of the breast.

The dispersion in the best matching frequency of the circular slitted antenna with respect to the radiometer center-band frequency is lower for volunteers

group aged 40-60 with most fatty breasts. Differences are not significant for the rectangular patch due to its wider bandwidth.

From the diagrams of Fig.5.14 and Fig.5.17 we notice that the measured return loss is -8dB (-10dB) in the worst case for the circular (rectangular) patch antenna at the radiometer frequency. An average return loss of -14dB (-17dB) has been estimated for the circular (rectangular) patch antenna.

A power reflectivity of about 0.17 and 0.10 (worst case) at the radiometer frequency has been estimated for circular and rectangular patch, respectively from table 5.3 and 5.4.

It can be improved by developing an antenna with a wider bandwidth.

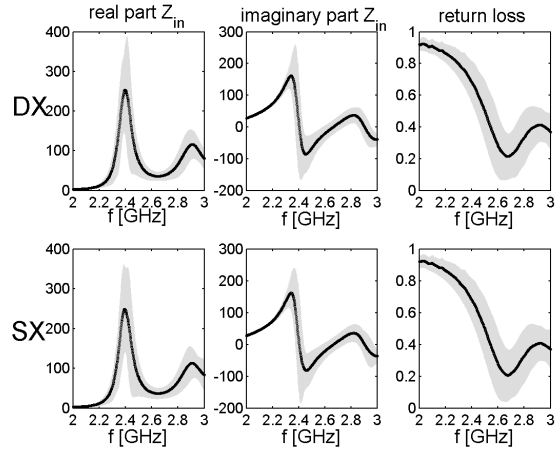

a)

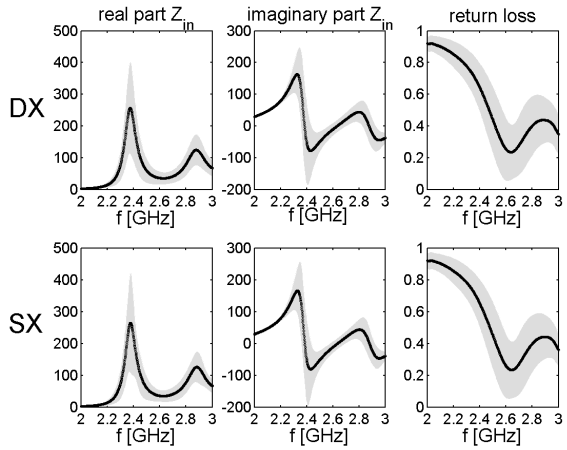

b)

Figure 5.10: Measured input impedance and return loss of the circular patch antenna. Bold line is the mean over all the measurements (10 for each volunteers x 20 volunteers per group), gray area is $|\Gamma|_{mean} - 2\sigma \leq |\Gamma| \leq |\Gamma|_{mean} + 2\sigma$. σ: standard deviation. Group aged 20-40 a); 40-60 b).

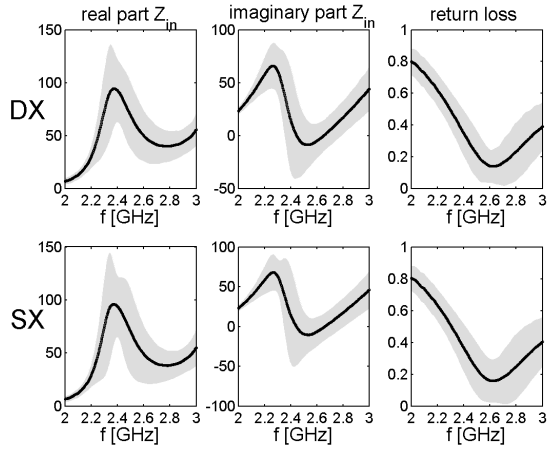

a)

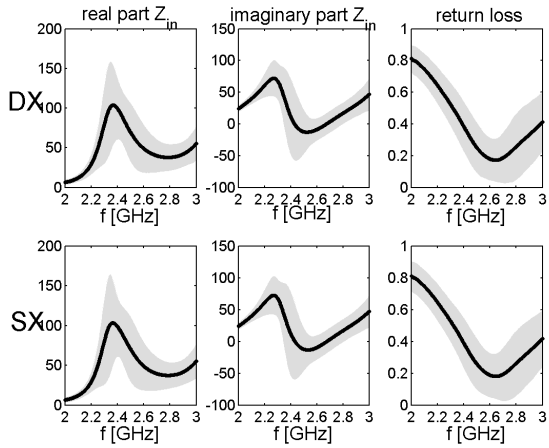

b)

Figure 5.11: Measured input impedance and return loss of the rectangular patch antenna. Bold line is the mean over all the measurements (10 for each volunteers x 20 volunteers per group), gray area is $|\Gamma|_{mean} - 2\sigma \leq |\Gamma| \leq |\Gamma|_{mean} + 2\sigma$. σ: standard deviation. Group aged 20-40 a); 40-60 b).

$\|\Gamma\| \pm 2\sigma$@2.6GHz			
group aged 20-40		group aged 40-60	
DX	SX	DX	SX
$0.22 \pm 2(0.08)$	$0.22 \pm 2(0.09)$	$0.23 \pm 2(0.08)$	$0.23 \pm 2(0.08)$

Table 5.3: Mean and standard deviation of the measured return loss at 2.6GHz for the circular patch antenna.

$\|\Gamma\| \pm 2\sigma$@2.6GHz			
group aged 20-40		group aged 40-60	
DX	SX	DX	SX
$0.14 \pm 2(0.06)$	$0.16 \pm 2(0.07)$	$0.17 \pm 2(0.07)$	$0.18 \pm 2(0.07)$

Table 5.4: Mean and standard deviation of the measured return loss at 2.6GHz for the rectangular patch antenna.

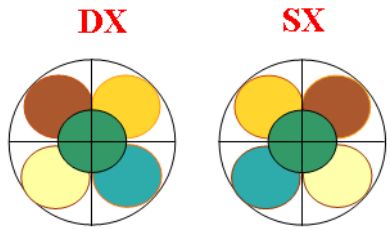

Figure 5.12: Breast quadrants. A quadrant in the right side is represented with the same color as the controlateral quadrant in the left side.

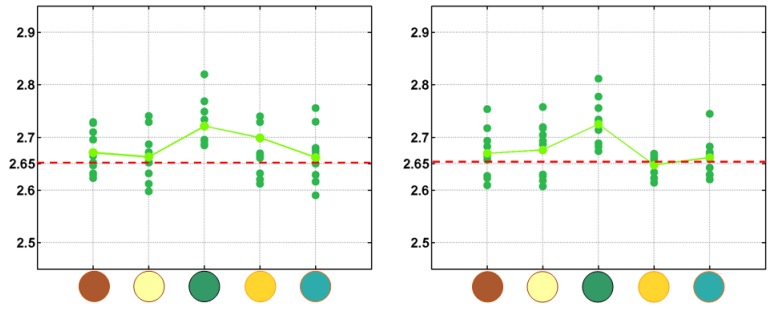

a)

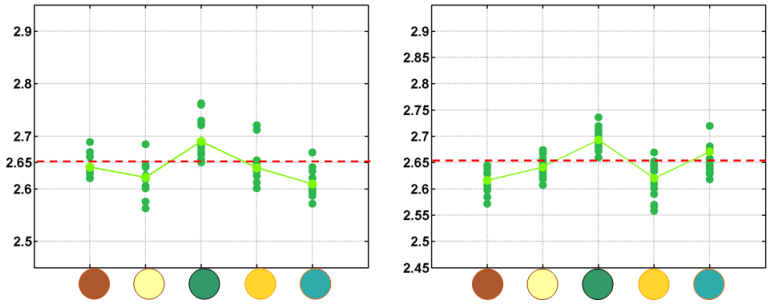

b)

Figure 5.13: Best matching frequency in GHz for each quadrant according to the scheme of Fig.5.15. Dark-green dots are samples. Light-green is mean. Group aged 20-40 a) and 40-60 b) and circular patch antenna.

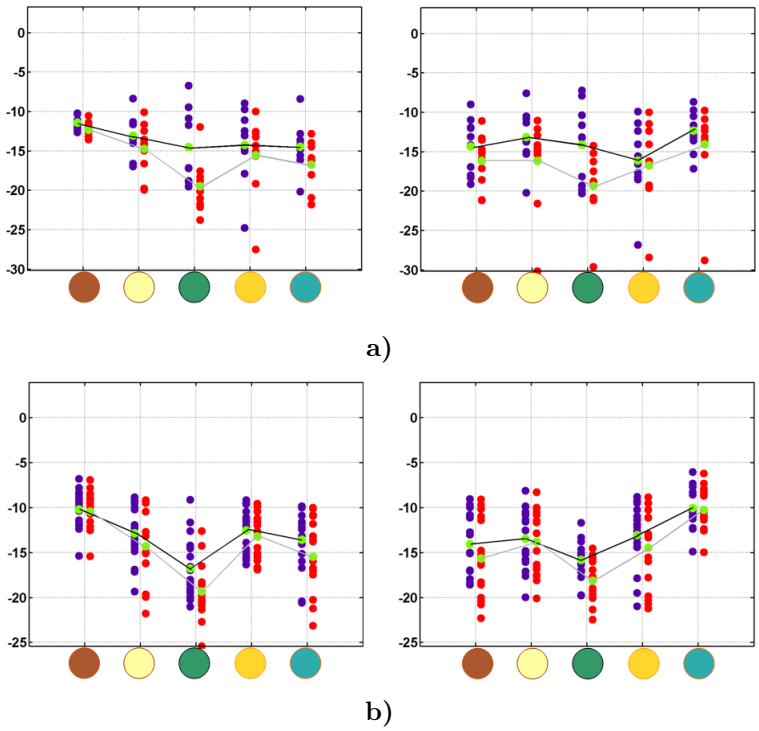

Figure 5.14: Measured return loss at the best matching frequency (red dots) and at 2.65GHz (blue dots) for each quadrant according to the scheme of Fig.5.15. Blue and red dots are samples. Light-green is mean. Group aged 20-40 a) and 40-60 b) and circular patch antenna.

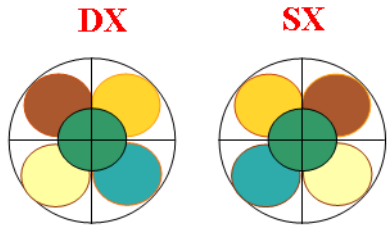

Figure 5.15: Breast quadrants. A quadrant in the right side is represented with the same color as the controlateral quadrant in the left side.

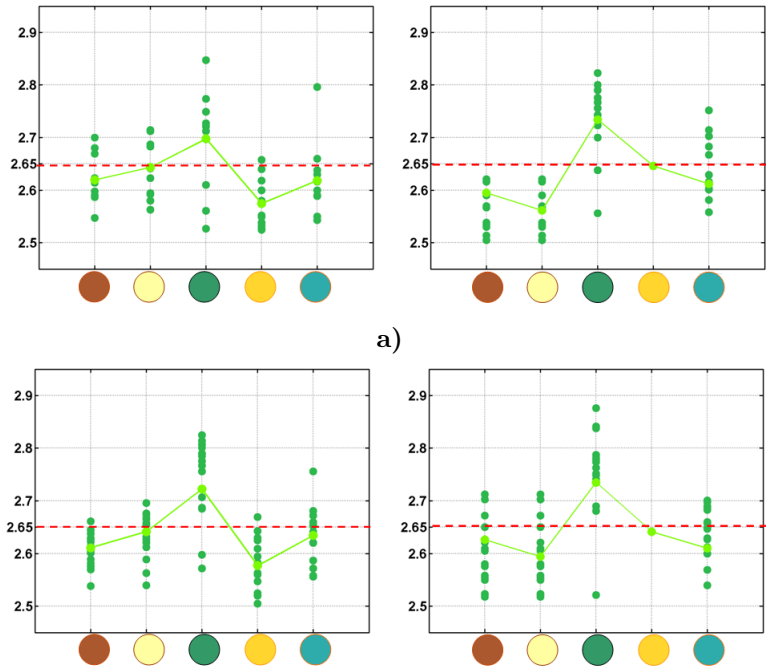

Figure 5.16: Best matching frequency in GHz for each quadrant according to the scheme of Fig.5.15. Dark-green dots are samples. Light-green is mean. Group aged 20-40 a) and 40-60 b) and rectangular patch antenna.

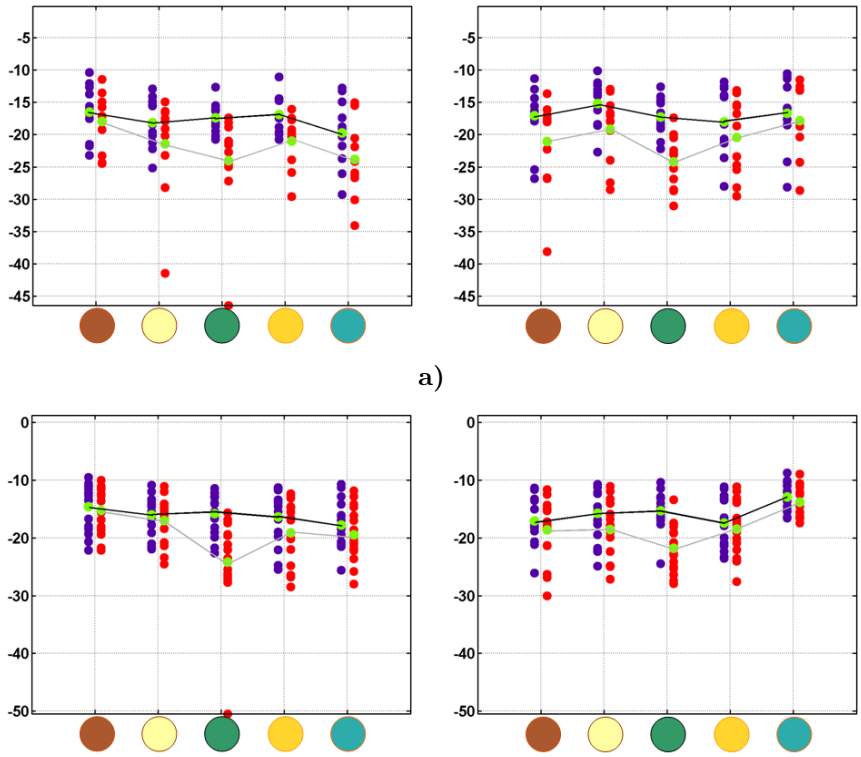

Figure 5.17: Measured return loss at the best matching frequency (red dots) and at 2.65GHz (blue dots) for each quadrant according to the scheme of Fig.5.15. Blue and red dots are samples. Light-green is mean. Group aged 20-40 a) and 40-60 b) and rectangular patch antenna.

Chapter 6

Microwave radiation balance radiometer characterization

6.1 The "Tor Vergata" Radiometer

A two-channel radiation-balance microwave radiometer has been designed in a collaboration with Prof. P. Tognolatti of the University of L'Aquila and it has been assembled in 2003 by Sirio S.r.l. In view of diagnostic application, a sensitivity better than 0.1°C was specified for 1s integration time. Immunity to reflectivity changes in the range between 0 and 0.25 was also specified. The size of the microwave unit has been kept small in order to allow its positioning close to the antenna and the sensed body (Fig.6.1). The radiometer has some interesting features. We quote: i) the use of high performance PIN switches, which show low insertion losses and high insulation due to a resonant scheme; ii) miniaturized front-end which employs MMIC and microwires on bare chips; iii) use of COTS devices in order to have a low cost; iv) radiometer operation and data acquisition supervised by a micro-controller, in order to have flexibility and capability of adopting further measurement procedures.

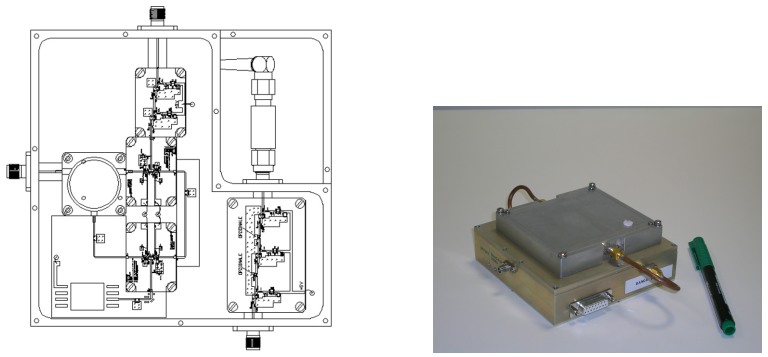

a) b)

Figure 6.1: Radiometer high band frequency microwave unit. Electronic circuit a). Prototype b).

6.2 Preliminary Reflectivity Independent Measurements

In this chapter measurements on the high frequency band channel are presented.

First measurements have been carried out in order to characterize the radiometer ability to detect temperature steps of a homogeneous phantom in reflectivity independent measurements.

Fig.6.2 shows the experimental setup of a radiometric acquisition with a matched load in a thermostated water bath.

For such measurements the problem of spurious external radiation lowering the signal-to-noise ratio can be neglected because the matched load is made up of a shielded cable that ends with a 50Ohm-load fully immersed in a thermostated water bath.

The radiometric data are shown in Fig.6.3a after a calibration that sets the radiometric offset equal to the bath temperature. Three bath temperature steps of 1°C, 0.5°C and 0.3°C respectively are shown in the diagram. All these steps are well detected by the instrument.

The standard deviation σ of the stochastic fluctuations is a measure of the radiometric temperature resolution and it has been estimated equal to 0.031 for 4s integration time. The higher the integration time the lower the temperature

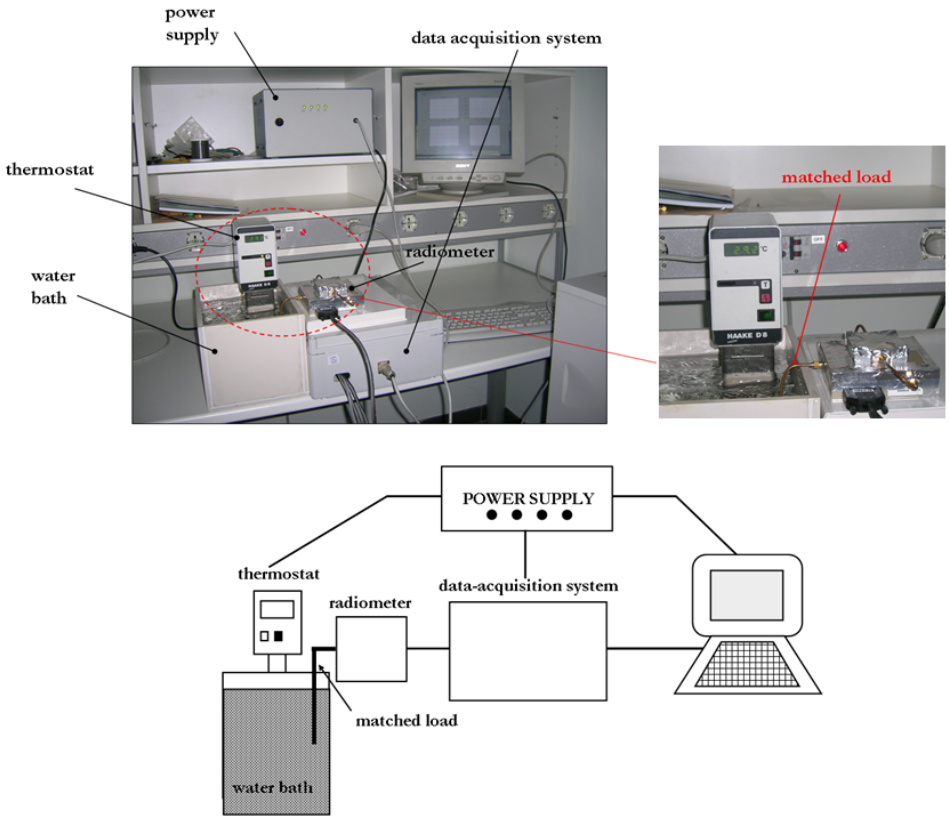

Figure 6.2: Experimental setup for the acquisition with a matched load in a thermostated bath (on the top) and its schematic representation (on the bottom).

resolution. A moving average of the radiometric data on a subset of 20 samples is shown in Fig.6.3b.

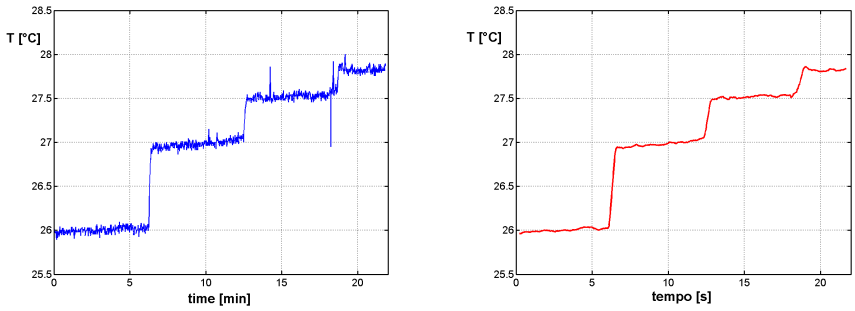

Figure 6.3: Record of radiometric data. A matched load in a thermostated water bath is connected to the input of the radiometer. Bath temperature steps are forced by a thermostat a). Moving average of the set of radiometric data of Fig.6.3a b).

6.2.1 Calibration

A matched load termination can also be exploited for receiver calibration. A calibration curve (see Fig.6.4) has been derived from a set of acquisitions similar to that of Fig.6.3a, by varying the bath temperature with steps of 1°C. The resulting relationship between the output indicator and the bath temperature provides the factor necessary for scaling the output to the temperature within the field of view of the antenna. It is interesting noticing from the diagram that the slope of the curve is very close to 1. The difference between the load temperature (T_{load}) and the estimated radiometric temperature (T_{rad}) is shown in Table 6.1 for all bath temperatures considered in the measurement.

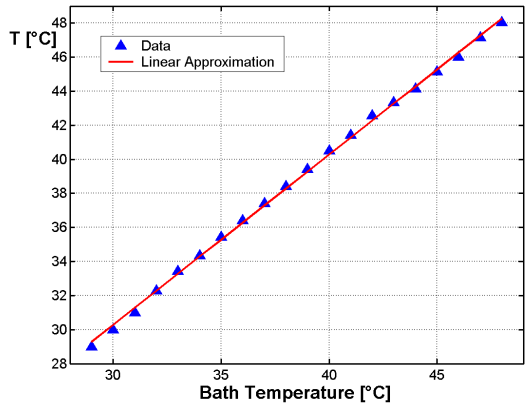

Figure 6.4: Calibration curve.

$T_{load}(^{\circ}C)$	$T_{rad}(^{\circ}C)$	$\mid T_{load} - T_{rad} \mid (^{\circ}C)$
29	29	0.00
30	30	0.00
31	31	0.00
32	32.28	0.28
33	33.42	0.42
34	34.35	0.35
35	35.42	0.42
36	36.42	0.42
37	37.42	0.42
38	38.42	0.42
39	39.42	0.42
40	40.5	0.50
41	41.42	0.42
42	42.56	0.56
43	43.35	0.35
44	44.13	0.13
45	45.13	0.13
46	46.00	0.009
47	47.15	0.15
48	48.03	0.03

Table 6.1: Load temperature and radiometric temperature for the measurement of Fig.6.4.

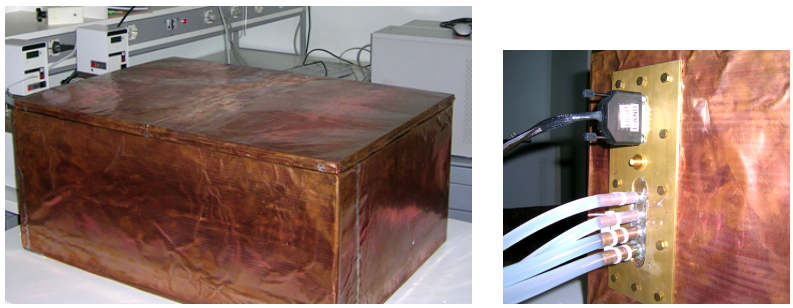

a) **b)**

Figure 6.5: Shielded box a). Metal mask for the cables to passing through the box. Radiometer-Data Acquisition System cable on the top. Four circular waveguides filled with circulating distilled water to control the temperature of main bath and of a tumor-imitator b).

6.3 Shielded Box

Since the electromagnetic signal from the body is extremely weak (on the order of picowatts), this makes it extremely important to shield the ambient noise in addition to design antennas that can collect the signal as efficiently as possible.

A shielded box (70cm x 70cm x 30cm) of copper has been realized to accommodate both the radiometer and the antenna in order the spurious radiation to be prevented from entering the receiver with saturation of the useful signal (see Fig.6.5a). The box is equipped with a lid that allows the housing of the components involved by an acquisition (radiometer, antenna and phantom). A metal mask with holes for connection to the radiometer-data acquisition system cable has been placed on one side of the box (see Fig.6.5b).

The shielding ability of the box has been tested during an acquisition consisting in two sequencies. Inside the box the radiometer input has been connected to an antenna of the type described in section 5.3.2. In the first part of the acquisition (7 minutes) the box has been kept closed; then it has been opened.

The recorded radiometric signal is shown in Fig.6.6. We conclude that the box is effective in shielding. However the standard deviation in the closed box is larger than the value ($\sim$ 0.03°C) that was measured for a matched load fully immersed in water. The estimated standard deviation for the radiometric output is equal to 0.060°C and 3°C respectively, for 4s integration time.

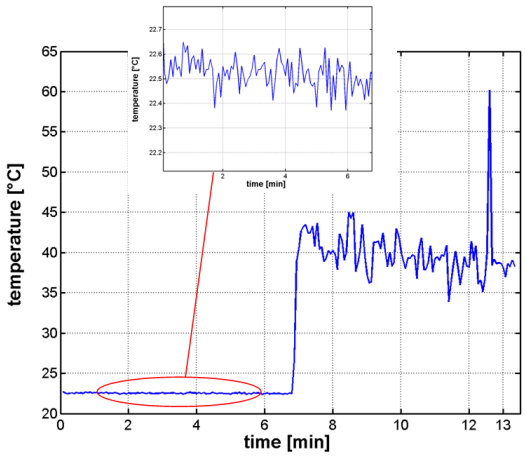

Figure 6.6: Radiometric acquisition with a patch antenna in air, inside the shielded box. The shielded box has been closed for the first 7 minutes. After it has been opened.

6.4 A Breast Phantom and a Tumor-Imitator

The experimental setup has been improved to characterize the radiometer ability to detect a hot spot inside a homogeneous medium. In particular it should be able to determine:

- the maximum detectable depth of a tumor imitator such that the radiometer can resolve the temperature gradient;

- the minimum detectable size of a tumor imitator such that the radiometer can detect it in terms of temperature gradient;

- the minimum detectable over-temperature between the tumor-imitator and the surrounding medium.

A PVC cylinder (diameter: 8cm, height: 15cm) open at the top and closed by a flexible membrane at the bottom, has been chosen to be filled with a glycerine tissue mimicking phantom. The electric properties of glycerine ($\epsilon_r \simeq 9$, $\sigma \simeq 0.2$S/m) are very closed to those of a fatty breast.

A patch antenna has been placed on the bottom of the cylinder and it has

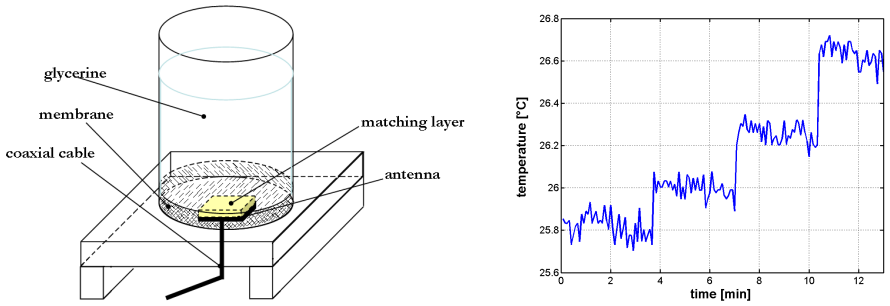

Figure 6.7: Glycerine tissue mimicking phantom a). A matched antenna in a thermostated glycerine bath is connected to the input of the radiometer. Glycerine temperature steps are forced b) .

been kept in contact with the membrane through a support. Between antenna and membrane, a matching layer is inserted to yield good matching to the glycerine.

Fig.6.7a shows a schematic representation of the phantom.

The phantom has been placed inside the box and antenna has been connected to the radiometer input through a coaxial cable. A two step procedure has been performed. In the first step the cylinder has been filled with thermostated glycerine and a sequence of radiometric data have been collected. In the second step a controlled volume of glycerine at higher temperature has been added and well mixed to the previous one in order the glycerine temperature to be homogeneous. The resulting temperature has been measured by a mercury thermometer with 0.1°C resolution. A second sequence of data have been collected.

Fig.6.7b shows the radiometric output for different temperature steps of the glycerine after calibration. A standard deviation of about 0.041 has been estimated from the recorded samples. The standard deviation is slightly higher than that of a matched load in a thermostated batch but it is still a good value. Glycerine temperature steps up to 0.2°C are well detected.

The average of each set of samples recorded over the time in which the shielded box is kept closed (between two consecutive mixing) is characterized by a slightly negative slope due to the fact that the glycerine is no longer ther-

mostated once inside the cylinder. As a consequence, its temperature decreases as a result of heat exchange with the environment at about 22°C.

6.4.1 An Improved Breast Phantom

The critical problem of the previous phantom model is that we cannot provide an accurate way to control the temperature of the glycerine. On the other hand mechanical agitators are uneffective with glycerine stirring because the fluid is dense.

Hence, we have arranged a cell-phantom consisting of two glass cylinders having different diameters without a superior base while the inferior base has a hole (Fig.6.8a). The lateral surfaces of the cylinders are welded together in order to create an interior space where the water can circulate. A 0.5mm thick PVC flexible semi-transparent membrane pasted on the glass, covers the hole on the bottom of the cell in order to close the cavity which is filled glycerine. A patch antenna contacts the membrane through a 2mm matching layer.

Distilled water circulates at a constant speed by an external thermostat (Hakke D8, Germany). This thermostat controls the temperature of the glycerine bath and ensures that the glycerine is thermostated.

A mammary gland tumor imitator made up of glass (Fig.6.8b) is placed in the middle of the glycerine bath and held upright by a mechanical arm. Our tumor imitator is very similar to a coaxial cable with an inner cylinder for the fluid inlet and an external cylinder that ends in a sphere for the fluid outlet. Distilled water circulates through the tumor imitator by a second external circulation as well as for the glycerine bath. The sphere radius is 1cm while the height of the tumor imitator is 12cm. The four PVC tubes (two for each circulation) pass through the shielded box by four hollow copper cylinders. The length and the radii of these cylinders have been chosen in order the cutoff frequency to be equal to the radiometer centre band frequency (see Fig.6.5b).

To measure the temperature inside the glycerine phantom and the tumor imitator we use two thermocouples (Copper-Constantan) 0.5mm thick[1]. A thermocouple has been placed on the outer surface of the tumor imitator sphere while the other one has been located at half the distance between the outer surface of the tumor imitator sphere and the inner surface of the cell (see Fig.6.9).

[1] The temperature control system has been assembled in a collaboration with prof. P. Coppa and G. Bovesecchi of the Department of Mechanics, University of "Tor Vergata", Rome.

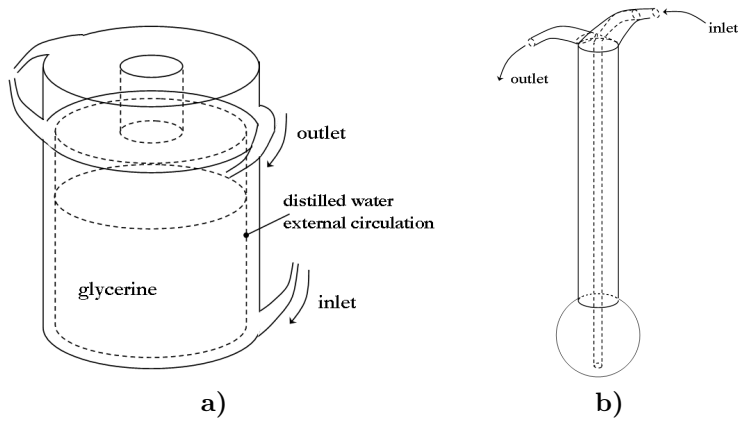

Figure 6.8: Glass cell for the breast phantom a). Tumor imitator b).

6.5 Measurements with the Tumor Imitator

We have adopted the following protocol to take the radiometric data when an over-temperature of 2°C is forced between the glycerine main bath and the tumor imitator.

1 The radiometer, the antenna and the glass-cell filled with the glycerine are placed inside the shielded box. The tumor imitator is placed in the middle of the glycerine bath and the center of the sphere is distant 12mm from the antenna.

2 Both the temperatures of the thermostats are set to 27°C in order the glycerine to reach this temperature as soon as possible by heating from the center of the glass cell and externally.

3 Once the glycerine temperature is increased up to desired value (as indicated by the thermocouples), we increase the temperature of the circuit that control the thermal status of the tumor imitator up to 29°C.

4 We let the water temperature inside the tumor imitator grow until it reaches the set value. Then we stop the acquisition.

Results of the radiometric acquisition described above are shown in Fig.6.10. A moving average of the radiometric samples is plotted in red.

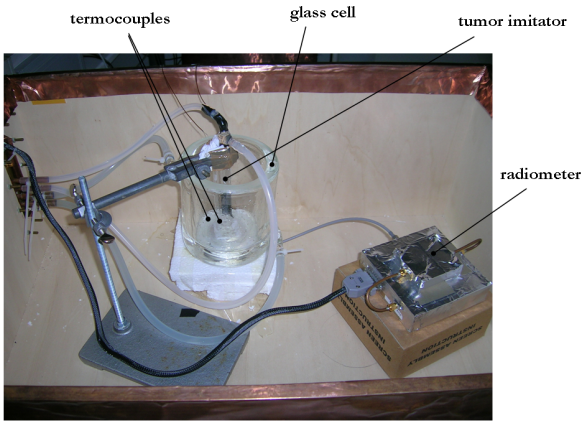

a)

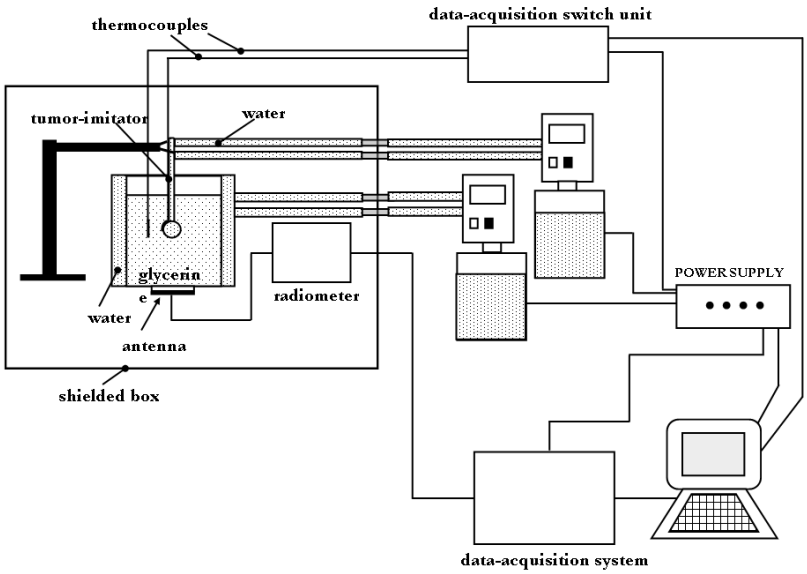

b)

Figure 6.9: Experimental setup for the measurements with the breast phantom and the tumor imitator a) and its schematic representation b).

It is interesting to notice from the diagram that an over-temperature of 2°C is recognized by the instrument as a difference radiometric temperature of about 0.5°C.

Unfortunately, we were unable to repeat such a radiometric acquisition for different depths of the tumor imitator inside the glycerine and for different over-temperature due to instability in the voltage outputs of the radiometer probably caused by instrumental overheating.

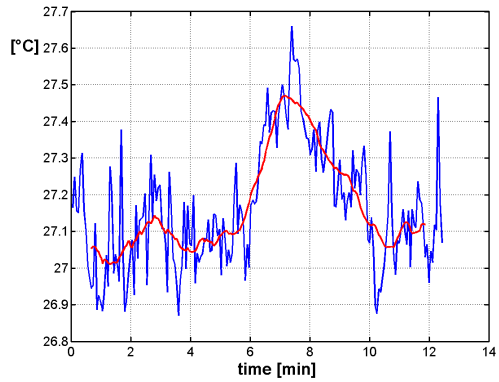

Figure 6.10: Record of radiometric data (blue). A matched antenna that contacts a thermostated glycerine bath through a PVC membrane is connected to the input of the radiometer. An over-temperature of 2°C between the glycerine bath and the tumor imitator is forced by two thermostats. Moving average of the set of radiometric data (red).

Conclusions

The aim of this study was to explore microwave radiometry for breast cancer detection based on the tumor over-temperature rationale.

Unlike the work of previous authors, who used microwave radiometry to retrieve temperature, the approach of the present study was to demonstrate the feasibility of tumor detection via differential (malignant-normal) data resulting from the thermal radiation spontaneously released by normal and malignant tissue in the microwave frequency band.

For this reason a full 3D numerical model that relates radiometric data to the temperature difference between normal and malignant breast has been developed.

Basing on this model tumor radiometric visibility has been predicted. The results indicate that a 10mm tumor is visible up to about 3cm by a radiometer with a standard resolution of 0.1°C. This visibility can be improved up to about 4cm by compressing the breast. A breast deformation of about 35% has been considered as painless compression in the range between 0 and 50% (that is typical in mammography). Additional computations should to be performed to investigate how sensitive the tumor radiometric visibility is to the amount of the breast compression.

The second part of the thesis was devoted to the instrumentation.

Radiometric measurements have been performed with an existing radiometer. A standard deviation of about 0.03°C for 4s integration time has been estimated when a matched load is connected to the input of the radiometer. All the measurements have been made in order to characterize the radiometer as a near-field sensing instrument. For this reason the antenna plays an important role in radiometer performance.

Two patch antennas have been designed and measured on volunteers to evaluate the change in antenna reflectivity when different portions of left and right breast are measured and to have some indications on the antenna to be

optimized. An average reflectivity of about 0.12 has been found over the band of operation. In the current design the optimization of the antenna as a radiometric device has received starting attention. Future research should provide a larger bandwidth and an optimization of the radiometric weighting function.

A breast phantom and a tumor imitator have been designed in order to characterize the radiometer ability to detect a hot spot inside a homogeneous medium. Some assumptions have been made in the modeling of the breast phantom. A homogeneous tissue mimicking phantom with dielectric properties similar to those of older women with most fatty breasts has been chosen for simplicity. The tumor-imitator as been modeled as a homogeneous medium as well. A distilled water has been used as tumor imitator to allow the temperature control by external circulation. A slightly higher standard deviation than that of a matched load has been found.

The instability of the radiometric output due to malfunctioning of electronic components of the radiometer has prevented me from taking additional data in phantom. The results were encouraging but final conclusions will be possible after further measurements.

Bibliography

[1] S. J. Nass, I. C. Henderson, and J. C. Lashof, *Mammography and Beyond: Developing Technologies for the Early Detection of Breast Cancer*. Washington: National Accademy Press, 2001.

[2] L. A. G. R. et al., *SEER Cancer Statistics Review:1973-1994, National Cancer Institute*. Bethesda, Maryland: NIH publication no.97-2789, 1997.

[3] T. Key, P. Appleby, I. Barnes, and G. Reeves, "Endogenous hormones and breast cancer collaborative group: Endogenous sex hormones and breast cancer in postmenopausal women: reanalysis of nine prospective studies," *J Microwave Power*, vol. 94, pp. 606–616, 2002.

[4] L. E, H. MD, and W. WC, "Diet and breast cancer," *Curr Oncol Rep*, vol. 9, no. 1, pp. 31–41, 2007.

[5] L. L. H. et al., "Breast cancer screening: Summary of the evidence for the U.S. preventive services task force," *Ann. Intern. Med.*, vol. 137, pp. 347–360, 2002.

[6] O. Olsen and P. C. Gøtzsche, *Systematic review of screening for breast cancer with mammography*. Denmark: The Nordic Cochrane Center, 2001.

[7] S. W. F. et al., "Report of the international workshop on screening for breast cancer," *JNCI*, vol. 85, pp. 1644–1656, 1993.

[8] J. T. C. et al., "Non-invasive thermal assessment of tissue phantoms using an active near field microwave imaging technique," *Int. J. Hyperthermia*, vol. 14, no. 6, pp. 513–534, 1998.

[9] N. F. B. et al., "Quantitative classiafication of mammographic densities and breast cancer risk," *JNCI*, vol. 87, pp. 670–675, 1995.

[10] E. A. Sickles, "Nonpalpable, circumscribed, noncalcified, solid breast masses: Likelihood of malignancy based on lesion size and age of patient," *Radiology*, vol. 192, no. 2, pp. 439–442, 1994.

[11] E. C. Fear, S. C. Hagness, P. M. Meaney, M. Okoniewski, and M. A. Stuchly, "Enhancing breast tumor detection with near-field imaging," *IEEE Microwave Magazine*, vol. 3, no. 1, pp. 48–56, 2002.

[12] X. Li and S. C. Hagness, "A confocal microwave imaging algorithm for breast cancer detection," *IEEE Microwave Wireless Compon. Lett.*, vol. 11, no. 3, pp. 130–132, 2001.

[13] M. et al., "A large-scale study of the ultrawideband microwave dielectric properties of normal, benign and malignant breast tissues obtained from cancer surgeries," *Phys. Med. Biol.*, vol. 52, no. 20, pp. 6093–6115, 2007.

[14] E. Zastrow, S. K. Davis, and S. C. Hagness, "Safety assessment of breast cancer detection via ultrawideband microwave radar operating in pulsed-radiation mode," *Microwave and optical Technology Letters*, vol. 49, no. 1, pp. 221–225, 2007.

[15] P. M. Meany, M. W. Fanning, and T. R. et al., "Initial clinical experience in microwave breast imaging in women with normal mammography," *Academic Radiology*, vol. 14, pp. 207–218, 2007.

[16] K. Paulsen, P. Meany, and S. Poplack, "Imaging the breast with microwaves: The dartmouth experience," in *URSI General Assembly, Chicago (IL)*, 2008 August.

[17] A. Fhager, P. Hashemzadeh, L. Baath, and M. Persson, "Microwave imaging for mammography using an iterative time-domain reconstruction algorithm; initial experiments," in *in Proceedings of the 16th International Zurich Symposium on Electromagnetic Compatibility; Topical Meetings*, 2005, pp. 67–70.

[18] P. Hashemzadeh, A. Fhager, and M. Persson, "Experimental investigation on an optimization approach to microwave tomography," *Electromagnetic Biology and Medicine*, vol. 25, no. 1, pp. 1–12, 2006.

[19] A. Fhager and M. Persson, "Using a priori data to improve the recpnstruction of small objects in microwave tomography," *IEEE Trans. Microwave Theory Techniques*, vol. 55, no. 11, pp. 2454–2462, 2007.

[20] A.Sabouni, A. Ashtari, S. Noghanian, and S. Pistorius, "Breast tumor detection and characterization based on microwave tomography," in *URSI General Assembly, Chicago (IL)*, August 2008.

[21] A. Fhager, C.C.Chen, and M. Persson, "On the use of a priori data in microwave tomography," in *URSI General Assembly, Chicago (IL)*, August 2008.

[22] A. Sabouni, M. Xu, S. Thulasiraman, and S. Pistorius, "Efficient microwave breast imaging technique using parallel finite difference time domain and parallel genetic algorithms," in *IEEE AP-S International Symposium on Antennas and Propagation, Hawaii, USA*, June 2007.

[23] T. Rubaek, P. Meany, P. Meincke, , and K. D. Paulsen, "Nonlinear microwave imaging for breast cancer screening using gauss-newton's method and the cgls inversion algorithm," *IEEE Trans. Antennas Propag.*, vol. 55, no. 8, pp. 2320–2331, 2007.

[24] P.Kosmas, J.D.Shea, B. V. Veen, , and S. Hagness, "Microwave imaging of realistic breast phantoms via a three-dimensional inexact gauss-newton algorithm," in *IEEE International Symposium on Antennas and Porpagation*, San Diego, CA 2008.

[25] J.D.Shea, P. Kosmas, S.C.Hagness, and B. V. Veen, "Three-dimensional microwave breast imaging: A bounded, multi-frequency inverse scattering solution on a uniform voxel mesh," in *URSI General Assembly, Chicago (IL)*, 2008.

[26] M. Lazebnik, S. C. Hagness, and J. H. Booske, "Dielectric-properties contrast enhancement for microwave breast cancer detection: Numerical investigation of microbubbles contrast agents," in *URSI General Assembly, Chicago (IL)*, 2008 August.

[27] S. Hagness, A. Taflove, and J. Bridges, "Two-dimensional fdtd analysis of a pulsed microwave confocal system for breast cancer detection: fixed-focus and antenna array sensors," *IEEE Trans. Biomed. Eng.*, vol. 45, no. 12, pp. 1470–1479, 1998.

[28] E. Fear, X. Li, S. Hagness, and M. Stuchly, "Confocal microwave imaging for breast cancer detection: localization of tumors in three dimensions," *IEEE Trans. Biomed. Eng.*, vol. 49, no. 8, pp. 812–822, 2002.

[29] E. Fear, S. Hagness, P. Meaney, M. Okoniewski, and M. Stuchly, "Enhancing breast tumour detection with near-field imaging," *IEEE Microwave Magazine*, vol. 3, no. 1, pp. 48–56, 2002.

[30] E. F. P. Meaney and M. Stuchly, "Microwave for breast cancer detection," *IEEE potentials*, vol. 22, no. 1, pp. 12–18, 2003.

[31] M. Elsdon, M. Leach, M. FDO, S. Foti, and D. Smith, "Early stage breast cancer detection using indirect microwave holography," in *in Proceedings of the 36th European Microwave Conference, Manchester (UK)*, September 2006, pp. 1256–1259.

[32] F. Bardati, M. Bertero, M. Mongiardo, and D. Solimini, "Singular system analysis of the inversion of microwave radiometric data: applications to biological temperature retrieval," *Inv. Probl.*, vol. 3, pp. 347–370, 1987.

[33] B. Bocquet, J. C. V. D. Velde, A. Mamouni, Y. Leroy, G. Giaux, J. Delannoy, and D. Delvalee, "Microwave radiometric imaging at 3 GHz for the exploration of breast tumours," *IEEE Trans. MTT*, vol. 38, no. 6, pp. 791–793, 1990.

[34] D. V. Land, "A clinical microwave thermography system," *IEEE Proc.*, vol. 134, no. 2, pp. 193–200, 1987.

[35] Y. L. A. M. J. C. V. D. V. B. Bocquet and B. Dujardin, "Microwave radiometry for non-invasive thermometry," *Automedica*, vol. 8, no. 4, pp. 181–202, 1987.

[36] Y. Leroy, A. Mamouni, J. C. V. D. Velde, B. Bocquet, G. Giaux, and J. Dellanoy, "Non-invasive measurement of subcutaneous tissue temperature by microwave radiometry," *Innov. Tech. Biol. Med.*, vol. 12, no. 1, pp. 155–162, 1991.

[37] A. Mamouni, Y. Leroy, B. Bocquet, J. C. V. D. Velde, and F. Gelin, "Computation of near field microwave radiometric signals: definition and experimental verification," *IEEE Trans. MTT*, vol. 39, no. 1, pp. 124–132, 1991.

[38] B. Stec, "Microwave thermography: methods and equipment," in *in 11th Int. Conf. Microw., Radar Wirel. Commun., Worksh., Warsaw, Poland*, 1996, pp. 97–114.

[39] F. Sterzer, "Microwave radiometers for non-invasive measurements of subsurface tissue temperatures," *Automedica*, vol. 8, no. 4, pp. 203–211, 1987.

[40] E. Schanda, *Passive Microwave Sensing in Remote Sensing for Environmental Sciences.* Springer-Verlag: Berlin, Germany, 1976.

[41] B. Enander and G. Larson, "Microwave radiometric measurements of the temperature inside a body," *Electron. Lett.*, vol. 10, no. 15, pp. 317–318, 1974.

[42] K. Maruyma, S. Mizushina, T. Sugiura, G. M. J. V. Leeuwen, J. W. Hand, G. Marrocco, F. Bardati, A. D. Edwards, D. Azzopardi, and D. Land, "Feasibility of noninvasive measurement of deep brain temperature in new-born infants by multifrequency microwave radiometry," *IEEE Trans. Microwave Theory Tech.*, vol. 48, no. 11, pp. 2141–2147, 2000.

[43] F. Sterzer, P. Paglione, F. Wozniak, J. Mendecki, E. Friedenthal, and C. Botstein, "Self-balancing microwave radiometer for noninvasively measuring the temperature of subcutaneous tissue during localized hyperthermia reatments of cancer," *IEEE MTT-S Int. Microwave Symp. Digest.*, vol. 82, no. 1, pp. 438–440, 1982.

[44] M. Chive, M. Plancot, Y. Leroy, G. Giaux, and B. Prevost, "Microwave(1 and 2.45 GHz) and radiofrequency(13.56 MHz) hyperthermia monitored by microwave thermography," in *in European Microwave Conf., Helsinki, Finland*, Sept. 1982.

[45] H. Ohba, M. Kinomura, M. Ito, T. Sugiura, and S. Mizushina, "Multifrequency microwave radiometry for noninvasive thermometry using a new temperature profile model function," *Trans. IEICE Electron.*, vol. E78-C, no. 8, pp. 1071–1081, 1995.

[46] S. J. P. Stauffer and D. Neuman, "Dual-mode antenna design for microwave heating and non-invasive thermometry of superficial tissue disease," *IEEE Trans. Bio-Med. Eng.*, vol. 47, no. 11, pp. 1500–1509, 2000.

[47] G. M. J. V. Leeuwen, J. Hand, J. J. Lagendijk, D. V. Azzopardi, and A. D. Edwards, "Numerical modeling of temperature distributions within the neonatal head," *Ad. Pediatric Res.*, vol. 48, no. 3, pp. 351–356, 2000.

[48] J. W. Hand, G. M. J. V. Leeuwen, S. Mizushina, J. B. V. de Kamer K. Maruyama, T. Sugiura, D. V. Azzopardi, and A. D. Edwards, "Monitoring of deep brain temperature in infants using multi-frequency microwave radiometry and thermal modeling," *Phys. Med. Biol.*, vol. 46, no. 7, pp. 1885–1903, 2001.

[49] L. Dubois, C. Vanoverschelde, V. Thomy, J. P. Sozanski, and M. Chivé, "Temperature control by microwave radiometry with narrow bandwidth," *Eur. Physical J. Appl. Phys.*, vol. 9, no. 1, pp. 63–68, 2000.

[50] A. H. Barrett, P. C. Myers, and N. L. Sadowsky, "Detection of breast cancer by microwave radiometry," *Radio Sci*, vol. 12, p. 167, 1977.

[51] J. Edrich, "Centimeter-and millimiter-wave thermography: A survey on tumor detection," *J Microwave Power*, vol. 14, pp. 95–104, 1979.

[52] K. L. C. A. M. El-Mahdi and J. Shaeffer, "Dual-mode microwave system to enhance early detection of cancer," *IEEE Trans. Microwave Theory Tech.*, vol. 29, no. 3, pp. 256–260, 1981.

[53] D. V. Land, S. M. Fraser, and R. D. Shaw, "A review of clinical experience of microwave thermography," *J Med Eng Tech*, pp. 109–113, 1986.

[54] K. L. Carr, "Microwave radiometry: Its importance to the detection of cancer," *IEEE Trans. Microwave Theory Tech.*, vol. 37, no. 12, pp. 1862–1869, 1989.

[55] F. Bardati and D. Solimini, "Radiometric sensing of biological layered media," *Radio Sci*, vol. 18, pp. 1393–1401, 1983.

[56] S. Mizushina, T. Shimizu, K. Suzuki, M. Kinomura, H. Ohba, and T. Sugiura, "Retrieval of temperature-depth profile in biological objects from multi-frequency microwave radiometric data," *J. Electromag. Waves App.*, vol. 7, pp. 1515–1547, 1993.

[57] M. El-Shenawee, "Numerical assesment of multifrequency microwave radiometry for sensing malignant breast cancer tumors," *Microwave and Opt. Thecnol. Lett.*, vol. 36, no. 5, pp. 394–398, 2003.

[58] J. Robert, J. Edrich, P. Thouvenot, M. Gautherie, and J. M. Eskanye, "Millimeter wave thermography: Preliminary clinical finding on head and neck diseases," *J. Microwave Power*, vol. 14, no. 2, pp. 45–52, 1979.

[59] J. Robert, J. Edrich, Y. Leroy, A. Mamouni, J. M. Eskaneye, and P. Thouvenot, "Clinical applications of microwave thermography," *Soc.Photo-Opt. Instrum. Eng.*, vol. 211, pp. 149–153, 1979.

[60] J. W. Lee, S. M. Lee, K. S. Kim, W. T. Han, G. Yoon, L. A. Pasmanik, I. A. Ulyanichev, and A. V. Troitsky, "Experimental investigation of the mammary gland tumour phantom for multifrequency microwave radiothermometers," *Med Biol Eng Comput*, vol. 42, no. 5, pp. 581–590, 2004.

[61] A. H. Barrett and P. C. Myers, "Subcutaneous temperatures: A method of noninvasive sensing," *Science*, vol. 190, pp. 669–671, 1975.

[62] K. L. Carr, A. M. E. Mahdi, and J. Schaeffer, "Dual mode microwave system to enhance early detection of cancer," *IEEE Trans. Microwave Theor. Tech.*, vol. MTT-29, pp. 256–260, 1980.

[63] B. Enander and G. Larson, "Microwave radiometry measurements of the temperature inside a body," *Electron. Lett.*, vol. 10, p. 317, 1974.

[64] J. . Edrich and P. C. Hardee, "Thermography at millimeter wavelengths," *Proc. IEEE*, vol. 62, pp. 1391–1392, 1974.

[65] S. Mizushina, Y. Hamainura, and T. Sugiura, "A three-band microwave radiometer system for noninvasive measurement of the temperature at various depths," *IEEE MTT-S Dig.*, pp. 759–762, 1986.

[66] A. Mamounit, Y. Leroy, J. V. de Velde, and L. Bellarbi, "lntroduction to correlation microwave thermography," *J. Microwave Power*, vol. 61, 1983.

[67] E. Edenhofer, "Electromagnetic remote sensing of the temperature profile in a stratified medium of biological tissues by stochastic inversion of radimetric data," *Radio Sci.*, vol. 16, pp. 1065–1069, 1981.

[68] M. Bertero, M. Bertero, M. Mongiardo, and D. Solimini, "Biological temperature retrieval from microwave radiometric data," *Recontres Interdisciplinaires Problèmes Inverses, Montpellier*, pp. 1–13, 1984.

[69] S. Jacosen and P. Stauffer, "Can we settle with single-band radiometric temperature monitoring during hyperthermia treatment of chestwall recurrence of breast cancer using a dual-mode transceiving applicator?" *Phys. Med. Biol.*, vol. 52, no. 4, pp. 911–928, 2007.

[70] S. Jacobsen, H. Rolfsnes, and P. Stauffer, "Characteristics of microstrip muscle-loaded single-arm archimedean spiral antennas as investigated by FDTD numerical computations," *IEEE TBME*, vol. 52, no. 2, pp. 321–330, 2005.

[71] T. Yahara, T. Koga, S. Yoshida, S. Nakagawa, H. Deguchi, and K. Shirouzu, "Relationship between microvessel density and thermographic hot areas in breast cancer," *Surg Today*, vol. 33, no. 4, pp. 243–248, 2003.

[72] G. Bekefi, *Radiation Processes in Plasmas*. New York: J. Wiley, 1966.

[73] K. M. Ludeke, J. Kohler, and J. Kanzenbach, "A new radiation balance microwave thermograph for simultaneous and independent temperature and emissivity measurements," *J Microwave Power*, vol. 14, pp. 117–121, 1979.

[74] Y. Leroy, B. Bocquet, and A. Momouni, "Non-invasive radiometry thermometry," *Physiol. Meas.*, vol. 19, no. 2, pp. 127–148, 1998.

[75] M. Gautherie, Y. Quenneville, and C. M. Gros, "Metabolic heat production growth rate and prognosis of early breast carcinomas," *Biomedicine*, vol. 22, pp. 328–336, 1975.

[76] E. Y. K. Ng and N. M. Sudharsan, "An improved three-dimensional direct numerical modelling and thermal analysis of a female breast with tumour," *Proc. Instn Mech Engrs*, vol. 215, pp. 25–37, 2001.

[77] M. Gautherie, "Thermopatology of breast cancer: measurement and analysis of in vivo temperature and blood flow," *Ann New York Acad Sci*, vol. 335, pp. 383–415, 1980.

[78] H. H. Pennes, "Analysis of tissue and arterial blood temperatures in the resting human forearm," *J. Appl. Physiol.*, vol. 1, pp. 93–122, 1948.

[79] J. Werner and M. Buse, "Temperature profiles with respect to inhomogeneity and geometry of the human body," *J. Appl. Physiol.*, vol. 65, pp. 1100–1118, 1988.

[80] H. S. Carslaw and J. C. Jaeger, *Conduction of Heat in solids*. Oxford: Oxford University Press, 1959.

[81] H. Nakajima, N. Imanishi, and S. Aiso, "Arterial anatomy of the nipple-areola complex," *Plast. Reconstr. Surg.*, vol. 96, no. 4, pp. 843–845, 1995.

[82] S.Iudicello and F. Bardati, "Functional imaging of compressed breast by microwave radiometry," *ACES Journal, in press.*

[83] *The European Protocol for the Quality Control of the Physical and Thecnical Aspects of Mammography Screening.* 3rd edn: CEC Report EUR 14821, 1999.

[84] COMSOL, "www.comsol.com," *Version 3.3a.*

[85] A. Samani, J. Bishop, M. J. Yaffe, and B. Plewes, "Biomechanical 3-d finite element modeling of the human breast using mri data," *IEEE Transactions on Medical Imaging*, vol. 20, no. 4, pp. 271–279, 2001.

[86] N. V. Rviter, T. O. Muller, R. Stotzka, H. Gemmeke, J. R. Reichenba, and W. Kaiser, "Automatic image matching for breast cancer diagnostics by a 3d deformation model of the mamma," *Biomed. Tech. (Berl)*, vol. 47 Suppl1 Pt2, pp. 644–7, 2002.

[87] P. Pathmanathan, D. Gavaghan, J. Whiteley, S. M. Bredy, M. Nash, P. Nielsen, and V. Rajagopal, *Predicting Tumor Location by Simulating Large Deformations of the Breast using a 3D Finite Element Model and Nonlinear Elasticity.* In Christian, B Haynor D. R. and Hellier P. Eds. Proc. MICCAI2004, LNCS3217: Springer-Verlag, 2004, pp. 217–224.

[88] V. Rajagopal, P. M. F. Nielsen, and M. P. Nash, "Development of a three dimensional finite element model of breast mechanics," in *in Proceedings of the 26th Annual International Conference of the IEEE EMBS, San Francisco, CA, USA*, Sept.1-5 2004.

[89] N.V.Ruiter, R.Stotzka, T. Muller, H. Gemmeke, J. Reichenbach, and W. Kaiser, "Model- based registration of x-ray mammograms and mr images of the female breast," *IEEE Transactions on Nuclear Science*, vol. 53, pp. 204–211, 2006.

[90] V. Vuskovic and M. Kauer, "In vivo-measurement of elasto mechanical properties of soft biological tissue," in *in European Medical and Biological Engineering Conference, Vienna, Austria*, 1999.

[91] R. D. Howe, "Identification of constitutive nonlinear constitutive law parameters of breast tissue," in *in Summer Bioengineering Conference, Vail, Colorado*, June 22-26 2005.

[92] N. Ruiter, *Registration of X-Ray Mammograms and MR-Volumes of the Female Breast based on Simulated Mammographic Deformation.* University of Mannehim: PhD thesis, 2003, pp. 55–74.

[93] D. C. Sullivan, C. A. Beam, S. M. Goodman, and D. L. Watt, "Measurement of force applied during mammography," *Radiology*, vol. 181, no. 2, pp. 355–7, 1991.

[94] P. Wellman, R. D. Howe, E. Dalton, and K. A. Kern, "Breast tissue stiffness in compression is correlated to histological diagnosis," in *Tech. Rep., Harward BioRobotics Laboratory, Harward University, Cambridge, Mass, USA*, 1999.

[95] A. R. Mijar and J. S. Arora, "An augmented lagrangian optimization method for conact analysis problem, 1: formulation and algorithm," *Struct Multidisc Optim*, vol. 28, pp. 99–112, 2004.

[96] W. B. Nickell and J. Skelton, "Breast fat and fallacies:more than 100 years of anatomical fantasy," *J of Hum Lact*, vol. 21, no. 2, pp. 126–130, 2005.

[97] N. A. Lee, H. Rusinek, J. Weinreb, R. Chandra, H. Toth, C. Singer, and G. Newstead, "Fatty and fibroglandular tissue volumes in the breast of women 20-83 years old: Comparison of x-ray mammography and computer-assisted mr imaging," *AJR*, vol. 168, no. 2, pp. 501–6, 1997.

[98] F. Bardati and S. Iudicello, "Modeling the visibility of breast malignancy by a microwave radiometer," *IEEE Trans. Biomed. Eng.*, vol. 55, pp. 214–221, 2007.

[99] B. Bocquet, A. Mamouni, M. Hochedez, J. C. V. de Veldea, and Y. Leroy, "Visibility of local thermal structures and temperature retrieval by microwave radiometry," *Elettronics Letters*, vol. 22, no. 3, pp. 120–121, 1986.

[100] P. C. Myers, N. L. Sadowsky, and A. H. Barrett, "Microwave thermography: Principles, methods, and clinical applications," *J. Microwave Power*, vol. 14, no. 2, pp. 105–115, 1979.

[101] S. Mizushina, Y. Hamamura, and T. Sugiura, "A three-band microwave radiometer system for noninvasive measurement of the temperature at various depths," *IEEE MTT-S Digest, volume =.*

[102] S. Jacobsen and A. Murberg, "Characterization of a transceiving antenna concept for microwave heating and thermometry of superficial tumors," *Progress in Electromagnetics Research, PIER*, vol. 18, pp. 105–125, 1998.

[103] S. Jacobsen, H. O. Rolfsnes, and P. R. Stauffer, "Characteristics of microstrip muscle-loaded single-arm archimedean spiral antennas as investigated by fdtd numerical computations," *IEEE Trans. Biomed. Eng.*, vol. 52, no. 2, pp. 321–330, 2005.

[104] S. A. Bokhari, J. F. Zurcher, J. R. Mosig, and F. E. Gardiol, "A small microstrip patch antenna with a convenient tuning option," *IEEE Trans. Ant. Prop.*, vol. 44, no. 11, pp. 1521–1527, 1996.

[105] C. Wood, "Improved bandwidth of microstrip antennas using parasitic elements," *IEEE Proceedings H*, vol. 127, no. 4, pp. 231–234, 1980.